

**DOME COLLAPSE DRIVEN BLOCK-AND-ASH FLOWS ON SHIVELUCH, AND  
PYROCLASTIC FLOWS ON MOUNT ST. HELENS:  
DEPOSIT MORPHOLOGY AND DISTRIBUTION ANALYSIS USING  
MULTIPARAMETER REMOTE SENSING- AND FIELD-BASED METHODS**

by

**Janine Barbara Krippner**

Bachelor of Science, University of Waikato, 2007

Master of Science, University of Waikato, 2009

Submitted to the Graduate Faculty of  
The Dietrich School of Arts and Sciences in partial fulfillment  
of the requirements for the degree of  
Doctor of Philosophy

University of Pittsburgh

2017

UNIVERSITY OF PITTSBURGH  
DIETRICH SCHOOL OF ARTS AND SCIENCES

This dissertation was presented

by

Janine Barbara Krippner

It was defended on

July 7, 2017

and approved by

John S. Pallister, Chief Volcano Disaster Assistance Program,

USGS Cascades Volcano Observatory (External Examiner)

Daniel Bain, Assistant Professor, University of Pittsburgh

William Harbert, Professor, University of Pittsburgh

Nadine McQuarrie, Associate Professor, University of Pittsburgh

Dissertation Advisor: Michael S. Ramsey, Professor, University of Pittsburgh

Copyright © by Janine Krippner

2017

**DOME COLLAPSE DRIVEN BLOCK-AND-ASH FLOWS ON  
SHIVELUCH, AND PYROCLASTIC FLOWS ON MOUNT ST. HELENS:  
DEPOSIT MORPHOLOGY AND DISTRIBUTION ANALYSIS USING  
MULTIPARAMETER REMOTE SENSING- AND FIELD-BASED  
METHODS**

Janine B. Krippner, PhD

University of Pittsburgh, 2017

Pyroclastic density currents are volcanic granular flows that include dome collapse-derived block-and-ash flows, and column collapse-derived pyroclastic flows. Volcanic dome-building cycles can last for years and can produce numerous collapse events that deposit block-and-ash flows up to 19 km from the dome. These impact surrounding communities and too-often result in fatalities, and populations have to be evacuated. Shiveluch in Kamchatka, Russia, is one of the world's most active dome-building volcanoes and has produced some of the largest historical block-and-ash flows, globally. The current eruption phase of Shiveluch volcano has been ongoing since 2001 in a cycle of dome growth and collapse. Understanding these prolonged dome growth episodes and characterizing the extreme end-members in deposit size and runout range is important for investigating these hazards at Shiveluch and other similar volcanoes. This multi-spatial scale investigation links dome activity to the block-and-ash flow deposits using satellite- and field-based data. Advanced Spaceborne Thermal Emission and Reflection Radiometer (ASTER) thermal infrared (TIR), shortwave infrared (SWIR), and visible-near infrared (VNIR) data are used to quantify the distribution of dome collapse events and resulting deposits through time. Small-scale deposit features are identified with field and high spatial resolution (~0.5 m) WorldView-02 and



QuickBird-02 panchromatic data. These block-and-ash flow deposits are compared to the well-studied Mount St. Helens 1980 column collapse pyroclastic flow deposits using historic aerial photography and airborne LiDAR data. Although these deposits are composed of different material that result from the different eruption styles, they contain similarities that reflect similar depositional processes, and differences that reflect the initiation mechanisms. These remotely-identified characteristics can help with rapid identification of the eruption style and can provide a safe and rapid assessment of eruptive products at dangerous and/or remote volcanoes around the world.

## TABLE OF CONTENTS

<b>PREFACE.....</b>	<b>XXI</b>
<b>1.0 INTRODUCTION.....</b>	<b>1</b>
<b>2.0 PARAMETRIC ANALYSIS OF LAVA DOME COLLAPSE EVENTS AND PYROCLASTIC DEPOSITS AT SHIVELUCH VOLCANO, KAMCHATKA, USING ORBITAL VISIBLE AND INFRARED DATA.....</b>	<b>4</b>
<b>2.1 INTRODUCTION .....</b>	<b>4</b>
<b>2.1.1 Summary of the recent eruption history of Shiveluch .....</b>	<b>9</b>
<b>2.2 METHODOLOGY .....</b>	<b>13</b>
<b>2.3 RESULTS .....</b>	<b>17</b>
<b>2.3.1 19 May 2001 .....</b>	<b>17</b>
<b>2.3.2 10 May 2004 .....</b>	<b>23</b>
<b>2.3.3 27-28 February 2005.....</b>	<b>23</b>
<b>2.3.4 18-19 December 2007.....</b>	<b>25</b>
<b>2.3.5 25-26 June 2009.....</b>	<b>25</b>
<b>2.3.6 27 October 2010 .....</b>	<b>26</b>
<b>2.3.7 26 July 2013.....</b>	<b>27</b>
<b>2.3.8 03 December 2013.....</b>	<b>28</b>
<b>2.4 DISCUSSION.....</b>	<b>29</b>
<b>2.5 CONCLUSIONS .....</b>	<b>38</b>
<b>2.6 ACKNOWLEDGEMENTS .....</b>	<b>39</b>

<b>3.0</b>	<b>THE 2005 AND 2010 BLOCK-AND-ASH FLOW DEPOSITS ON SHIVELUCH VOLCANO, KAMCHATKA.....</b>	<b>40</b>
<b>3.1</b>	<b>INTRODUCTION .....</b>	<b>40</b>
<b>3.2</b>	<b>METHODOLOGY .....</b>	<b>43</b>
<b>3.3</b>	<b>RESULTS .....</b>	<b>44</b>
<b>3.3.1</b>	<b>Shiveluch 2005 BAF deposit .....</b>	<b>46</b>
<b>3.3.1.1</b>	<b>Vegetation damage .....</b>	<b>54</b>
<b>3.3.1.2</b>	<b>Deposit remobilization .....</b>	<b>58</b>
<b>3.3.1.3</b>	<b>Degassing Structures.....</b>	<b>58</b>
<b>3.3.1.4</b>	<b>Erosion and redeposition.....</b>	<b>59</b>
<b>3.3.1.5</b>	<b>Stratigraphic exposures .....</b>	<b>61</b>
<b>3.3.2</b>	<b>Shiveluch 2010 BAF Deposit.....</b>	<b>64</b>
<b>3.3.2.1</b>	<b>2010 channelized deposit .....</b>	<b>67</b>
<b>3.3.2.2</b>	<b>Ridges and scarps.....</b>	<b>70</b>
<b>3.3.2.3</b>	<b>Erosion .....</b>	<b>72</b>
<b>3.3.2.4</b>	<b>Degassing structures .....</b>	<b>72</b>
<b>3.3.2.5</b>	<b>Surface block content.....</b>	<b>72</b>
<b>3.4</b>	<b>DISCUSSION.....</b>	<b>73</b>
<b>3.4.1</b>	<b>Application to LAHARZ model .....</b>	<b>82</b>
<b>3.5</b>	<b>CONCLUSIONS .....</b>	<b>85</b>
<b>3.6</b>	<b>ACKNOWLEDGEMENTS .....</b>	<b>86</b>
<b>4.0</b>	<b>A COMPARISON OF COLUMN COLLAPSE-DERIVED PYROCLASTIC FLOW DEPOSITS ON MOUNT ST. HELENS VOLCANO, USA, AND DOME-</b>	

<b>COLLAPSE-DERIVED BLOCK-AND-ASH FLOWS ON SHIVELUCH VOLCANO, KAMCHATKA .....</b>	<b>87</b>
<b>4.1    INTRODUCTION .....</b>	<b>87</b>
<b>4.1.1    The 1980 eruption of Mount St. Helens.....</b>	<b>90</b>
<b>4.1.2    Shiveluch 2005, 2010, and 2013 eruptions.....</b>	<b>92</b>
<b>4.2    METHODS.....</b>	<b>93</b>
<b>4.3    RESULTS .....</b>	<b>96</b>
<b>4.3.1    Componentry and composition .....</b>	<b>99</b>
<b>4.3.2    Aerial Deposit Distributions .....</b>	<b>102</b>
<b>4.3.3    Sheet-like deposits.....</b>	<b>102</b>
<b>4.3.4    Composite lobate deposits.....</b>	<b>104</b>
<b>4.3.5    Lobate morphologies .....</b>	<b>106</b>
<b>4.3.6    Primary and secondary levees and channels.....</b>	<b>110</b>
<b>4.3.7    Shallow deposit remobilization.....</b>	<b>111</b>
<b>4.3.8    Ridges.....</b>	<b>113</b>
<b>4.4    DISCUSSION.....</b>	<b>118</b>
<b>4.4.1    Composite lobate features.....</b>	<b>121</b>
<b>4.4.2    Lobate morphology.....</b>	<b>121</b>
<b>4.4.3    Compression ridges versus levees .....</b>	<b>125</b>
<b>4.4.4    Secondary remobilization .....</b>	<b>127</b>
<b>4.5    CONCLUSIONS .....</b>	<b>128</b>
<b>4.6    ACKNOWLEDGEMENTS .....</b>	<b>129</b>
<b>5.0    CONCLUDING REMARKS .....</b>	<b>130</b>

<b>APPENDIX A .....</b>	<b>133</b>
<b>BIBLIOGRAPHY .....</b>	<b>140</b>

## LIST OF TABLES

Table 1. Available dome growth rates from Shevchenko et al., 2015 and references therein.....	10
Table 2. Summary of Shiveluch eruptive product composition over time. ....	11
Table 3. Available parameters for the eight Shiveluch dome collapse events.....	12
Table 4. ASTER VNIR, SWIR, and TIR data used in this study. ....	14
Table 5. Summary of dome and block and ash flow deposit parameters for the eight collapse events. .....	16
Table 6. ASTER TIR and VNIR scenes used for dome collapse scar analyses. ....	21
Table 7. Block and ash flow maximum runout distance and maximum deposit area for Shiveluch and other dome-producing volcanoes around the world.....	35
Table 8. Parameters for the high resolution data sets used in this chapter. ....	43
Table 9. Summary of the 2005 and 2010 block and ash flow (BAF) deposits. Deposit and collapse scar values are from Chapter one.....	74
Table 10. Best-fit parameters for the two BAF deposits used in the LAHARZ model.....	83
Table 11. High resolution data used in this study with technical parameters.....	96
Table 12. Shiveluch 2005, 2010, and 2013; and Mount St. Helens (MSH) 18 May, 12 June, and 12 July deposit distributions. ....	102

## LIST OF FIGURES

Figure 1. The location of Shiveluch at the intersection of the Kuril-Kamchatka and Aleutian subduction zones.....	6
Figure 2. ASTER VNIR data of Shiveluch volcano acquired 11 October 2010 (bands 3, 2, 1 in R, G, B, respectively highlights vegetation in red and snow in white). (a) Overview image with white dashed line showing the extent of the 1964 debris avalanche deposit (from Belousov, 1995). White box shows the area in (b). (b) The Shiveluch dome within the 1964 debris avalanche scar. The eastern and western drainage points eroded either side of the 1964 slide blocks at the base of the dome.....	7
Figure 3. The 3 December 2013 block-and-ash flow on Shiveluch (view looking north). This relatively small pulse of material is traveling past Baidarny Ridge with the bulk of the flow directed towards the west and a smaller portion of flow freshly deposited to the east. Photograph courtesy of Yuri Demyanchuk.....	8
Figure 4. Periods of dome growth and heights from September 1980 to October 2016, with the eight collapse events indicated by the grey bars. Dome heights from 1980 to 2013 from Zharinov and Demyanchuk (2008) and Shevchenko et al. (2015), and 2013-2016 heights are estimated from photographs taken by Yuri Demyanchuk. ....	11
Figure 5. ASTER data of the eight collapse scars resulting from the dome-collapse events in the right column (VNIR image with the TIR-derived temperature contours of the dome-collapse scars overlain in the right column). The BAF event (month and year) are labeled in the left column.	

Acquisition dates and other information given in Table 6. Temperature contours are in 10-degree C increments as shown in (b) and all images are oriented with north to the top, as shown in (a).21

Figure 6. ASTER VNIR data of the eight block and ash flow deposits investigated in this study (all images are orientated north): a) 19 May 2001; b) 10 May 2004; c) 27-28 February 2005; d) 18-19 December 2007; e) 25-26 June 2009; f) 27 October 2010; g) 26 July 2013; h) 3 December 2013..... 23

Figure 7. ASTER TIR scenes preceding six of the eruptions included in this study with the dome-collapse scar boundaries that followed them overlain in color. The maximum temperature or the number of pixels that exceed the ASTER TIR saturation temperature of 97°C. The 9 July 2013 scene has the weakest thermal anomaly, and a steam/gas plume covers the top of the area. .... 32

Figure 8. The block-and-ash flow (BAF) area (km<sup>2</sup>), runout distance (km), and planimetric dome collapse areas (scar area, km<sup>2</sup>) of the eight collapse events. .... 37

Figure 9. Photo of the Shiveluch dome taken from the southwest on 21 October 2016 (solid black line denotes the dome surface in this view). The dashed black line depicts the dome surface four days prior (17 October 2010). Following the eruption on 27 October 2010, the dome surface changed dramatically, shown by the white line (after Zharinov and Demyanchuk, 2013). Photo courtesy of Yuri Demyanchuk. .... 38

Figure 10. The Shiveluch 2005 and 2010 block and ash flow deposits originating from partial dome collapse. Left image is a WorldView-02 scene (panchromatic band) acquired on 29 September 2010. Right image is a QuickBird-02 scene (panchromatic band) acquired on 27 August 2013. 41

Figure 11. The nine facies that represent surface characteristics across the 2005 and 2010 main deposit fans and channelized deposits. The colors and numbers correlate to the descriptions on the next page. .... 44



Figure 12. The Shiveluch 2005 BAF main deposit fan area (panchromatic WorldView-02 scene acquired on 29 September 2010). The white boxes and letters indicate areas where the photographs in the following section were taken. The black boxes and letters indicate the areas of the figures that are enlargements of this WorldView-02 scene. a) Figure 15; b) Figure 16b; c) Figure 17; d) Figure 18; e) Figure 19; f) Figure 20; g) Figure 21; h) Figure 22; i) Figure 23; j) Figure 24; k) Figure 25. .... 47

Figure 13. Pyroclastic surge deposit sections with grain-size distributions with relative abundances (measured in the phi size scale) and corresponding sample site. Locations shown in Figure 14. 48

Figure 14. Locations of the surge samples that are described in Figure 13. .... 49

Figure 15. a) surficial lineaments of lower-density andesite clasts on the surface of the 2005 deposit; b) the low-density bands were deposited along flow fronts (field notebook for scale); c) multiple flow fronts lined with the low-density clasts seen in drone footage (three people for scale in the black circle). .... 50

Figure 16. a) Aerial photograph (looking west) of the 2005 main deposit fan. Band of singed trees (mostly larch and stone birch) up to several hundred meters wide bounds the toes of the 2005 block-and-ash flow deposit. The trees were damaged by low-energy, hot, and fine-grained pyroclastic surge that accompanied the block-and-ash flow. Helicopter views from the N (a) and SW (b). .... 51

Figure 17. Sinuous lobate deposit surface with erosional channels on the 2005 main deposit fan. WorldView-02 image acquired on 29 September 2010. .... 52

Figure 18. Singular pulses of material are indicated by bands of low-density material that were deposited at the flow front. a) Thin black lines annotate the bands, thick black lines are major flow

boundaries, yellow lines outline channels, and white arrows indicate areas of remobilization; b) the white bands are visible in the QuickBird-02 scene acquired on 27 August 2010. .... 53

Figure 19. a) knocked down and partly burned trees along the lateral edge of the 2005 deposit. Some of the trees withstood the dynamic action of the block-and-ash flow, but fell down some time later when the bases of their trunks were charred on the contact with the deposit.; b) tree dam at the distal edge of the 2005 main deposit fan, man in circle for scale; c) trees broken and wrapped around a standing tree; d) Bark and branches removed on the stoss side of the tree up to the height of 3.5 m above the surface of the 2005 deposit. The elevation of the damaged tree trunk indicates the thickness of the gas-inflated BAF before its final deposition. .... 55

Figure 20. Four zones of vegetation damage: 1) complete tree removal and/or complete burial by deposit; 2) tree stumps remaining/felled trees in situ; 3) singe zone where dead trees remain standing reaching over 280 m from the BAF deposit; 4) No tree damage. .... 57

Figure 21. a-b) The surface manifestations of degassing structures along the thickest area of the 2005 deposit (Figure 3), with surface discoloration and colored rings (field notebook for scale in white circle); c) a line of degassing structures (indicated by arrows) along the 2005 composite lobate feature, taken by drone near the area of 14a and are similar size of those in the photographs. .... 59

Figure 22. a) laminated water flow deposits with dispersed lenses of coarser clasts (above the white line) in the northern eroded channel which is up to 40 m-wide at this location. The channel is 1~ km long and erodes into the pre-2005 substrate, to a depth of over 18 m in places; b) erosion and deposition (above the white line) into the 2005 deposit along the southern boundary. The dashed line is where erosion took place into preexisting reworked deposits; c) the eroded surface exposing

a higher number of blocks and with sheets of 1964 andesite; d) an eroded channel in the 2005 deposit up to 45 m wide (people for scale). ..... 60

Figure 23. The eroded surface of the 2005 block and ash flow deposit with braided and dendritic patterns. WorldView-02 image acquired on 29 September 2010. .... 61

Figure 24. The distal end of a lobe located along the southern edge of the 2005 deposit. The underlying unit is fines-depleted and has a thicker termination, also visible on the other side of the erosional channel. The fines-poor unit is overlain by a matrix-supported unit. .... 62

Figure 25. The southern wall of a cross section cut by the Baidarnaya River with reversely-graded units indicated by white arrows. Note that no fresh deposits are on the northern (right) side of the channel. .... 63

Figure 26. The Shiveluch 2010 BAF deposit (panchromatic QuickBird-02 scene acquired on 27 August 2013). The white boxes and letters indicate areas where the photographs in the following section were taken. The black boxes and letters indicate the areas of the figures that are enlargements of this WorldView-02 scene. a) Figure 27a, c; b) Figure 27b, d; c) Figure 28a d) Figure 28b; e) Figure 29; f) Figure 30; g) Figure 31; h) Figure 32 (WorldView-02 scene acquired on 19 March 2011 used in Figure 29 due to shadow in the 17 August 2013 scene); i) Figure 33. .... 64

Figure 27. a) The main deposit fan of the 27 October 2010 block and ash flow deposit and the channelized section that continued for 5,400 m; the composite lobate features are shown in b and c with black lines in d and e indicate the lobe fronts. White arrows indicate the location and direction of remobilization. Images are of the QuickBird-02 scene acquired on 27 August 2013. .... 65

Figure 28. Herringbone structures on the 2010 deposit a) 8,000 m and b) 8,500 m from the dome (QuickBird-02 scene acquired on 27 August 2013). ..... 66

Figure 29. Feathery lobes in the 2010 deposit, 11,000 m from the dome. Here, the distal deposit was emplaced onto the hummocky 1964 debris avalanche deposit (QuickBird-02 scene acquired on 27 August 2013)..... 67

Figure 30. Grain-size distributions with relative abundances measured in phi. The samples pf2010b and 2010/2 were overlying 2010a and 2010/1, respectively. Locations are shown on the QuickBird-02 scene acquired on 27 August 2013. .... 68

Figure 31. Cross section through the channelized 2010 deposit ~14,000 m from the dome where the deposit is cut down to the original riverbed surface. .... 69

Figure 32. Varying block contents over a short distance with the smoother block-poor deposit surface in the upper left of the image. Black arrow indicates flow direction and white arrows indicate deposit remobilization (QuickBird-02 scene acquired on 27 August 2013)..... 70

Figure 33. Bench and Scallop topography (area indicated in inset image) with black arrows indicating four out of the ~30 benches present. Black specks in the image are large blocks on the deposit surface. .... 71

Figure 34. Large blocks of dome rock, a) 12 km from the dome base on the 2005 deposit, b) 15 km from the dome base in the 2005 deposit, c) 10 km from the dome base in the 2010 deposit, and d) 13 km from the dome base in the 2010 deposit..... 73

Figure 35. Three stratigraphic sections in the 2005 main deposit fan that show the discontinuous nature of the units within a 550 m distance. .... 77

Figure 36. a) small surface hummocks are formed over and around blocks or portions of logs; b) 0.9 x 3.7 m hummock in the channelized 2010 deposit >14 km from the dome (rock hammer for

scale in white circle). A portion of tree trunk/branch is protruding out the side; c) small surface hummocks (white arrows) on the 2010 deposit >8 km from the dome. Flow direction is indicated by the arrows. .... 81

Figure 37. The two best-fit LAHARZ simulated inundation results for the Shiveluch 2005 and 2010 BAF deposits on the SRTM DEM. The deposit outlines are shown in black. .... 84

Figure 38. a) Mount St. Helens volcano (ASTER VNIR data acquired 08 August 2001. The white box outlines the area of the pumice plain area that is the focus for this study (see Figure 39 for more detail). False color image RGB: 3,2,1) and; b) Shiveluch volcano with the 2005 and 2010 main deposits with black outlines, and the 2013 deposit outlined in white. ASTER VNIR data acquired 06 June 2013. False color image RGB: 3,2,1). .... 88

Figure 39. The preserved area of the pumice plain pyroclastic flow deposits are shown in the white box (in a and within inset) in a) the 2009 lidar data; and b) an OrbView-3 image (Table 11) acquired on 5 October 2004. Erosional channels are visible throughout the pumice plain..... 95

Figure 40. The Mount. St. Helens Pumice Plain shown in three overlapping aerial photographs. The 18 May 1980 (black outlines), 12 June 1980 (pink outlines), and 22 July 1980 (blue outlines) delineate pyroclastic flow deposits. Yellow boxes indicate areas shown in Figure 44. .... 98

Figure 41. Componentry plots for the Mount St. Helens 12 June pyroclastic flow deposit, and the Shiveluch 2005 and 2010 deposit. Plot titles indicate original sample names. .... 100

Figure 42. Abundance of ash and lapilli in the Shiveluch 2005 (-05-pf) and 2010 (pf2010) BAFs (Chapter two); b) and Mount St. Helens June 12 pyroclastic flow deposits (Pallister et al.,2017). The upper-most units are outlined and indicated by arrows. .... 101

Figure 43. Differing degrees of surface relief in the 18 May deposits: a) thicker lobate deposits with shadows visible in the aerial images due to the thickness of the lobes; b) low-relief surface

morphologies formed by thinner deposit in the darker areas of the 18 May deposits. Photographs from the USGS 31 July 1980 survey. .... 103

Figure 44. Composite lobate features in the: a) 18 May 1980 deposit; and b) 12 June 1980 deposits on the Pumice Plain. Locations given in Figure 40. .... 105

Figure 45. Lobate morphologies in the 18 May 1980 pyroclastic flow deposits with white arrows showing flow direction: a) lobe set with stacking of deposit material in the same place and each subsequent pulse is shorter; b) cats-paw or lobe and cleft morphology; c) stacked sets of narrow, elongate lobes forming off the side of a flow; d) entire section of stacked lobes with black arrows indicating feature locations; e) elongate overlapping lobes originating from the same feeder channel; f) sheet-like deposit with poorly-defined lobate terminations perpendicular to the main flow direction. Images are from the 31 July aerial survey..... 107

Figure 46. Lobes of the 26 July 2013 Shiveluch BAF deposits, a) sharp terminations with coarser clasts concentrated along the flow boundaries 620 m from the dome; b) well-defined levees and sharp flow boundaries 1070 m from the dome; c) diffuse flow boundaries 1600-1800 m from the dome, d) diffuse flow boundaries 3150 m from the dome..... 109

Figure 47. Secondary levees at MSH. a) As mapped in a 2009 lidar survey image and; b) the same location with levee locations overlain on a USGS 31 July 1980 aerial photograph..... 110

Figure 48. Secondary levees at MSH with locations shown by the black (a) and white (b) arrows on the Google Earth image in c..... 111

Figure 49. Scalloped remobilization scarp in the 12 June 1980 pyroclastic deposit on the Pumice Plain. Area is show in the white box in (b), which is an aerial photograph taken during a USGS survey on 8 July 1980. Black arrows indicate flow direction..... 112

Figure 50. Remobilization scarps in the Shiveluch deposits: a) scarp headwall of a curvilinear scarp (area indicated in the white box shown in c) in the northern section of the 2010 deposit; b) the sidewall of the arcuate scarp (area indicated in the white box in d) with person (in white circle) for scale; c) bench topography above the curvilinear scarp in the 2010 deposit fan; d) nested arcuate scarps in the 2005 deposit..... 112

Figure 51. The MSH 18 May sheet-like pyroclastic flow deposits that contain the surface ridge-and-trough features shown in more detail in: a) Figure 52; b) Figure 53; and c) Figure 54. The area is indicated by the white box within the inset image. .... 114

Figure 52. The USGS September 2009 data series 904 Lidar survey over the sheet-like section that contains surface ridges. Small black arrows (in a and b) indicate a few examples where a ridge is immediately followed by a furrow. An aerial photograph from the 31 July 1980 survey is shown in (c) over the same area. .... 115

Figure 53. Elevation profiles across the NW section of the MSH 18 May pyroclastic flow deposits taken from the USGS September 2009 Lidar survey (data series 904) and overlain on a USGS aerial photograph taken in the 31 July 1980 survey. .... 116

Figure 54. Elongate lobe containing multiple parallel ridges and toes along the lateral edges within the 18 May deposit: a) Lidar surface morphology sections shown in b; b) 2009 lidar survey with surface survey lines; c) aerial photograph taken 8 July 1980, the same area shown in b, yellow triangle indicates the photograph d; d) side view of the NE section showing multiple lobes overlaying each other. Area of interest is shown in inset. .... 117

Figure 55. a-b) Herringbone features in the Shiveluch 2010 deposit upstream from topographic highs, from Chapter two; b) compression ridges in the remobilized deposit within the arcuate

scarps in the Shiveluch 2005 deposit; d) compression ridges on the surface of 2010 deposit. White arrows show flow direction, black arrows indicate examples of compression ridges. .... 118

Figure 56. Examples of the similar morphological features across the MSH and Shiveluch PDC deposits, where present. .... 120

Figure 57. a) Lascar 1993 lobate pyroclastic flow deposits (Jessop et al., 2012); b) lobate dome collapse BAF deposits from the 11 April 1997 eruption of Soufriere Hills volcano (Cole et al., 2002); c) lobate flow front within the 2006 BAF on Merapi volcano (Gomez et al., 2009); d) BAF lobate deposits of the April 16-17 1991 eruption of Colima volcano; e) multiple distal lobes in the 1993 Lascar column collapse pyroclastic flow deposits (Sparks et al., 1997); f) distal lobate ends of the 1990-1995 Unzen volcano BAF deposits (Miyabuchi, 1999); g) lobate deposits..... 124

Figure 58. Sequence showing the formation of the rounded ridges in Figure 15. a) a flow front of the pyroclastic flow section moving with relatively similar velocities across the front; b) friction possibly caused by interaction with underlying topography, or material being emplaced directly ahead, causing the center to slow down; c) the material towards the edges slows and forms a rounded; d) the lateral edges of the lobe have curved around the central material and a smaller toe has broken out through the outermost edge. This sequence has occurred multiple times from the front to the back of the feature, and stacking from the base to the top. .... 126



## PREFACE

I have loved volcanoes for most of my life and there have been hundreds of people along the way who have helped me on this journey. Thank you to all of you around the world who have been a part of this journey to Ph.D. Thank you to my colleagues and fellow volcano-lovers who have offered support, encouragement, technical advice, and comments and edits.

Thank you Sasha Belousov and Marina Belousova for your invaluable help with field work and writing. Life-after-Kamchatka is indeed better.

Thank you to those at the Cascades Volcano Observatory who provided feedback and assistance with field work – John Pallister, Alexa Van Eaton, Heather Wright, Jim Vallance, Tom Pierson, and Kristen Sweeney. Thank you Victoria Silvagni for assistance in the field and with data collection. Thank you, Brittany Brand for aerial photography data and conversations about the Pumice Plain.

Thank you, Alison Graettinger, my friend and co-blogger, for the years of discussions around everything volcanoes and the extensive help throughout this Ph.D.

Thank you Erik Klemetti, Laura Walkup, Sally Kuhn Sennert, and Dawn Ruth for comments, discussions, and encouragement. Thank you, Rudiger Escobar Wolf, for your LAHARZ matlab code, and for the assistance in running the model.

Thank you and to my wonderful Whanau back in Aotearoa – Mum, Dad, Ian, Jayde, all my Aunts, Uncles, Cousins, Grandparents, and Angela. Your support through the years of my chasing volcanoes means the world to me. Arohanui.

Thank you to all of my colleagues around the world who engage in outreach and science communication with me. Conversations with you all has been encouraging, inspiring, and fun! I have learned so much from all of you and have been inspired by your work.

Thank you to Mike for taking me on as a Ph.D. student and getting me here, to the USA. Thank you, Dan, Bill, Nadine, Charlie, Mark, and Eitan for the advice over these past five years. Thank you for faculty and friends in the Department of Geology and Environmental Science for the comradery, and for listening to me get excited about volcanoes.

Thank you to the organizations for the following grants and awards that funded this research, field work, data, and presenting my research at conferences: NASA NESSF, USGS Jack Kleinman Grant for Volcano Research, Digital Globe Imagery Grant, Kenneth P. Dietrich School of Arts and Sciences Tuition Supplement, GSA Graduate Student Research Grant, University of Pittsburgh International Studies Fund, Hewlett International Grant (University of Pittsburgh), AGU 2015 Fall Meeting Student Travel Grant, AEG Foundation Lemke Scholarship, AGU 2015 Fall Meeting Outstanding Student Presenter Award (OSPA), The Henry Leighton Memorial Graduate Scholarship, the IAVCEI grant for inscription fee to attend Cities on Volcanoes 9 conference, and Bob Holzworth at the WWLLN (World Wide Lightning Location Network).

Kia Kaha!

## 1.0 INTRODUCTION

Shiveluch volcano in Kamchatka, Russia, is one of the world's most active dome-building volcanoes producing some of the largest historical block-and-ash flows of any volcano. They result from partial collapse events that initiate at different locations as dome growth occurs. The southerly distribution direction is influenced by topographic control exerted by the 1964 horseshoe-shaped crater formation and subsequent debris avalanche deposit. The dome and resulting deposits are investigated using the Advanced Spaceborne Thermal Emission and Reflection Radiometer (ASTER) thermal infrared (TIR), shortwave infrared (SWIR), and visible-near infrared (VNIR) satellite data for the period from 2001 to 2013. Linking the deposit distribution to the size, location, and temperature profiles of the dome collapse area provides a basis for determining similar future hazards at Shiveluch and other dome-forming volcanoes. Eight large block-and-ash flow deposits and collapse scars are investigated, which were formed during eruptions or collapse events in 2001, 2004, 2005, 2007, 2009, 2010, and two in 2013. The largest runout distance reached 19 km from the uppermost extent of the collapse scars. Over the 12 years of this period of investigation there is no trend in size or runout distances of the flows through time, although the largest dome collapse events occurred when the dome exceeded a relative height (from dome base to top) of 500 m. Where data prior to the events are available, the locations of pending collapse are preceded by a thermal anomaly, although the anomalous area does not generally correlate with the size of the collapse event. Here, we give quantitative data for the large

deposits of a long-lived dome-forming eruption. Volcanic hazard analyses and mitigation at volcanoes with similar block-and-ash flow emplacement behavior may be improved with detailed, synoptic studies of the prolonged dome-building and collapse activity at Shiveluch volcano.

The 2005 and 2010 block-and-ash flow deposits are two of the largest known historic block-and-ash flow fields, globally. The deposits were produced during retrogressive pulsatory dome collapse events that occurred over 6-9 hour-long eruptions on 27-28 February 2005 and 27 October 2010. These events emplaced material up to 19 km from the dome and inundated areas of 24.1 and 22.3 km<sup>2</sup>, respectively. The deposit surfaces contain overlapping lobate deposits, compaction ridges, levee and channel morphologies, degassing structures, abundant large dome blocks, and large areas of syn- or immediately post-depositional remobilization shown by bench scallop and arcuate scarps. The block-and-ash flows produced associated pyroclastic surges that killed vegetation to nearly 300 m beyond the main deposits. The 2005 dome collapse event produced a block-and-ash flow that emplaced a large fan deposit and associated surge that destroyed a 10 km<sup>2</sup> area of forest. The October 2010 event also produced a large fan deposit with a distal channelized deposit that extended an additional 5.4 km beyond the fan along the Kabeku River channel. Since deposition, fluvial erosion has resulted in large areas comprised of dendritic and braided channel systems.

The surface morphology seen in satellite data, and cross-section stratigraphy give insight into the pulsatory nature of the dome collapse events, the final moments of deposition, and the subsequent erosion of the deposits in a high-latitude region where the deposits are relatively well preserved. Investigating such large-scale block-and-ash flow fields gives a rare opportunity to understand the extent of extreme large end-member dome collapse events and their runout distances in channelized and non-channelized environments.

Variations in the deposit morphology of different pyroclastic density current types, such as the Shiveluch block-and-ash flow deposits, provide insight into the late stage transportation and deposition processes. Near-real time field-based studies on pyroclastic deposits are rare due to the fact that they are time-consuming, costly, and very dangerous, all of which can be mitigated through approaches using remote sensing data. Morphological features of deposits at Shiveluch and Mount St. Helens volcanoes are described using a combination of satellite, aerial, and field data, to identify characteristics indicative of different eruption mechanisms (column collapse and dome collapse) and source materials (pumice and dense dome rock). Both eruption styles produce unsteady flows that form a range of morphologies including sheet-like deposits, channel and levees, transverse compression ridges, lobate terminations, and retrogressive stacking of deposit pulses. The sequence of deposition is described with several phases recognized that show a general trend in decreasing distance from vent/dome: 1) pulsatory sheet-like deposition; 2) development of distinct lobate deposits; 3) retrogressive stacking of deposits with channel and levee systems; 4) deposit remobilization. Some of these phases repeat throughout the eruption and not all are present in each deposit. The two deposit types are distinguished by distinctive lobe morphologies, such as elongate lobes with distinct, steeper lobe and cleft features (pyroclastic flow) vs. fanning deposits with tapering flow fronts containing numerous small toes (block-and-ash flow). This comparison of variations in deposit surfaces gives insight into the development of pyroclastic density current deposits in the final moments of deposition. These deposit surfaces are described in outcrop-scale in the field and using high-resolution aerial and satellite imagery, evaluating the morphologies for the purpose of characterizing deposits and interpreting late-stage flow behavior.

## **2.0 PARAMETRIC ANALYSIS OF LAVA DOME COLLAPSE EVENTS AND PYROCLASTIC DEPOSITS AT SHIVELUCH VOLCANO, KAMCHATKA, USING ORBITAL VISIBLE AND INFRARED DATA**

### **2.1 INTRODUCTION**

Volcanic lava domes are solidified/semi-solidified plugs of lava extruded at a volcano. The partial collapse of these lava domes can produce block-and-ash flow (BAF) deposits, typically with minimal to no warning (Calder et al., 2015). The prolonged eruption duration and unpredictable nature of dome-collapse events can result in fatalities, social disruptions, or permanent evacuations of surrounding populations either because of the BAF or related/detached pyroclastic surges (Charbonnier et al., 2013a and references therein). Past well-known examples of these prolonged eruptions include eruptions of Mt Pelée (Fisher and Heiken, 1982), Unzen volcano (Miyabuchi, 1999), Soufrière Hills volcano (Cole et al., 2002), and Merapi and Sinabung volcanoes (Surono et al., 2012; Gunawan et al., 2017). The prolonged nature of cyclic eruptions of dome growth and destruction are disruptive to local communities, such as at Sinabung volcano in Indonesia, where the current eruption (since 2013) has damaged or destroyed 10 villages and two hamlets, and has displaced almost 10,000 people (Yulianto et al., 2016, Andreastuti et al., 2017). Unlike Sinabung, Shiveluch is in a remote area of northern Kamchatka (Klyuchi, the nearest town is 31 km from the edge of the debris fan). Shiveluch was selected for this study due to the prolonged dome-forming eruption that has produced of BAF deposits ranging in size and distribution. Within the current eruption period, eight dome-collapse events and the resulting BAF deposits were selected, for which orbital VNIR, SWIR, and TIR data from the ASTER sensor are

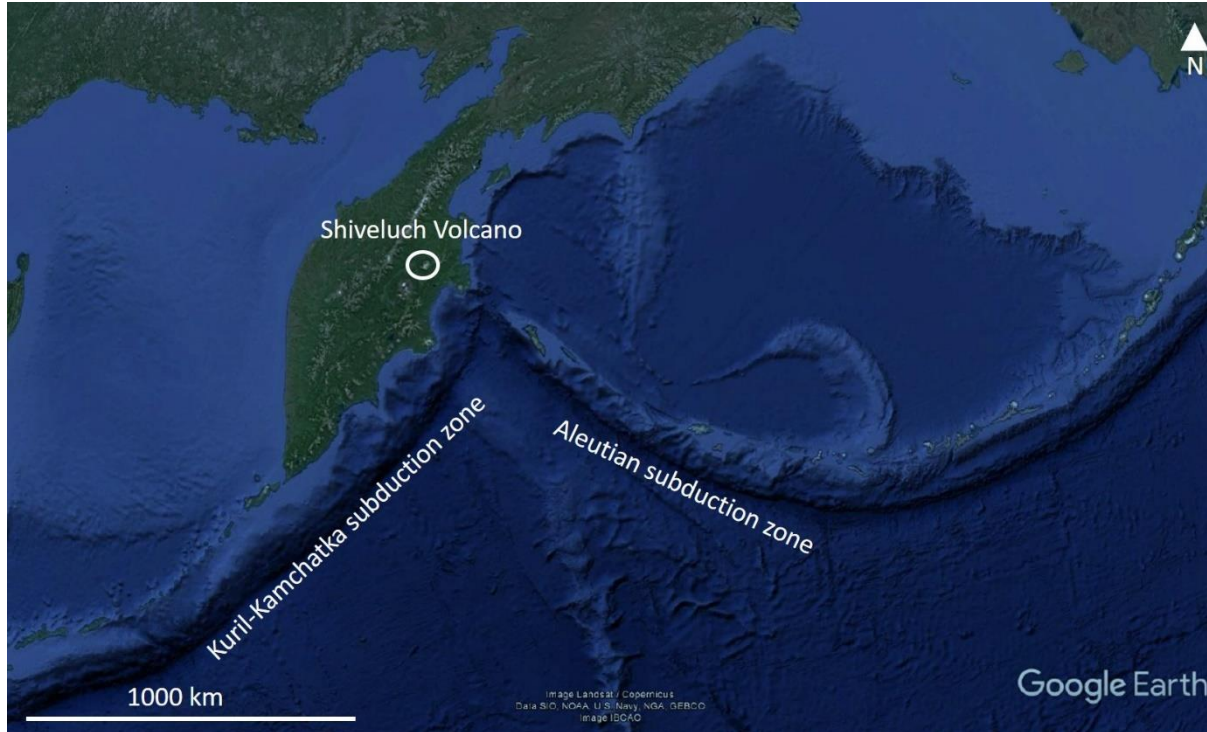
available before and after the collapse events. By investigating these events, a range in BAF deposit sizes are compared to activity at the dome, and the conditions that result in these distributions are assessed.

In retrospect, the relationships between the pre-collapse areas of elevated thermal output and the size and location of the following collapse events are investigated in order to assess the value of TIR data for identifying pre-dome-collapse indicators at Shiveluch. For this study, I characterize the dome-collapse scars using planimetric areal extent, location of source areas on the dome, and temperature profiles. The deposits are then characterized using spatial distribution (including runout distance), maximum width, and dome-collapse volume where available. By doing this, the evolution of this long-lived dome-building eruption at Shiveluch is investigated, through analyzing the dome-collapse events and the resulting BAF deposits. This clarifies the impact of large BAFs over the duration of a lengthy eruption and constrains the maximum size of deposits that result from dome-collapse events.

### *Study Area*

Shiveluch volcano (also spelled Sheveluch) is located in the northern Central Depression of Kamchatka, where the Kuril-Kamchatka and Aleutian subduction zones intersect (Figure 1), and is the northern-most active volcano in Kamchatka. The edifice is divided into Old Shiveluch (3335 m) that was partially destroyed by a  $>10 \text{ km}^3$  debris avalanche with an age of 10 ka, and Young (Molodoy, in Russian) Shiveluch (2763 m) that was formed after the collapse (Belousov et al., 1999). Shiveluch has undergone at least seven large edifice collapse events, dated at approximately 10,000, 5700, 3700, 2600, 1600, 600 BP, and 1964 AD, with the failure frequency attributed to the high supply rate of viscous andesite magma (Belousov et al., 1999). Such high

magma supply rates also result in rapid reconstruction of the volcanic cones following collapse

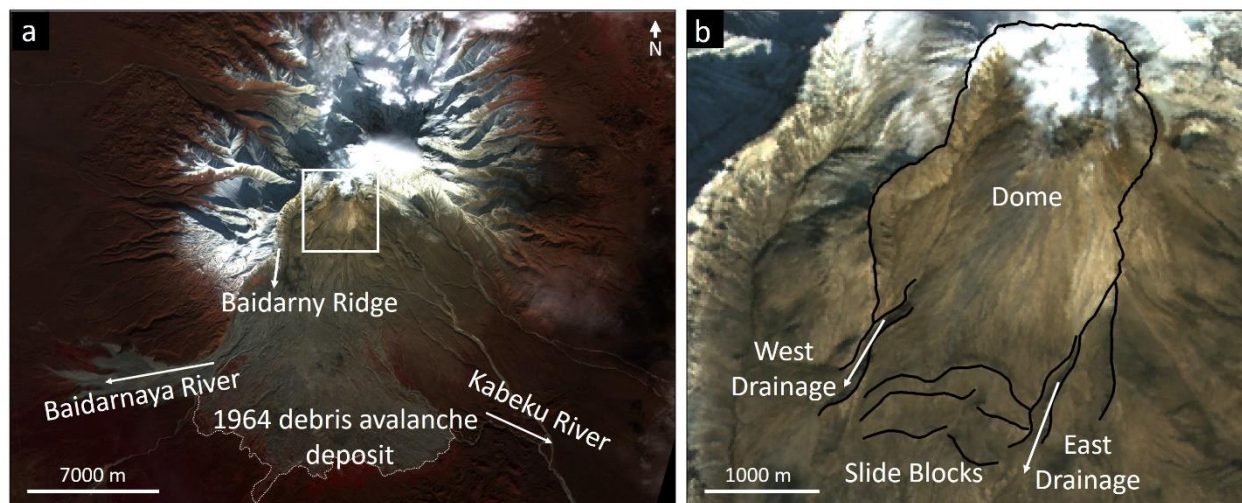


**Figure 1. The location of Shiveluch at the intersection of the Kuril-Kamchatka and Aleutian subduction zones.**

events. Young Shiveluch has formed in the 10 Ka collapse scar of Old Shiveluch and has subsequently experienced six major eruptive periods, mainly consisting of dome formation (Belousov, 1995 and references therein). A 1500 m-diameter horseshoe crater formed during a collapse around 600 BP and domes have since cyclically filled the crater (Belousov, 1995 and references therein). The cone of Young Shiveluch is composed of overlapping domes, short lava flows up to 100 m thick, and volcanic breccias; a low-angle volcanoclastic fan extends to more than 20 km to the south (Dirksen et al., 2006). The currently-active dome is situated in the most recent 1750 m-wide south-facing collapse crater, which formed in 1964 (Figure 2). The dome was formed through several cycles of growth and collapse during the current 16-year-long eruption. BAFs result from partial dome-collapse and are directed to the SE and SW flanks of the volcano



by barriers consisting of two large debris avalanche blocks (Toreva blocks) that were emplaced during the 1964 collapse (Belousov, 1995). After being directed SE and SW, the majority of the flows then travel along the eastern and western edges of a 1964 hummocky debris avalanche deposit fan (Figure 2a).



**Figure 2.** ASTER VNIR data of Shiveluch volcano acquired 11 October 2010 (bands 3, 2, 1 in R, G, B, respectively highlights vegetation in red and snow in white). (a) Overview image with white dashed line showing the extent of the 1964 debris avalanche deposit (from Belousov, 1995). White box shows the area in (b). (b) The Shiveluch dome within the 1964 debris avalanche scar. The eastern and western drainage points eroded either side of the 1964 slide blocks at the base of the dome.

### *Terminology*

Here, term ‘block-and-ash flow’ describes the motion of a mass of rock (breaking into smaller fragments during movement), ash, and hot gas that results from dome-collapse (Figure 3) (Bursik et al., 2005). The BAFs at Shiveluch are produced mainly by Merapi-type events, in which dome-collapses are the result of gravitational failure (Bardintzeff, 1984). The term ‘pyroclastic

density current' (PDC) is used when the initiation mechanism (such as dome or column collapse) is unclear.



**Figure 3. The 3 December 2013 block-and-ash flow on Shiveluch (view looking north). This relatively small pulse of material is traveling past Baidarny Ridge with the bulk of the flow directed towards the west and a smaller portion of flow freshly deposited to the east. Photograph courtesy of Yuri Demyanchuk.**

For this study, we investigate eight dome collapses and the resulting block-and-ash flow deposits for which ample orbital VNIR, SWIR, and TIR data from the ASTER sensor are available. We characterize the dome collapse scars using planimetric areal extent, location on the dome, and temperature profiles. The deposits are then characterized using spatial distribution (including runout distance), maximum width, and dome collapse volume where available. Precursory thermal activity on the dome is investigated using ASTER thermal (TIR and SWIR) data and the

Kamchatka Volcanic Eruption Response Team (KVERT) reports. The eruption details are compiled from KVERT Volcano Observatory Notification to Aviation (VONA) reports available online, as well as from various scientific publications in local Russian journals.

### **2.1.1 Summary of the recent eruption history of Shiveluch**

Volcanic activity prior to 2001 has been described by Belousov (1995), Gorelchik (1996), Fedotov, et al. (2004), Zharinov and Demyanchuk (2008), Gorbach and Portyagin (2011), and Zharinov and Demyanchuk (2013). Three main recent dome-forming cycles have since occurred in 1980-1981, 1993-1995, and 2001-onwards (Fedotov, S. A., et al., 2004). Dome growth rates during the current cycle have ranged from 150,000 to 700,000 m<sup>3</sup>/day (approximately 2 to 8 m<sup>3</sup>/s) (Table 1). Since 1980, the dome height has been increasing, with intermittent reductions in height due to collapse events (Figure 4).

Since recent dome growth began in 1980, the style of growth has largely been exogenous with intermittent periods of endogenous growth (Shevchenko et al., 2015). Through cycles of dome growth and collapse, the dome has been constructed of overlapping lobes. Viscous, blocky andesite lavas have formed radial, bilateral symmetrical, and irregularly spreading lobes or petals throughout the eruption period (Dirksen et al., 2006; Ramsey et al., 2012; Shevchenko et al., 2015). A talus cone surrounds the edifice and extends to the 1964 debris avalanche blocks. Explosions and partial collapses commonly produce excavated explosion pits and collapse chutes or scars (Shevchenko et al., 2015). Shiveluch also displays a range of eruptive activity including small to regionally extensive ash plumes, pyroclastic surges, and associated lahars (Fedotov, et al., 2001; Zharinov, and Demyanchuk, 2008; Zharinov, and Demyanchuk, 2013; Shevchenko, and Svirid,

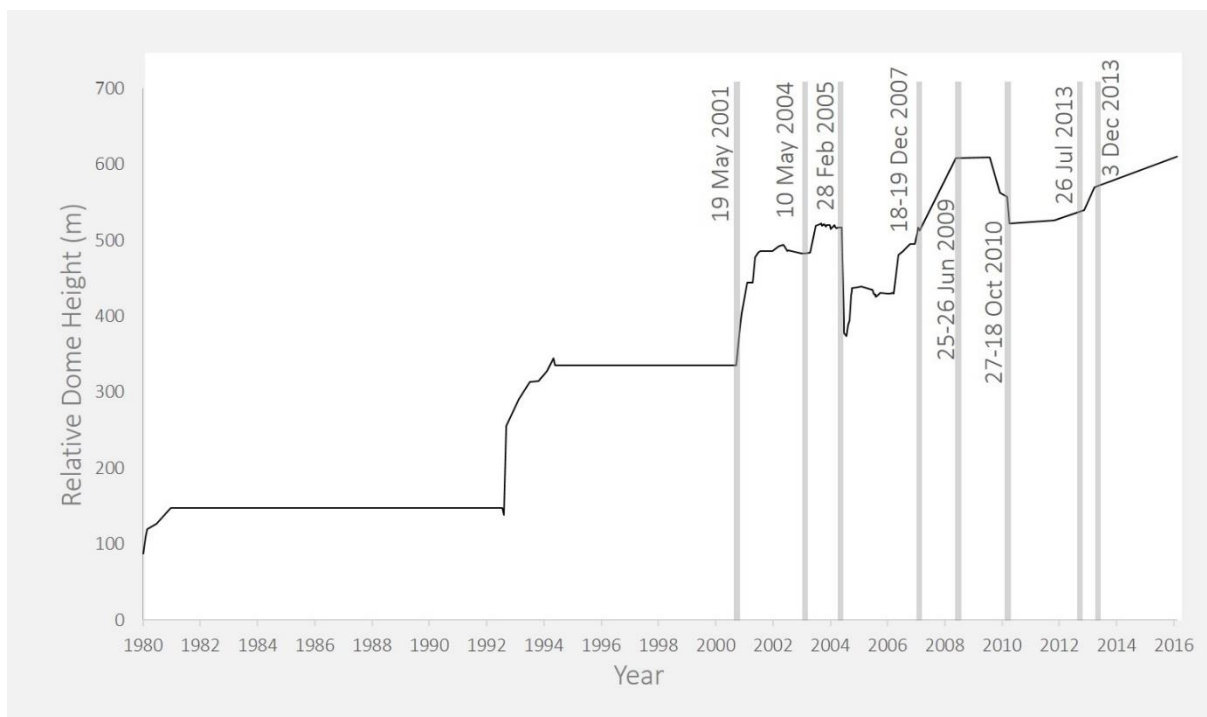
2014). Shiveluch dome-collapse events are also hazardous to aircraft, as ash plumes can reach flight levels and extend hundreds of kilometers from the volcano during collapse events.

Zharinov and Demyanchuk (2008 and 2013) give detailed accounts of lava dome dimensions (heights, widths, volumes, and profiles), viscous lava extrusion, gas emissions, and seismicity (volcanic tremor, tectonic earthquakes) from 2001 to 2012. The 0.63 km<sup>3</sup> andesite to dacite dome (2012 volume in Shevchenko et al., 2015) began its current cycle of growth in April 2001 after a period of quiescence following activity in 1993-1995 (Gorbach, 2006; Shevchenko and Svirid, 2014). The SiO<sub>2</sub> content of the lavas has increased over time, from 58.5% in 1964 and about 61% in 2001 to as much as about 63% in 2007-2008 and 2013 (Table 2). The current dome is composed of hornblende-plagioclase andesite to low-silica dacite (Gorbach et al., 2016). During the period 2001-2013, Shiveluch has undergone two major cycles of dome growth including multiple collapse events based on relative dome height, with the largest collapse events occurring when the maximum height of the dome stabilized for an extended period at approximately 520 and 560 m.

The collapse events within the current eruption period have been chosen for more detailed analysis, based on size and availability of data. The eight collapse event details, where available, shown in Table 3, and eruption descriptions are given in Appendix A.

**Table 1. Available dome growth rates from Shevchenko et al., 2015 and references therein.**

<b>Date range</b>	<b>Rate (m<sup>3</sup>/day)</b>
23 August to 22 October 1980	186,000
4 April to 24 August 1993	810,000
1993 to 1995	280,000
29 April 2001 to 16 May 2001	700,000
16 May 2001 to 7 October 2003	320,000
7 October 2003 to 21 August 2005	>175,000
21 August 2005 to 22 November 2010	≥220,000
22 November 2010 to 12 July 2012	150,000



**Figure 4.** Periods of dome growth and heights from September 1980 to October 2016, with the eight collapse events indicated by the grey bars. Dome heights from 1980 to 2013 from Zharinov and Demyanchuk (2008) and Shevchenko et al. (2015), and 2013-2016 heights are estimated from photographs taken by Yuri Demyanchuk.

**Table 2.** Summary of Shiveluch eruptive product composition over time.

Year	wt.% SiO <sub>2</sub>	Reference
1964 eruption avg.	58.49	Bindeman et al., 2004, Kepezhinskas et al., 1997, Hochstaedter et al., 1996, Dirksen et al., 2006
1980 eruption avg.	60.33	Pineau et al., 1999, Dirksen et al., 2006
1993 eruption avg.	61.09	Tolstykh et al., 2000, Dirksen et al., 2006
1995 eruption avg.	60.62	Tolstykh et al., 2000, Dirksen et al., 2007
2001	61.27-61.81	Dirksen et al., 2006; Gorbach et al., 2016
2002	62.39	Dirksen et al., 2006
2004	62.74-64.02	Gorbach, 2006, Gorbach et al., 2016
2005	61.19-62.65	Gorbach et al., 2016
2007-08	60.55-63.48	Gorbach et al., 2016
2013	60.84-63.03	Gorbach et al., 2016

**Table 3. Available parameters for the eight Shiveluch dome collapse events.**

Eruption date	Eruption start time	Eruption end time	Eruption length (hours)	Intense activity length (hours)	Ash plume height (km a.s.l.)	Ash plume travel distance/direction	Ash fall area (km <sup>2</sup> )	Max. flow extent	Dome height before (m)	Dome volume (km <sup>3</sup> )	Dome collapse volume (km <sup>3</sup> )	Dome height reduction	Total eruptive mass/volume	Aviation Color Code	References
19-May-01	17:05			2	10	20 km N-W		13.7	335	0.19 (16 May 2001)		0			Fedotov et al., 2001; KVERT report 19 May 2001; Shevchenko et al., 2015
10-May-04	01:10			5	8-11			8.8	521	0.47 (7 Oct 2003)	0.04				Girina et al., 2004; Shevchenko and Svirid, 2014; Zharinov and Demyanchuk 2007; Shevchenko et al., 2015
27/28-Feb-05	18:25		6.8	1.7	8-9		24,800	17.8	520		0.11	125 m	0.2 km <sup>2</sup>	Red	Zharinov and Demyanchuk, 2008; Shevchenko and Svirid, 2014; Gorbach et al., 2016
18/19-Dec-07	18:23 (18 Dec) 20:00 (19 Dec)	02:45 (19 Dec) 23:00 (19 Dec)	8 3		4.4-6	130 km W 300 km S-SW		12.7		0.36				Orange	KVERT Report 19 Dec 2007;
25/26-Jun-09					5			6.4						Orange	KVERT Report 2 July 2009
27-Oct-10					>12	2500 over Pacific Ocean	2000	19.0	563	0.54 (22 Nov 2010)	0.28		7.8 million tons	Red	KVERT Reports 28 Oct 2010; 30 Oct 2010; Dvigalo et al., 2011; Zharinov and Demyanchuk, 2013; Shevchenko et al., 2015
26-Jul-13	22:55				10	520 km SE		11.6		0.63 (12 July 2012)				Red	KVERT Report 1 Aug 2013; Shevchenko et al., 2015
3-Dec-13	13:25	18:58			8-9	>500 km N		13.6						Red	KVERT Report 3 Dec 2013;

## 2.2 METHODOLOGY

### *ASTER Data*

Several studies have applied TIR data to active volcanic domes, for example: Mount St. Helens in 2004-05 (Vaughan et al., 2005; Schneider et al., 2008), Chaitén (Bernstein et al., 2013), Bezymianny (Ramsey and Dehn, 2004; Carter et al., 2007), and Shiveluch (Ramsey et al., 2012). These studies, using data acquired from ground-based cameras, airborne sensors, and orbital instruments, determined dome-growth styles, surface structures/textures, and detected episodes of new activity.

For this study, I collected archival ASTER data with minimal cloud cover (cloud absent over the dome or the deposit of interest). The data spanned the time range preceding and following each eruption episode (Table 4). ASTER data are acquired by three different subsystems: 15 m resolution 0.5-1.0  $\mu\text{m}$  VNIR, 30 m resolution 1.0-2.5  $\mu\text{m}$  SWIR, and 90 m resolution 8-12  $\mu\text{m}$  TIR.

**Table 4. ASTER VNIR, SWIR, and TIR data used in this study.**

<b>Acquisition</b>	<b>Product ID</b>	<b>Product Name</b>	<b>Day/Night</b>	<b>Scene ID</b>
19-May-01	AST_09T	Surface Radiance TIR	Night	SC:AST_L1A.003:2003153825
19-May-01	AST L1B	Surface Radiance SWIR	Night	SC:AST_L1A.003:2003153825
14-Feb-02	AST_07XT	Surface Reflectance VNIR	Day	SC:AST_L1A.003:2006045159
11-May-04	AST_09T	Surface Radiance TIR	Night	SC:AST_L1A.003:2023494312
4-Jun-04	AST_07XT	Surface Reflectance VNIR	Day	SC:AST_L1A.003:2024291013
4-Jun-04	L1B	Surface Radiance SWIR	Night	SC:AST_L1A.003:2024291013
23-Feb-05	L1B	Surface Radiance SWIR	Night	SC:AST_L1A.003:2030456561
12-Mar-05	AST_07XT	Surface Reflectance VNIR	Day	SC:AST_L1A.003:2028072070
12-Mar-05	AST_09T	Surface Radiance TIR	Day	SC:AST_L1A.003:2028072070
29-Mar-05	L1B	Surface Radiance SWIR	Night	SC:AST_L1A.003:2028324137
21-Nov-07	09T	Surface Radiance TIR	Night	SC:AST_L1A.003:2062848883
22-Dec-07	AST_07XT	Surface Reflectance VNIR	Day	SC:AST_L1A.003:2064011999
23-Dec-07	AST_09T	Surface Radiance TIR	Night	SC:AST_L1A.003:2064043505
23-Dec-07	L1B	Surface Radiance SWIR	Night	SC:AST_L1A.003:2064043505
27-May-09	AST_09T	Surface Radiance TIR	Night	SC:AST_L1A.003:2073834400
30-Jul-09	AST_09T	Surface Radiance TIR	Night	SC:AST_L1A.003:2075202177
29-Jul-09	AST_07XT	Surface Reflectance VNIR	Day	SC:AST_L1A.003:2075176798
11-Oct-10	AST_09T	Surface Radiance TIR	Day	SC:AST_L1A.003:2081621953
07-Dec-10	AST_07XT	Surface Reflectance VNIR	Day	SC:AST_L1A.003:2082480246
07-Dec-10	09T	Surface Radiance TIR	Day	SC:AST_L1A.003:2082480246
23-Aug-13	AST_009T	Surface Radiance TIR	Day	SC:AST_L1A.003:2126554976
23-Aug-13	AST_07XT	Surface Reflectance VNIR	Day	SC:AST_L1A.003:2126554976
16-Feb-13	09T	Surface Radiance TIR	Night	SC:AST_L1A.003:2122809877
30-Jan-14	AST_07XT	Surface Reflectance VNIR	Day	SC:AST_L1A.003:2130529870

The use of SWIR data allows for the analysis of higher temperatures on the dome, while TIR data are sensitive to lower temperatures that are spatially predominant across the dome. The SWIR data have three different gain settings available to minimize potential saturation, however the SWIR subsystem failed in 2008 and data are no longer acquired. The archival data require some level of additional processing to extract surface temperature. The ASTER TIR night time data are received as the AST\_09T surface radiance product, which has a saturation temperature of approximately 97°C (Urai et al., 1999). This product is atmospherically corrected using the Moderate Resolution Transmittance (MODTRAN) radiative transfer code, which accounts for



temperature, water vapor, elevation, ozone, and aerosols (NASA LP DAAC, 2001). The at-surface radiance data are finally separated into emissivity and pixel-integrated brightness temperature using the normalization emissivity approach within ENVI software (Realmuto, 1990; Gillespie, 1995). SWIR nighttime data are processed slightly differently using the assumption that any detected radiance is due solely to high temperature surfaces. Pixel integrated temperature is derived from band 4 (1.6-1.7  $\mu\text{m}$ ) using the Plank Equation and assuming an emissivity of 1. The detection threshold for this band ranges from 283-467°C (low gain) and 250-410°C (high gain).

If nighttime data are not available (usually due to cloud cover) close to the eruption time, daytime TIR and SWIR scenes are used. These scenes are initially processed using the same method as the nighttime data, but require removal of solar radiance. The average temperature difference between consecutive day-night pairs close to the acquisition date is found and removed from the daytime data. This method is used for pixels within the dome-collapse scar, which are the focus of this study.

#### *Dome collapse and deposit distribution analysis*

Eight BAF deposits from 2001 – 2013 are analyzed using the combination of the ASTER VNIR and TIR data. Using ASTER VNIR data, the runout lengths (straight-line horizontal length measured in satellite data) of the BAF deposits were manually measured in ESRI ArcMap. The material that is the source for the BAFs comes from different areas within the ~1550 x 3500 m dome, However, a unique starting point for each collapse is not generally known. Consequently, by using both the top and base of the collapse scar in the dome that resulted from each event, the resulting range in run-out distances represents the maxima and minima for each flow (Table 5). Throughout the text the maximum runout distance is given as the length measured from the top of the collapse scar to the distal end of the deposit. The locations of features along the deposits are

given in kilometers from the uppermost point, or headwall scarp, of the collapse scarp, and are therefore maximum lengths.

**Table 5. Summary of dome and block and ash flow deposit parameters for the eight collapse events.**

<b>Eruption Date</b>	<b>Collapse scar area (km<sup>2</sup>)</b>	<b>Collapse scar max. width x length (m)</b>	<b>Dome Rock Removed (km<sup>3</sup>)</b>	<b>BAF runout distance (km)</b>	<b>BAF runout from dome base (km)</b>	<b>H/L Ratio</b>	<b>BAF deposit area (km<sup>2</sup>)</b>
19-May-01	0.33	640 x 750		12.9-13.7	10.9	0.18	3.5
10-May-04	1.53	800 x 3500	0.004*	5.7-8.8	5.6	0.24-0.3	11.4
28-Feb-05	0.86	550 x 2400	0.11†	15.6-17.8	15.4	0.11-0.13	24.1
18/19-Dec-07	1.4	840 x 2650		10-12.7	9.8	0.20-0.21	5.1
25/26-Jun-09	0.46	580 x 1260		5.2-6.4	3.8	0.39-0.42	2.9
27-Oct-10	1.71	1100 x 2540	0.28**	16.4-19	15.7	0.12-0.16	22.3
26-Jul-13	0.24	330 x 1060		10.6-11.6	8.2	0.22-0.23	3.5
3 Dec 2013	0.4	550 x 1100		12.6-13.6	9.7	0.19-0.20	9.2

<b>Eruption Date</b>	<b>Max. deposit width (m)</b>	<b>Max. dome temp. (°C)</b>	<b>Dome pixels above TIR saturation (°C)</b>	<b>Flow direction</b>	<b>Lobes</b>	<b>Channelized deposit</b>	<b>Preceding thermal Anomaly</b>	<b>Evidence for surge?</b>
19-May-01	485	445	10	SW	N/A	Y	N/A	Y
10-May-04	2500	406	42	S	4	Minor	N/A	N
28-Feb-05	2490	312.86	8	SW, W	6	Minor	Y	Y
18/19-Dec-07	1370	273.5	10	SW	2	Y	Y	N
25/26-Jun-09	1560	N/A	10	S	4	N	Y	N
27-Oct-10	4100	N/A	N/A	S, SE	N/A	Y	Y	Y
26-Jul-13	1100	N/A	2	SW	3	Y	Y	N
3 Dec 2013	1550	N/A	3	SW	5	Y	Y	N

\* N. A. Zharinov and Yu. V. Demyanchuk 2007

† Shevchenko and Svirid, 2014

\*\* Dvigalo et al., 2011; Shevchenko et al., 2015

The runout length is also calculated from the dome base where the flows exit the erosional channels (Figure 2b) for a comparative length from a consistent location, and is given in Table 5.

The maximum temperature of the deposits and the area of the precursory thermal anomalies are

calculated using TIR, and SWIR data where available. The precursory thermal anomalies are interpreted by overlaying the contoured brightness temperature data on the VNIR images. Dome-collapse dimensions (e.g., planimetric area and length) are calculated using a combination of ASTER TIR and VNIR data.

## **2.3 RESULTS**

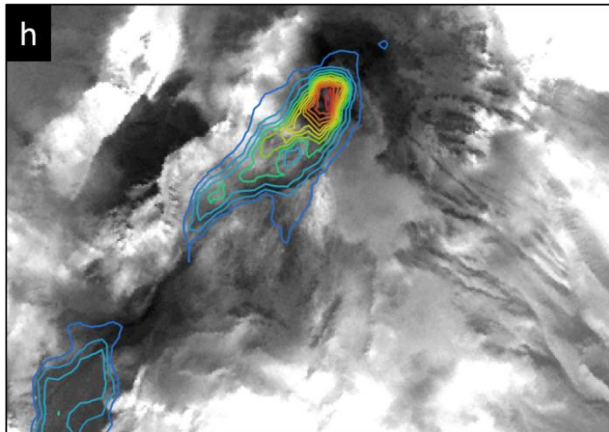
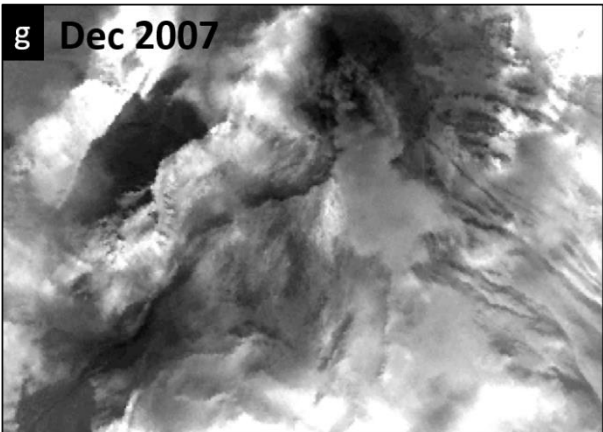
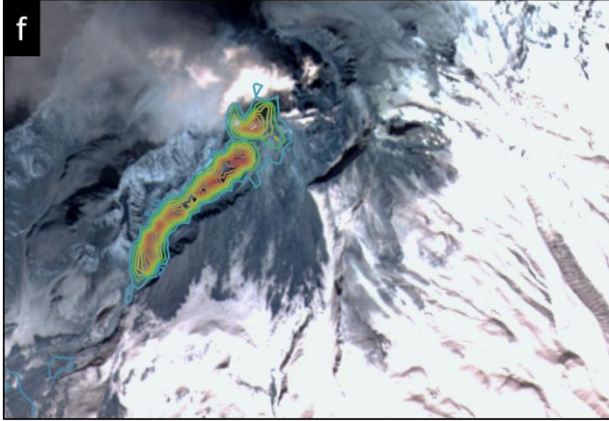
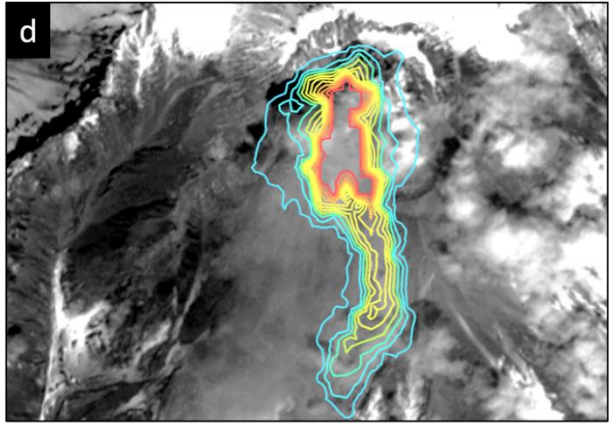
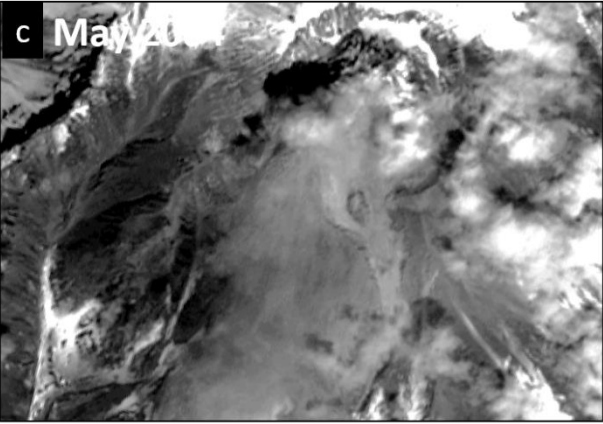
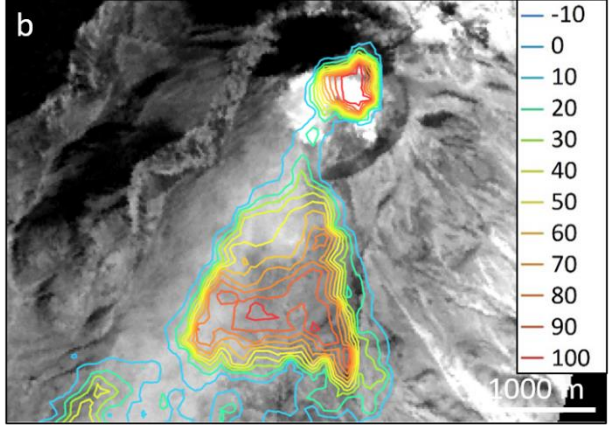
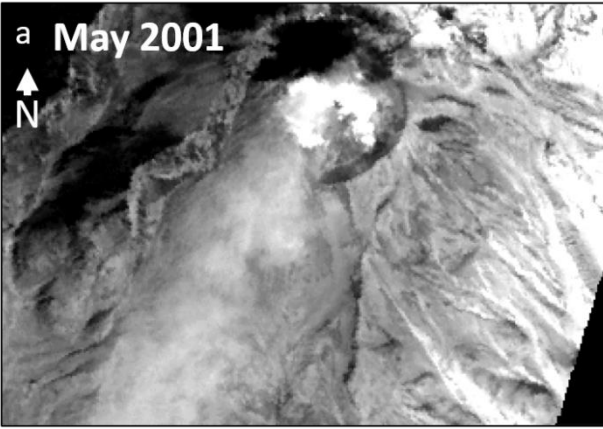
Careful examination of the ASTER VNIR and TIR data, combined with field validation, reveal details of the emplacement process for the eight collapse events that was not previously known. Below the current dome and talus apron are three large (1.5 km-wide) slide blocks which formed during the 1964 collapse (Belousov et al., 1999; Figure 2). These blocks direct the flows to the east or west depending on the initiation location on the dome.

### **2.3.1 19 May 2001**

This eruption produced a BAF originating from the northwestern side of the dome, forming a 0.33 km<sup>2</sup> collapse scar (Figure 5a-b) equant in shape with irregular edges. A maximum measured temperature within this scar of 445°C registered in a single 30 m<sup>2</sup> SWIR pixel in data acquired the same day as the eruption. This is the minimum temperature for this pixel, as it represents a mixed-temperature surface that could contain both hotter, and cooler areas. This is the hottest collapse scar temperature measured for all of the eight dome-collapse events, but temperatures likely exceeded this at the top of the collapse scar where a steam plume obscured the dome rock in the

SWIR image. The outer temperatures of the dome prior to collapse can fall below  $-10^{\circ}\text{C}$ , giving a pixel-integrated brightness temperature range of at least  $455^{\circ}\text{C}$  for the BAF source rock.

The BAF deposit (Figure 6a) is long and narrow ( $<485$  m), following the western edge of the 1964 debris avalanche deposit, with a total maximum length of 13.7 km (Table 5). The flow fanned out on the talus slope until it reached the upper slide block, where it was directed through drainage bounding the slide block's western margin. At 5.0 km from the scar the deposit bifurcates, with a smaller lobe extending south for another 1.9 km and then southeast around Baidarny Ridge (Figure 2). At the tip of Baidarny Ridge a second smaller lobe extends southwest for an additional 1.3 km. The main flow entered the Baidarnaya River channel 5.4 km from the scar where it traveled a further 8.2 km. The total deposit planimetric area is  $8.8$  km<sup>2</sup>. Lahar deposits extend beyond this point, resulting from emplacement of the BAF onto snow.





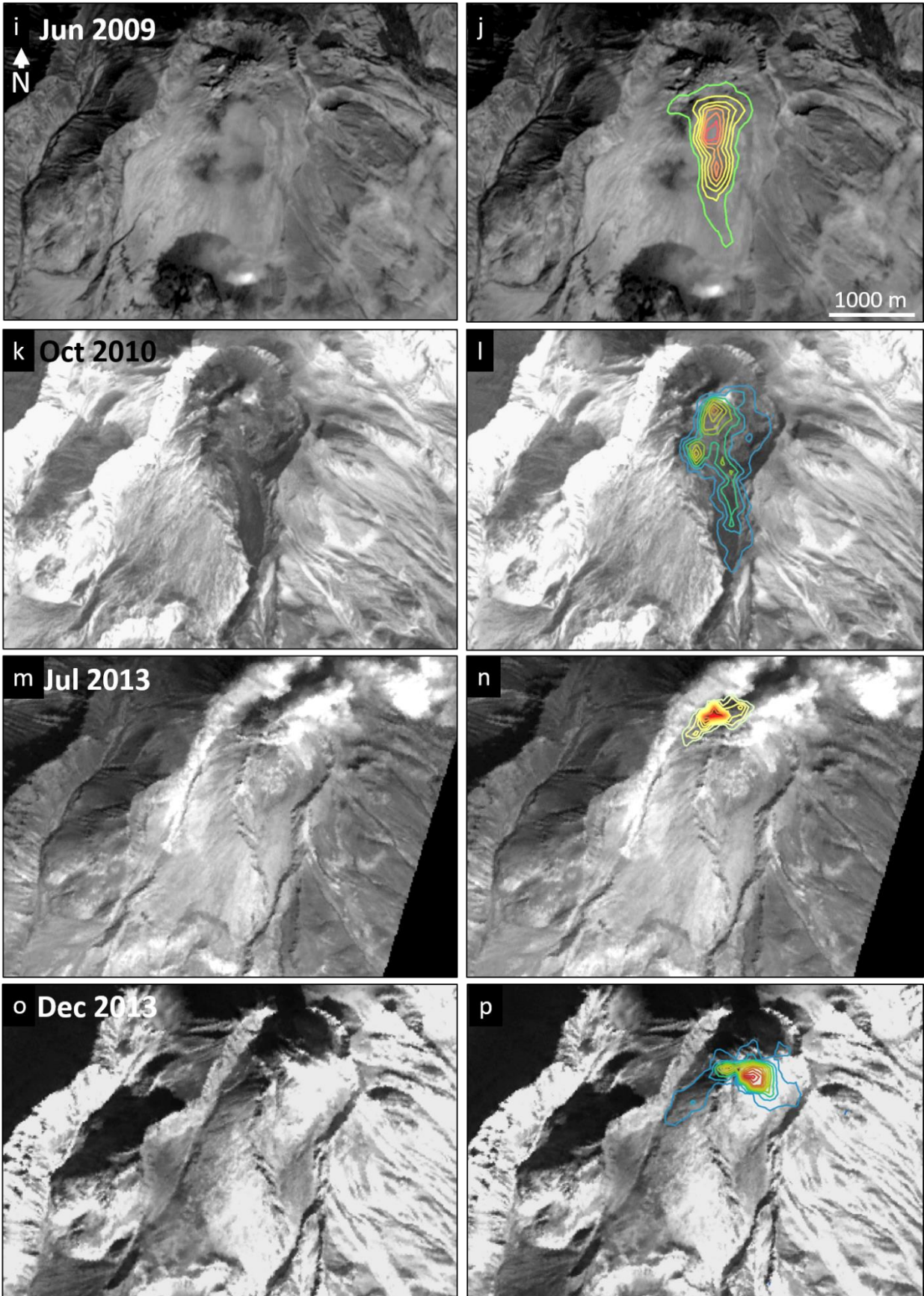


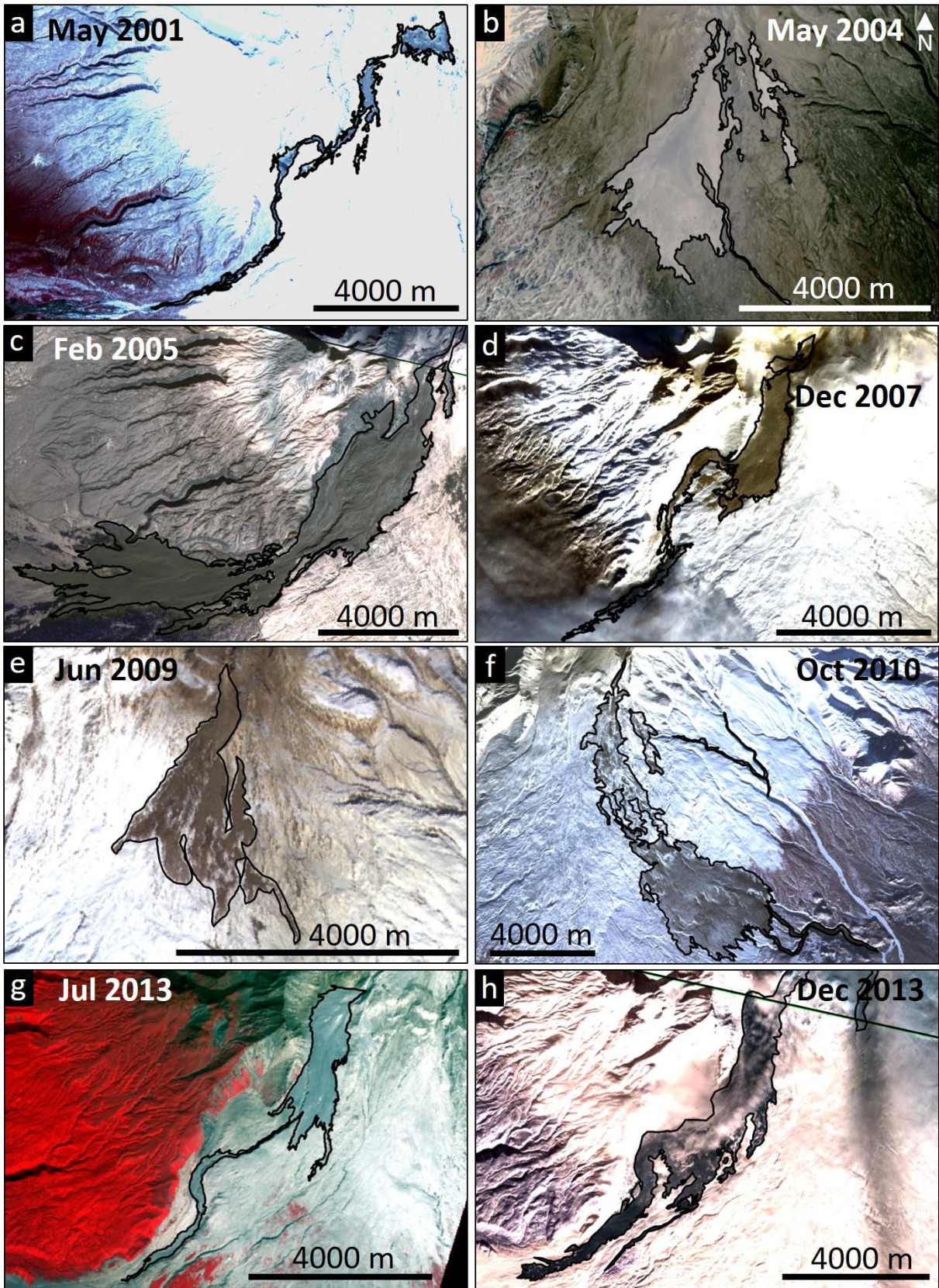
Figure 5. ASTER data of the eight collapse scars resulting from the dome-collapse events in the right column (VNIR image with the TIR-derived temperature contours of the dome-collapse scars overlain in the right column). The BAF event (month and year) are labeled in the left column. Acquisition dates and other information given in Table 6. Temperature contours are in 10-degree C increments as shown in (b) and all images are oriented with north to the top, as shown in (a).

Table 6. ASTER TIR and VNIR scenes used for dome collapse scar analyses.

Figure	Eruption date	TIR date		Days after eruption	VNIR date	Days after eruption
3a-b	19-May-01	19-May-01		0	14-Feb-02	271
3c-d	10-May-04	11-May-04		1	4-Jun-04	26
3e-f	27/28-Feb-05	12-Mar-05	*	4	12-Mar-05	13
3g-h	18/19-Dec-07	23-Dec-07		6	22-Dec-07	5
3i-j	25/26-Jun-09	30-Jul-09		36	29-Jul-09	35
3k-l	27-Oct-10	7-Dec-10	*	42	7-Dec-10	42
3m-n	26-Jul-13	23-Aug-13	*	28	23-Aug-13	28
3o-p	3-Dec-13	16-Feb-14		133	30-Jan-14	59

\* ASTER TIR day time image







**Figure 6. ASTER VNIR data of the eight block and ash flow deposits investigated in this study (all images are orientated north): a) 19 May 2001; b) 10 May 2004; c) 27-28 February 2005; d) 18-19 December 2007; e) 25-26 June 2009; f) 27 October 2010; g) 26 July 2013; h) 3 December 2013.**

### **2.3.2 10 May 2004**

Following the eruption, a portion of the southern flank of the Shiveluch dome-collapsed to produce a scar with an aerial extent of 1.53 km<sup>2</sup> (Figure 5c-d). In an ASTER TIR scene acquired one day later, 42 pixels (3.78 km<sup>2</sup>) within the collapse scar are above the ASTER TIR saturation temperature and the maximum detected SWIR temperature is 406°C. The eruption deposited hot material on the east and west slopes of the dome and talus slope. The majority of the material traveled to the east of the slide blocks and then continued south to produce a fan deposit with a maximum width of ~2.5 km and a total area of 11.4 km<sup>2</sup> (Figure 6b). The main body of the deposit terminates with four lobes, each up to 1 km in length. At 3 km from the dome base, a narrow section of deposit continues for 3 km southeast from the main deposit body. The maximum runout length is 8.8 km. To the west, a section of the flow traveled up and over the 1964 collapse crater rim and down a valley, emplacing another 3-km-long deposit over an area of 1.42 km<sup>2</sup>.

### **2.3.3 27-28 February 2005**

The SWIR data acquired on 23 February show three areas with elevated temperatures on the western side of the dome. The retrospective analysis of these data show that these areas largely coincide with the area of subsequent collapse. Data acquired five days after the eruption show an elongate scar that was cut out of the southeast portion of the dome by the collapse event. This scar has an area of 0.86 km<sup>2</sup> and maximum dimensions of 0.55 x 2.4 km (Figure 5e-f). The uppermost

area of the collapse scar overlaps the thermal anomalies detected earlier. The scar has a central elongate trough up to 170-m-wide and 2.1 km long, with lateral terraces ~160 m wide and ~1.2-km-long along the eastern side. A smaller western terrace up to 65-m-wide by ~0.6-km-long is also present. Within the trough is a 1.6-km-long,  $\leq 160$  m-wide zone. TIR data acquired on 12 March show eight pixels (an area of 720 m<sup>2</sup>) within the scar that remained above the saturation temperature of 97°C; whereas, the ASTER SWIR data acquired 29 March have pixels within the scar area that have a maximum temperature of 312°C.

The 27-28 February 2005 BAF traveled through the western drainage system and continued to the south and southwest for a distance reaching 17.8 km from the dome scar (Figure 6c). A smaller flow overtopped the eastern side of the western drainage system and deposited a lobe that extends further south for 2 km. The entire BAF covers an area of 24.1 km<sup>2</sup>. It traveled to the southwest alongside the Baidarnaya River then fanned out and emplaced the material of the upper fan with a maximum width of ~2.5 km. At a distance of 10.3 km from the scar, the deposit is largely confined to the ~190 m wide Baidarnaya River channel for ~2 km towards the west, before fanning out to emplace the lower fan deposit (which has a maximum width of 2.04 km). At 10.8 km from the scar, a portion of the BAF overtopped the channel and continued towards the southwest for another 4.2 to 5 km. This smaller deposit section has a maximum width of 900 m, and an area of 1.9 km<sup>2</sup>. The lower fan deposit terminates with five lobes up to 2 km long. The main 2005 deposit fan is surrounded by a rim of dead trees up to 300 m-wide that were killed by a fine-grained pyroclastic surge that continued past the BAF deposition area.

#### **2.3.4 18-19 December 2007**

The 18-19 December 2007 collapse occurred on the western side of the dome and talus slope (Figure 5g-h). Prior to the collapse, a thermal anomaly was visible near the summit of the dome in the area that would become the upper area of the collapse scar. The VNIR and TIR data show a collapse scar with an area of 1.4 km<sup>2</sup>. The maximum temperatures on the failed dome surface exceed the saturation temperature for the TIR over ten pixels (900 m<sup>2</sup>). The maximum SWIR-derived temperature is 273.5°C within the collapse scar.

The BAF was directed to the east of the 1964 slide blocks where it fanned out to form a deposit 4.5 km in length with a maximum width of 1.37 km (Figure 6d). At the end of the Baidarny Ridge, 6.5 km from the scar, the BAF turned towards the west and then to the south, and continued along the edge of the 1964 debris avalanche fan. The flow was briefly confined within the channel for 7 km, and ultimately formed a 5.1 km<sup>2</sup> deposit, with a maximum runout distance of 12.7 km. The VNIR data show that prior to the collapse and BAF emplacement, the top of the scar had largely been filled by a 670 x 900 m dome and associated talus.

#### **2.3.5 25-26 June 2009**

The BAF deposit emplaced during the 25-26 June 2009 eruption is the smallest included in this study. In my retrospective examination of TIR data, which was acquired on 27 May 2009, I detected an elongate thermal anomaly that measures ~0.45 x 1.33 km on the upper southern dome slope. The dome-collapse occurred in the southeast portion of the dome area of collapse coincided almost exactly with the location of the pre-existing thermal anomaly, producing a scar with an area

of 0.46 km<sup>2</sup> (Figure i-j). Four days after the eruption, ten pixels (900 m<sup>2</sup>) exceed the ASTER TIR saturation temperature of 97°C.

Deposition began after the BAF exited the eastern drainage system and emplaced material to the south over an area of 2.9 km<sup>2</sup> (Figure 6e). The runout length is a maximum of 6.4 km from the dome scar and it has a maximum width of 1.56 km. The deposit terminates in four lobes. The eastern-most lobe flowed up and over a topographic high at a bend in the drainage, located 4.4 km from the scar, while the other three lobes extend from the deposit fan.

### **2.3.6 27 October 2010**

In my retrospective analysis of TIR data acquired on 11 October 2010, 16 days before the 27 October eruption, I identified a 640 x 645 m thermal anomaly near the summit of the dome. The eruption produced a 1.1 x 2.54 km scar along the eastern side of the dome and talus slope, with an area of 1.71 km<sup>2</sup> (Figure 5k-l). The thermal anomaly I identified was located near the center of this scar area. The maximum depth of the scar was ~180 m, calculated from a photogrammetry-derived DEM in Shevchenko et al. (2015).

The 27 October 2010 eruption produced a BAF deposit that covered a total area of 22.3 km<sup>2</sup> (Figure 6f). The deposit includes: an area of relatively thin and patchy deposition in the proximal area down to ~10.6 km from the scar; the main deposit fan that extends from ~10.6 to ~16.2 km from the scar; a channelized deposit that followed the Kabeku river for an additional 5.4 km to the east; and two lobes that were emplaced over the eastern side of the 1964 collapse crater to distances of 4 and 7.5 km. The total length of the deposit including the channelized section reaches a maximum of 19.0 km from the collapse scar. The main deposit body covers an area of 16.2 km<sup>2</sup>, with 11.6 km<sup>2</sup> emplaced on top of the 1964 debris avalanche deposit. The deposit has a

maximum width of 4.1 km. The distal edge of the main deposit fan is defined by the continuation of the flow for an additional 0.4 to 1 km into linear furrows or depressions in the underlying 1964 debris avalanche deposit. There is evidence of a dilute surge cloud component from the October 2010 BAF in the Kabeku River channel, as shown by the trees killed on the hillsides surrounding the channel.

### **2.3.7 26 July 2013**

The 26 July 2013 dome-collapse event occurred on the northwest flank of the dome, producing the smallest collapse scar observed in this study with an area of only 0.24 km<sup>2</sup> (Figure 5m-n). In imagery prior to the eruption, steam can be seen to emanate from the collapse area and elevated temperatures surround the future collapse area, although other areas of the dome are also elevated in temperature. In the collapse scar, two pixels (180 m<sup>2</sup>) exceed the TIR saturation threshold in data that was acquired on 23 August 2013, with the hottest area located just to the south of the future scar center.

The BAF that resulted from this collapse traveled down the western side of the dome and through the western drainage system, and emplaced material to the southwest of the dome alongside the Baidarny Ridge and then down the Baidarnarya River channel (Figure 6g). The portion of the flow that emplaced the main deposit body fanned out below the dome and terminated in three distal lobes. The distal portion of the BAF continued as a channelized flow along the Baidarnarya River channel and in places shows evidence of superelevation (flowing up and over a topographic high) and overtopping the confining channel walls. It is uncertain whether this deposit was entirely emplaced during the 26 July eruption, or if it also includes material produced by subsequent activity in August (KVERT online report, 31-2013), because cloud cover prevented

imaging during the weeks following the eruption. The main deposit body has a total length of 3 to 4.3 km, and a maximum width of 1.1 km. The channelized portion of the BAF entered the Baidarnaya River channel 6.3 km from the scar and continued for an additional 4.65 km downstream. The flow then overtopped both channel walls at 7.9 km from the dome after a bend in the channel, and again at 9.9 km where the channel shallows. The maximum total length of the deposit 11.6 km from the scar, and it covers an area of 3.5 km<sup>2</sup>.

### **2.3.8 03 December 2013**

The 3 December 2013 BAF is the result of a dome-collapse event originating from the northeast section of the dome (Figure 5o-p) in the same location as the 19 May 2001 and 26 July 2013 events. TIR data acquired on 16 February 2014 show that there was an elevated thermal signature on the dome within a pre-existing collapse scar approximately 0.4 km<sup>2</sup> in size, with maximum dimensions of ~1.1 x ~0.55 km. Three pixels (270 m<sup>2</sup>) exceed the saturation threshold of 97°C.

The BAF emplaced mainly to the western side of the 1964 slide blocks, with a small portion of the flow traveling to the eastern side of the dome, which produced a 3.4-km-long TIR signature in the post-collapse image. A narrow thermal signature on the western edge of the talus slope extends 3 km in the image before widening below the dome and depositing the bulk of the material over another 5.3 km to 8.6 km from the scar, after which a narrow portion of the flow continued down the Baidarnaya River channel to the maximum runout distance of 13.6 km (Figure 6h). A portion of the flow emplaced an additional long and narrow deposit for 2.3 km from the southeast edge of the main deposit body, to 11.6 km from the scar. The deposit has a maximum width of 1.5 km.

Webcam images (taken from the Kamchatkan Volcanological Station in Klyuchi village, 45 km to the SSW of the dome and 30 km from the deposit fan) at one-minute intervals show five smaller avalanches in the two hours preceding the emplacement of the largest deposit. Over the three hours of the eruption event during daylight hours (13:13 to 16:07, local time) there were at least six pulses of collapse, with only three of those at 13:21, 13:42, and 14:14 appearing to transport material to the distal extent of the deposit. The initial flows did not extend beyond the end of Baidarny Ridge (6.6 km from the scar). Figure 3 shows one of the BAF pulses moving alongside Baidarny Ridge. Smaller avalanches or flows continued into the night.

## 2.4 DISCUSSION

Extended periods of dome activity have occurred at Soufrière Hills volcano on Montserrat from 1995 to 2010 (e.g. Wadge et al., 2014), Unzen volcano in Japan in 1990 to 1995 (e.g. Tadahide et al., 1999, Miyabuchi, 1999), and Sinabung volcano, Indonesia (December 2013 to present; Gunawan, et al., 2017; Pallister et al., 2017). Similar activity is ongoing at Shiveluch volcano and the dome-collapse events and their resulting BAF deposits are detailed to evaluate relationships between dome growth and dome-collapse distribution. The analysis of these data clarify the impact of large BAFs over the duration of an eruption and document the variability of dome-collapse and related BAFs sizes over the course of a long-lived dome-forming eruption. Identification of systematic patterns in the distribution and size of BAF emplacement over durations of eruptions could reduce uncertainty in evaluating risk at other dome-building volcanoes around the world (Ogburn et al., 2015). In order for such patterns to be useful in hazard

evaluations they must be statistically robust, requiring many such studies of dome forming eruptions.

*Dome-collapse BAF deposits on Shiveluch*

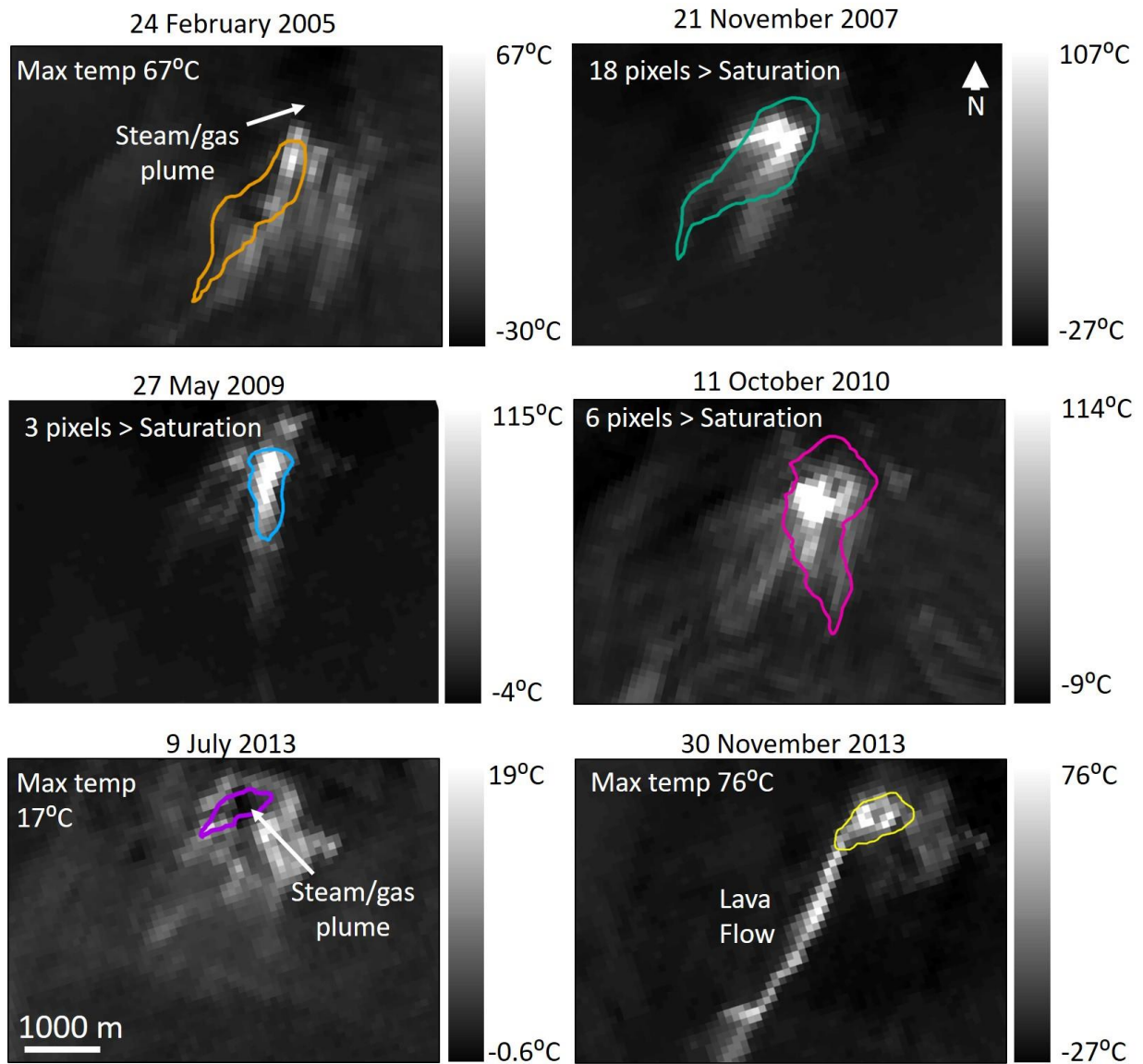
The recent deposits on Shiveluch are predominantly of the BAF type. The 2005 and 2010 deposits were confirmed to be BAF deposits during a field campaign in 2015 (Chapter two), however, due to the poor accessibility on the remote and dangerous volcano and time since emplacement, other deposits were not examined in the field. A study carried out by Shevchenko and Svirid (2014) concluded that events in May 2004, December 2007, and October 2010 were gravitational in nature based on morphological investigation of the dome scars. They identified collapse scarps, strongly tapering-downward scars, lack of an explosion craters, and an absence of ballistic trajectories. Based on these observations, I assume that all BAF deposits studied here are largely due to dome-collapse rather than column collapse. The last confirmed pyroclastic flow generated by column collapse was in 1964 during the eruption that produced a Plinian column, with no dome present (Belousov, 1995). Shevchenko and Svirid (2014) explored the morphological evidence on the dome for a collapse origin of May 2004, December 2007, and October 2010, and concluded that these were due to gravitational processes rather than explosive eruptions, even though some events were accompanied by explosive activity. Here, remote sensing data confirm this analysis. Evidence of ash plumes and deposition associated with the collapse events are seen in several satellite images. Lightning strikes associated with these ash plumes are also recorded by the World Wide Lightning Location Network (WWLN) during the February 2005, June 2009, and October 2010 events (over 11 minutes, 17 hours, and 1.5 hours, respectively). The pumiceous component of the May 2001 and July 2013 deposits suggest that



partial collapse of dome material in some cases exposed deep or fresh parts of the dome which may have undergone vesiculation due to gravitational unloading.

#### *Pre-eruption thermal anomalies*

Examination of precursory thermal anomalies over the eight eruptions allows assessment of their value in improving forecasts of the size of collapse. Prior to six of the eight events thermal anomalies in the TIR pixel-integrated brightness temperature data occurred within, or partially overlap, the area of future dome-collapse (Figure 7). The thermal anomalies occur within the area of the future collapse but are smaller in size, except for the thermal anomaly preceding the June 2009 event that almost exactly marks the size and area of the future collapse. Increased thermal output on a lava dome can be the result of the heat radiating outward from cracks that form as lava moves towards the surface, lava extrusion onto the surface, active faults that reach surface, increased fumarole temperatures, and the exposure of inner, hotter material by collapse or explosions (e.g., Kaneko et al., 2002; Schneider et al., 2008; van Manen et al., 2010; Bernstein et al., 2013; Wessels et al., 2013). Gravitational sliding processes that result in fault movement and headwall fractures have previously been described at Shiveluch (Shevchenko and Svirid, 2014). The formation of headwall scarps may account for the thermal anomalies preceding the collapse events, especially the events where the anomaly occurs at the top of the subsequent collapse.



**Figure 7.** ASTER TIR scenes preceding six of the eruptions included in this study with the dome-collapse scar boundaries that followed them overlain in color. The maximum temperature or the number of pixels that exceed the ASTER TIR saturation temperature of 97°C. The 9 July 2013 scene has the weakest thermal anomaly, and a steam/gas plume covers the top of the area.

Here, I discuss the limitations of using these data for thermal precursory analysis. These pre-eruption thermal data are based on a single data point (one ASTER TIR scene) for each eruption since data are limited to only a few data acquisition times during the days to weeks preceding and following collapses. Cloud cover and gas and steam plumes over the dome area further reduces this data availability. A greater density of data and a closer linkage to other monitoring data is recommended for a better understanding of thermal precursory signatures. Because the depth of instability, and therefore, collapse, cannot be determined in advance of an eruption, it would be difficult to forecast deposit size based on the surficial manifestations of dome activity, such as areas of elevated thermal activity. An additional problem with long-lived dome-forming eruptions is the occurrence of thermal anomalies on the dome surface that do not lead to collapse events. The KVERT online reports commonly note persistent thermal anomalies over the area of the lava dome at Shiveluch. Between the dates 19 May 2001 to 6 December 2013 there were 287 ASTER TIR scenes showing elevated temperatures on the dome. This includes scenes only partly covering the dome, and scenes containing thin cloud or gas/steam through which the thermal anomaly is visible. Satellite observations are thus limited by the repeat time and scenes free of atmospheric cloud and gas/steam plumes obscuring the dome area. For a complete evaluation of the value of thermal imaging for identifying areas susceptible to collapse, a higher density of data is needed, either satellite- or ground-based, leading up to an eruption. In retrospect, this could allow the identification of the duration and any increase in thermal output in the pre-collapse area to be quantified. To improve the understanding and applicability of the link between thermal anomalies to active lava extrusion, the integration of additional monitoring datasets, such as seismicity, gas flux measurements, and deformation data, is recommended. Therefore,

quantifying the relative roles of active dome-growth processes, as opposed to other external factors, is important to forecasting.

#### *BAF deposit distributions*

BAF maximum runout distances vary from 6.4 to 19.0 km, producing deposits that range in area from 3.5 to 24.1 km<sup>2</sup>. Additional surge deposits occur in the May 2001, February 2005, and October 2010 deposits at Shiveluch, extending up to 300 m beyond the main deposit boundaries. The larger values are impressive in comparison to collapse events and deposits at other volcanoes around the world (Table 7). The 2005 and 2010 BAF deposits are the two largest in both runout distance and deposit area. Prior to 2015, the largest published historical dome-collapse volume was the 12-13 July 2003 failure at Soufrière Hills volcano, with a volume of 0.21 km<sup>3</sup> (Herd et al., 2005). The October 2010 collapse exceeds this with a volume of 0.28 km<sup>3</sup> prior to bulking (increasing in size) by entraining accidental material during flow transportation, calculated by Dvigalo et al., 2011 (Shevchenko et al., 2015).

**Table 7. Block and ash flow maximum runout distance and maximum deposit area for Shiveluch and other dome-producing volcanoes around the world.**

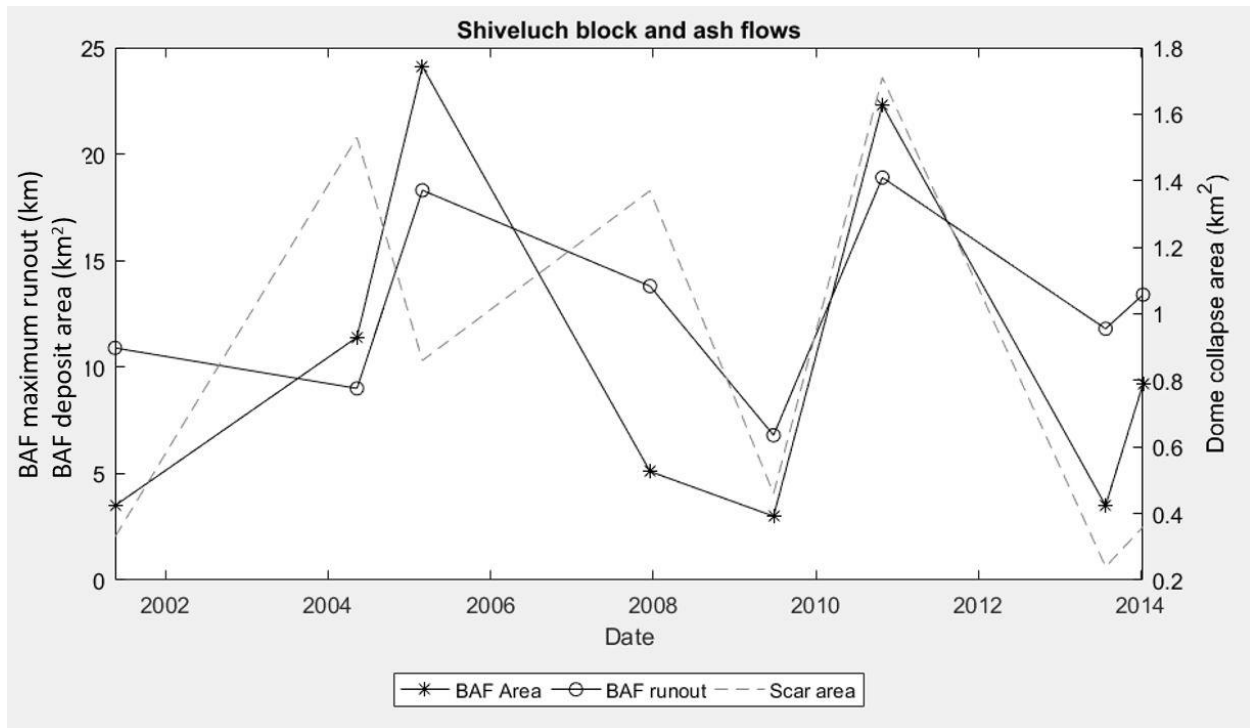
Volcano	Eruption Date	Max. BAF runout distance (km)	Max. Deposit Area (km <sup>2</sup> )	Reference
Shiveluch	19-May-2001	13.7	3.5	
	10-May-2004	8.8	11.4	
	28-Feb-2005	17.8	24.1	
	18/19-Dec-07	12.7	5.1	
	25/26-Jun-09	6.4	2.9	
	27-Oct-2010	19	22.3	
	26-Jul-2013	11.6	3.5	
	3-Dec-2013	1	9.2	
Merapi	18/19-Dec-30	13.2	8.5	Bourdier and Abdurachman, 2001; Ogburn, 2012.
	7/8-Jan-69	13	7.8	Bourdier and Abdurachman, 2001; Ogburn, 2012.
	14-Jun-2006	7.8	1.136	Thouret et al., 2010; Thouret et al., 2015
	5-Nov-2010	15.5	6.53	Surono et al., 2012, Charbonnier et al., 2013b; Solikhin et al., 2015
Unzen	1990-1995	5.5		Miyabuchi, 1999
Tarawera	1305 AD	9.4		Nairn et al., 2001; Hanenkamp, 2011
Chaiten	19-Feb-2009	6		Major et al., 2013
Soufriere Hills	1995-2010	7	10	Cole et al., 2002; Sparks et al., 2002
Sinabung**	2010-2015	4.9		Yulianto et al., 2016
Augustine**	Jan-Mar 2006	5	4.42*	Vallance et al., 2000
Colima	19-Jan-1913	15	0.07	Saucedo et al., 2005

\* Area includes all deposit components (block and ash flow plus surge).

Data for other volcanoes sourced from Ogburn (2012) and Hartnet et al., (2017).

\*\* Flows entered the sea, therefore, runout distances are minimum values.

Although the results of this study show a relationship between deposit size/runout distance and the dome-collapse scar areas from 2001-2009, a much stronger relationship emerges after 2009 (Figure 8). The lack of a simple relationship between size of the collapse scars and the size of the resulting BAFs in our data suggest that additional controlling factors are involved, such as the depth of instability (in addition to the area affected) of the dome rock that controls the BAF deposit size, and runout distance is affected by the transportation path geometry (channelized or open area) that the flow takes. This is reflected in the H/L values from 0.13 to 0.27, a parameter that has been used to compare the mobility of granular flows (e.g., Hayashi and Self, 1992). The May 2004 and December 2007 collapses produced relatively large collapse scars on the dome, which could be due to a shallow collapse depth over a broad area. The February 2005 collapse produced a deep collapse scar on the dome, resulting in a relatively small scar area. The depths of dome-collapse scars on Shiveluch should be quantified and compared to deposit size for further analysis. Channelization enhanced the runout distance of the May 2001, December 2007, October 2010, July 2013, and December 2013 flows where the flows continued for over 5 km beyond the main fan deposit, with the length of the channelized deposit accounting for up to 60% of the total deposit length. These deposits that have significant channelized sections have a poor relationship between collapse area and runout distances. Channelization of a BAF that occurred on 5 November 2010 at Merapi volcano also enhanced the runout distance, from 8.4 km (non-confined) to 15.5 km down the Gendol River channel (Komorowski et al., 2013).



**Figure 8. The block-and-ash flow (BAF) area (km<sup>2</sup>), runout distance (km), and planimetric dome collapse areas (scar area, km<sup>2</sup>) of the eight collapse events.**

### *Dome height and large collapse events*

The largest collapse events, in 2005 and 2010, correspond with a maximum relative dome height (Figure 4). The dome height 10 days before the 27 February 2005 eruption was 517 m, and the dome height prior to the 27 October 2010 eruption was 563 m (Zharinov and Demyanchuk, 2013). These maximum heights remained stable for over a year before the large collapse events. Based on a photograph of the dome taken on 21 October 2016, the current dome height is ~610 m, the largest to date (Figure 9). The increase in height has occurred in the area of the 27 October 2010 eruption collapse scar, which has been filled with new dome material. The continued analysis of dome height and eruption data over time will show whether this is a continuing trend for the Shiveluch dome-growth and collapse cycle.



**Figure 9.** Photo of the Shiveluch dome taken from the southwest on 21 October 2016 (solid black line denotes the dome surface in this view). The dashed black line depicts the dome surface four days prior (17 October 2010). Following the eruption on 27 October 2010, the dome surface changed dramatically, shown by the white line (after Zharinov and Demyanchuk, 2013). Photo courtesy of Yuri Demyanchuk.

## 2.5 CONCLUSIONS

Shiveluch has produced eight large BAFs between 2001-2013, including the largest dome-collapse volume and the two largest BAF deposit sizes (in terms of runout and deposit area) in recorded history. Using ASTER data, this study 1) investigated the relationships between the dome-collapse events and the deposits that they produced, 2) described the distribution and long



runout of these large BAF deposits, and 3) investigated the relationships between areas of elevated thermal output leading to the collapse events, and the ensuing collapse scars. Here, I described BAF deposits with areas that range from 3 km<sup>2</sup> to 24 km<sup>2</sup>, and have maximum runout distances of 6.4 to 19 km. There is direct evidence of a detached surge component for the May 2001, February 2005, and October 2010 BAFs, shown by the destruction of vegetation and the emplacement of fine-grained material surrounding the deposits. Precursory elevated thermal anomalies occur in six out of eight events with some correlation between size and collapse area, especially with the 2009 failure. However, thermal precursors cannot currently be used to predict dome-collapse events as thermal anomalies occur on the dome regularly that are not followed by dome failure.

## **2.6 ACKNOWLEDGEMENTS**

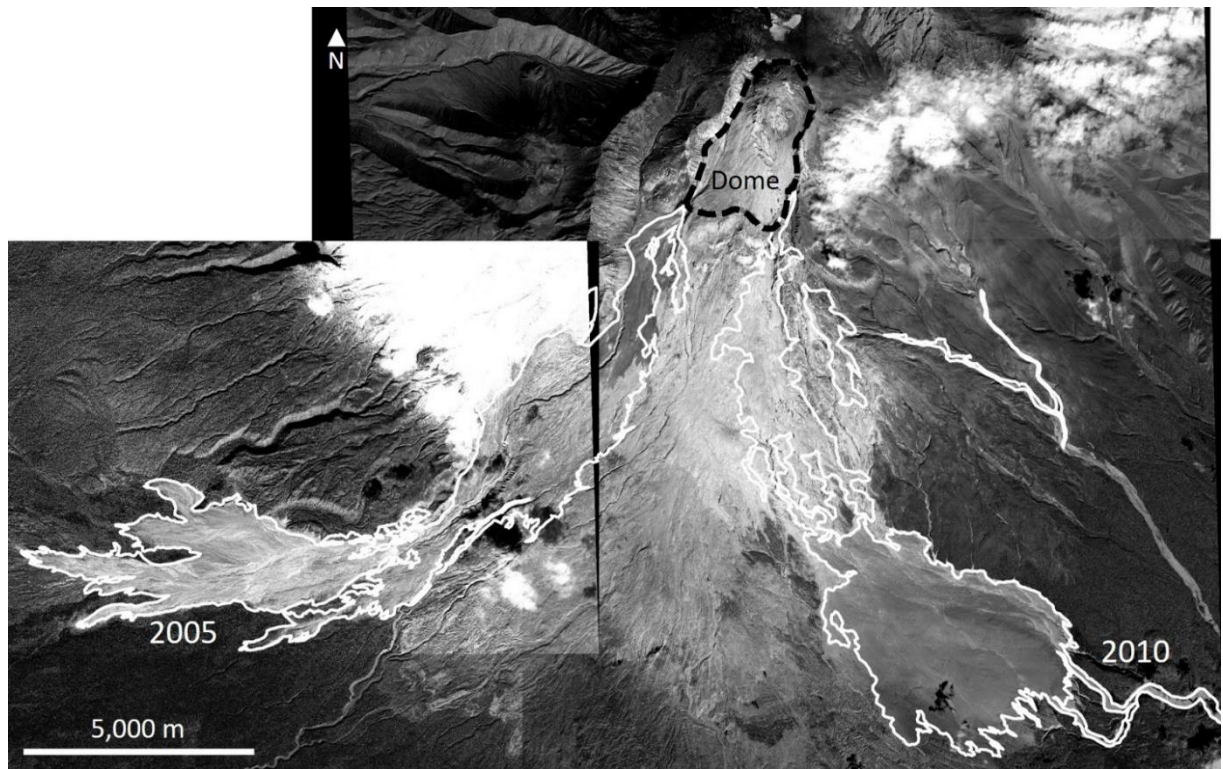
Funding for Janine Krippner was provided by the NASA, Earth and Space Science Fellowship program (NNX14AK88H) for the years 2014-17 and the NASA; and for Mike Ramsey by the NASA, Science of Terra and Aqua Program (NNX14AQ96G). The high-resolution QuickBird-02 and WorldView-02 data were provided by a DigitalGlobe Foundation Imagery Grant. The authors wish to thank the World Wide Lightning Location Network (<http://wwlln.net>), a collaboration among over 50 universities and institutions, for providing the lightning location data used in this paper. Thank you to Alison Graettinger for comments and discussions.

### **3.0 THE 2005 AND 2010 BLOCK-AND-ASH FLOW DEPOSITS ON SHIVELUCH VOLCANO, KAMCHATKA**

#### **3.1 INTRODUCTION**

Shiveluch, the northernmost and one of the most active volcanoes in Kamchatka, Russia, has produced some of the largest dome collapse-derived block-and-ash (BAF) deposits in historical times. The current eruptive episode began in 2001 and has included the gravitational failure of dome rock, which results in a wide range in deposit types, from small rockfalls that do not extend beyond the dome, to major dome failure events with collapse volumes reaching 0.28 km<sup>3</sup> (Dvigalo et al., 2011; Shevchenko and Svirid, 2014). Eight large block-and-ash flows occurred on 19 May 2001, 10 May 2004, 27-28 February 2005, 18-19 December 2007, 25-26 June 2009, 28 October 2010, 26 July 2013, and 3 December 2013, and are described in Chapter one. The two largest deposits were emplaced during the February 2005 and October 2010 events (Figure 10) investigated by remote sensing methods using orbital Advanced Spaceborne Thermal Emission and Reflection Radiometer (ASTER) Visible-Near Infrared (VNIR), and high-resolution WorldView-02 and QuickBird-02 sensor datasets. Here, we present a detailed analysis of the surface morphology and stratigraphy of the deposits, and utilize the resulting data to understand the processes responsible for the distribution of these extreme large end-members of dome-collapse related pyroclastic density currents. In addition to this, the LAHARZ model is used to assess the applicability of the inundation simulation model to these large BAF flows. The results

are compared to the distributions of the 2005 and 2010 deposits to check the simulated results to the physical deposits that were produced.



**Figure 10. The Shiveluch 2005 and 2010 block and ash flow deposits originating from partial dome collapse. Left image is a WorldView-02 scene (panchromatic band) acquired on 29 September 2010. Right image is a QuickBird-02 scene (panchromatic band) acquired on 27 August 2013.**

Experiments and numerical simulations of granular flows are increasingly used in combination with geological information to understand the runout extent and distribution of hazards associated with volcanic eruptions (e.g. Charbonnier and Gertisser, 2009; Oramas-Dorta et al., 2012). Data for large end-member BAFs that include inundation areas and runout distances are limited, yet they are valuable for hazard assessment (Widiwijayanti et al., 2009). Prior to the 2011 published  $0.28 \text{ km}^3$  volume for the Shiveluch 2010 dome collapse (Dvigalo et al., 2011), the largest published BAF known was from Soufriere Hills volcano, Montserrat. However, the distal

part of this flow was emplaced offshore (Cole et al., 1998; Calder et al., 2002; Cole et al., 2002), consequently, the full extent is unknown. This 2003 Soufriere Hills flow was produced a dome collapse and has an on-land volume of  $0.21 \text{ km}^3$ . It was emplaced over an 18-hour eruption (Herd et al., 2005). In contrast, the October 2010 Shiveluch collapse event has a volume of  $0.28 \text{ km}^3$  (Dvigalo et al., 2011; Shevchenko et al., 2015). The Shiveluch 2005 collapse volume ( $0.11 \text{ km}^3$ ) was less than half of the 2010 event (Shevchenko and Svirid, 2014). These are minimum deposit volumes as they do not take into account bulking (increases in volume) due to entrainment of accidental material from pre-existing deposits. We note that bulking is observed in entrainment of lower density andesite clasts in deposits of the 1964 eruption and erosional channels closer to the dome, and consequently, we cannot rule out some degree of bulking in the 2010 and 2005 flows.

BAFs are a result of the partial collapse of a lava dome and can be triggered by volcanic and non-volcanic processes such as eruptions, earthquakes, or rainfall, which can make them difficult to forecast (Carn et al., 2004). However, with the advent of near-real-time satellite and ground based observations of features that reflect dome stability, it is now possible to issue probabilistic forecasts of dome-collapse and related pyroclastic flows (Wright et al., 2017).

The hornblende-plagioclase andesite Shiveluch lava dome (Gorbach et al., 2016) has temperatures that range over of hundreds of degrees, from a cooler outer carapace to the hotter interior (Chapter one). The inner and hotter dome material likely degassed to a lesser extent, resulting in pore-pressure-induced autobrecciation, in addition to the mechanical breakage from clast interactions during transportation. The role of explosive and mechanical-based fragmentation has been discussed in work by Dellino and La Volpe (1995), Bursik et al. (2005), and Mackaman-Lofland et al. (2014). These workers document a range of transitional facies between debris avalanches and vesicular pyroclastic flows with BAFs somewhere in between. Perhaps, the mix of

gravitational failure with hot, explosive fragmentation leads to BAF deposits that share some similarities with both debris avalanches and column-collapse pyroclastic flows? In this chapter, I discuss the morphology of flow surfaces, deposit stratigraphy, fan and channelized characteristics, and the distribution of large dome blocks carried by the flows.

### 3.2 METHODOLOGY

The 2005 and 2010 BAF deposits were examined in detail using panchromatic high resolution data (Table 8). The deposit surfaces were characterized based on surface morphology, roughness, and block content using the Esri ArcMap program. Areas of interest were identified and investigated further in the field, along with stratigraphic profiles where available. Aerial images were collected using a drone by A. Belousov and M. Belousova in the summer of 2016. Componentry samples were also collected and analyzed by A. Belousov and M. Belousova.

**Table 8. Parameters for the high resolution data sets used in this chapter.**

<b>Satellite sensor</b>	<b>Acquisition Date</b>	<b>Spectral Range (nm)</b>	<b>Spatial Resolution /swath width (at nadir)</b>	<b>Deposit imaged</b>
WorldView-02	12-Mar-05	Panchromatic 450-800	0.46 m/16.4 km	Shiveluch 2005 BAF
QuickBird-02	27-Aug-13	Panchromatic 450-900	0.65 m/ 16.8 Km	Shiveluch 2010 BAF



### 3.3 RESULTS

The 2005 and 2010 deposits share similarities in surface morphology due to the similar eruption style, flow transportation processes, and depositional processes. I have assigned nine facies groups across the two deposits that share similar physical characteristics (Figure 11).

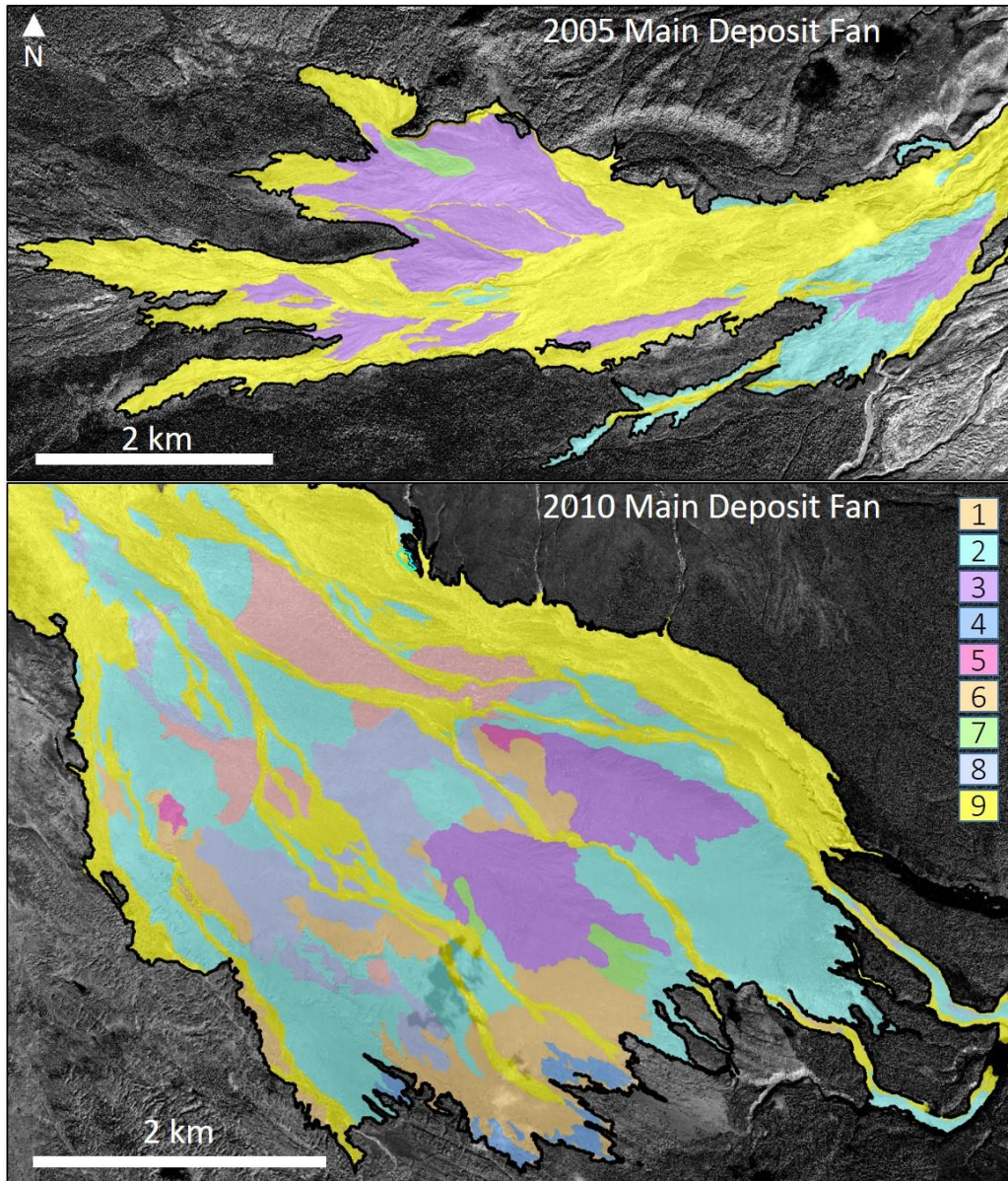


Figure 11. The nine facies that represent surface characteristics across the 2005 and 2010 main deposit fans and channelized deposits. The colors and numbers correlate to the descriptions on the next page.

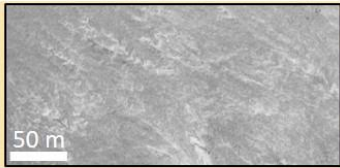
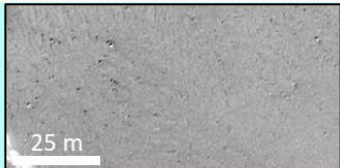
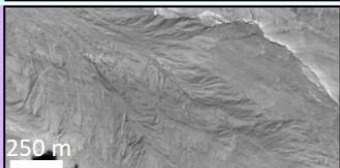
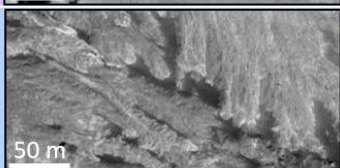
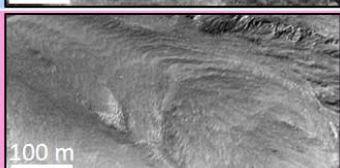
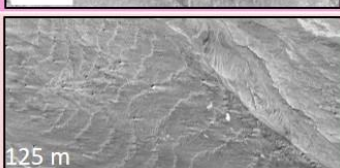
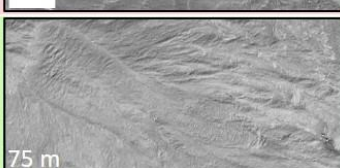


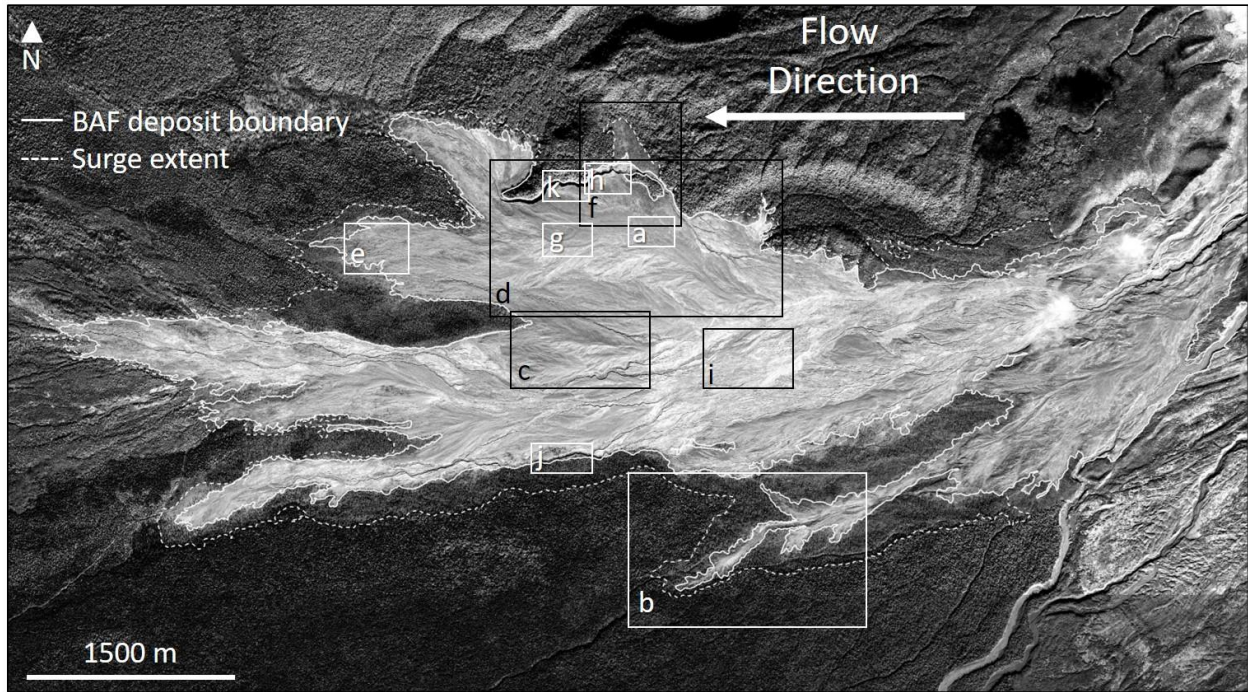
	Facies	Description	Example
1	Low-relief with rare to absent surface blocks	Contains rare large surface blocks and low surface relief with no features casting shadows onto the deposit surface. Faint lobe terminations in places.	
2	Low-relief with surface blocks	Surface blocks common. Low surface relief with no features casting shadows onto the deposit surface. Faint lobe terminations visible in places.	
3	Composite Lobes	Series of overlapping lobes with varying sizes, extents, and shapes. Levees and channels may be present. Lobes have ridge and furrow morphology. Surface blocks are variable.	
4	Feathery terminations	Occurring at the distal end of the main deposit fan. They are block-poor with low-relief, and contain bands of low-density entrained material around the boundaries.	
5	Herringbone	Sequence of repeating v-shaped features or ridges, with the vertexes pointing upstream.	
6	Parallel linear scarps	Repeating, near-parallel curvilinear scarps. Block contents are variable.	
7	Arcuate scarp	Singular or repeating scarps. Irregular remobilized deposit surfaces within and downstream of the scarp. Terminations are often lobate or rounded.	
8	Curvilinear bench and scarp facies	Multiple arcuate scarps, often joined or in subsequent steps. Areas below the scarps are irregular, and sometimes contain lobate features within the remobilized material.	
9	Surface erosion	Fluvial erosion has occurred in sheets, or has formed meandering and braided channels. Surface block contents are variable, higher within channels.	

Figure 2. continued.

### **3.3.1 Shiveluch 2005 BAF deposit**

The 2005 BAF deposit is composed of fragmented dome material, and accidental lithic clasts that are seen on the surface. The locations of the following figures are given in Figure 12. The deposit comprises an ash and lapilli-supported matrix with sub-angular to sub-rounded blocks, in some cases exceeding 6 m in length. This surge deposit is well-sorted (Figure 13), normally-graded and is composed of lapilli to very fine ash with a maximum deposit thickness of 75 cm (sample locations are shown in Figure 14). The surge deposit also contains accretionary lapilli, charred and uncharred wood, dome-rock clasts up to 5 cm in diameter, and degassing pipes. The surface of the BAF deposit contains numerous curvilinear bands that are composed of lower-density andesite clasts from the underlying 1964 pyroclastic flow deposit, and wood fragments with various degrees of charring. These bands both bifurcate from, and merge towards, each other as well as remain nearly parallel to each other (Figure 15).





**Figure 12.** The Shiveluch 2005 BAF main deposit fan area (panchromatic WorldView-02 scene acquired on 29 September 2010). The white boxes and letters indicate areas where the photographs in the following section were taken. The black boxes and letters indicate the areas of the figures that are enlargements of this WorldView-02 scene. a) Figure 15; b) Figure 16b; c) Figure 17; d) Figure 18; e) Figure 19; f) Figure 20; g) Figure 21; h) Figure 22; i) Figure 23; j) Figure 24; k) Figure 25.


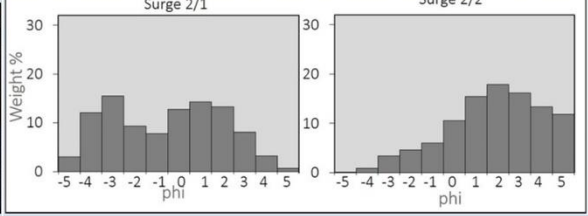

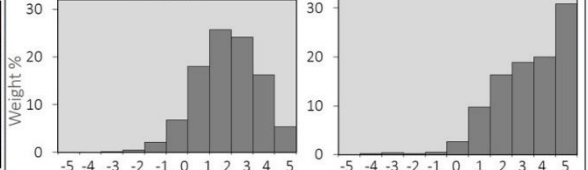

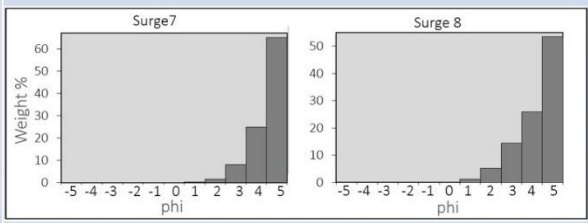

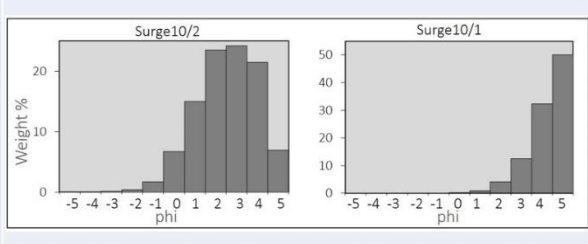

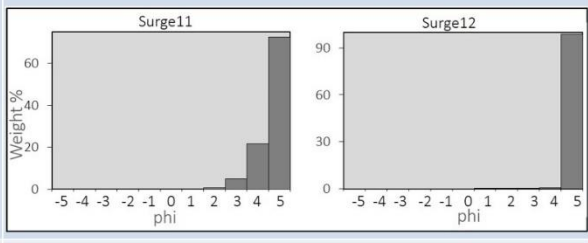
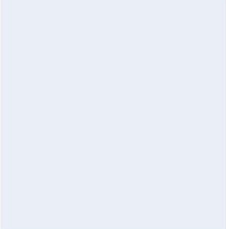
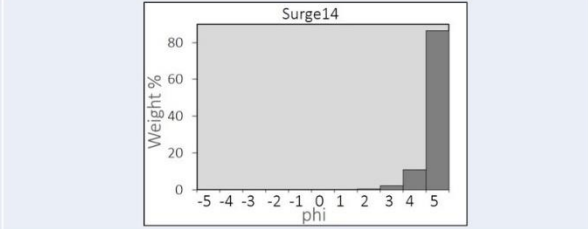
Photo of sampled section	Grain-size distributions with relative abundances (measured using the phi scale)	Sample descriptions
		<p><b>Surge 2/1</b> – normally graded medium-fine grained sand with clasts up to 5 cm, thickness of 25 cm.</p> <p><b>Surge 2/2</b> – A diffuse boundary above a fine-grained sand with degassing pipes and traces of accretionary lapilli, thickness of 20 cm.</p>
		<p><b>Surge 3/1</b> – medium to fine grained ash with few clasts in the lower section - vague degassing pipes. Rare clasts of pumice on the surface.</p> <p><b>Surge 3/2</b> - more fine grained ash with diffuse boundary, thickness of 8 cm.</p>
		<p>At the boundary of the living forest.</p> <p><b>Surge 7</b> – well-sorted fine grained ash with a thickness of 6.5 cm.</p> <p><b>Surge 8</b> well-sorted fine grained ash with a total thickness of 12 cm.</p>
		<p><b>Surge 10/1</b> - well-sorted medium-grained ash with charred and uncharred wood, thickness of 15 cm.</p> <p><b>Surge 10/2</b> – ash and lapilli with no laminations, thickness of 40 cm.</p>
		<p><b>Surge 11</b> - well-sorted fine-grained ash with charred wood, thickness of 15 cm.</p> <p><b>surge 12</b>- fine-grained ash, thickness of 5 cm.</p>
		<p><b>Surge 14</b> - fine- grained ash, thickness of 10 cm.</p>

Figure 13. Pyroclastic surge deposit sections with grain-size distributions with relative abundances (measured in the phi size scale) and corresponding sample site. Locations shown in Figure 14.

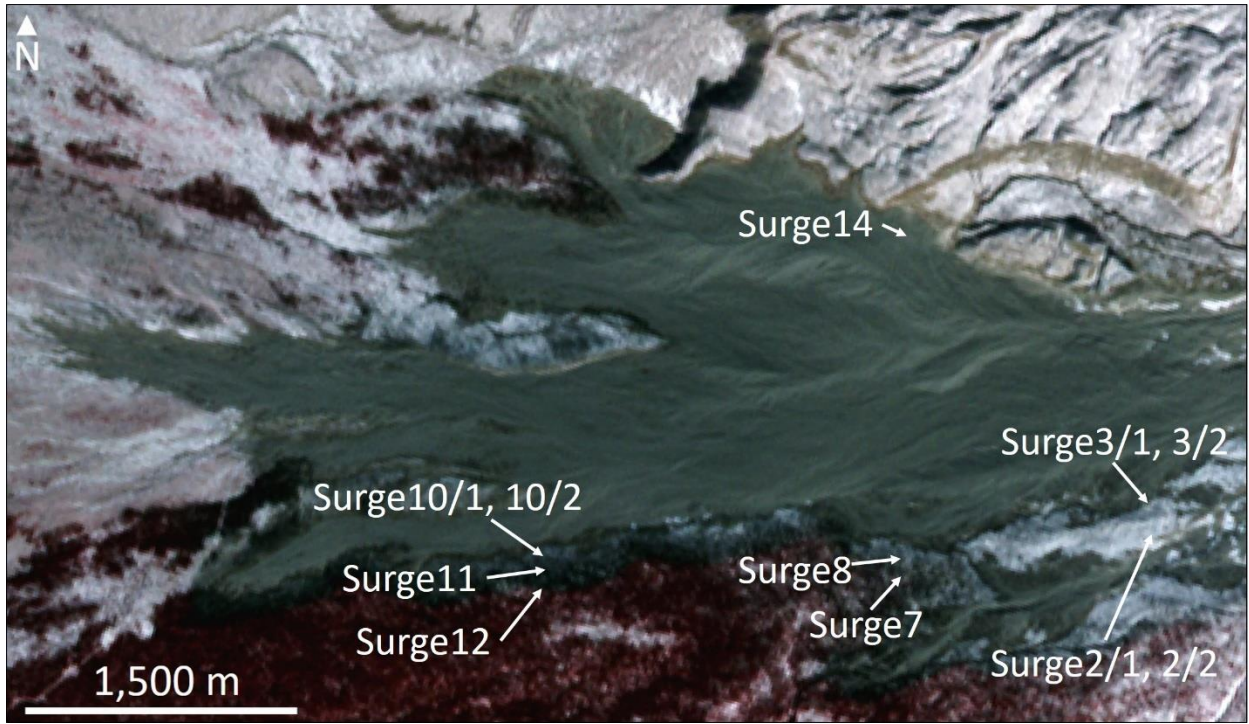


Figure 14. Locations of the surge samples that are described in Figure 13.





**Figure 15. a) surficial lineaments of lower-density andesite clasts on the surface of the 2005 deposit; b) the low-density bands were deposited along flow fronts (field notebook for scale); c) multiple flow fronts lined with the low-density clasts seen in drone footage (three people for scale in the black circle).**

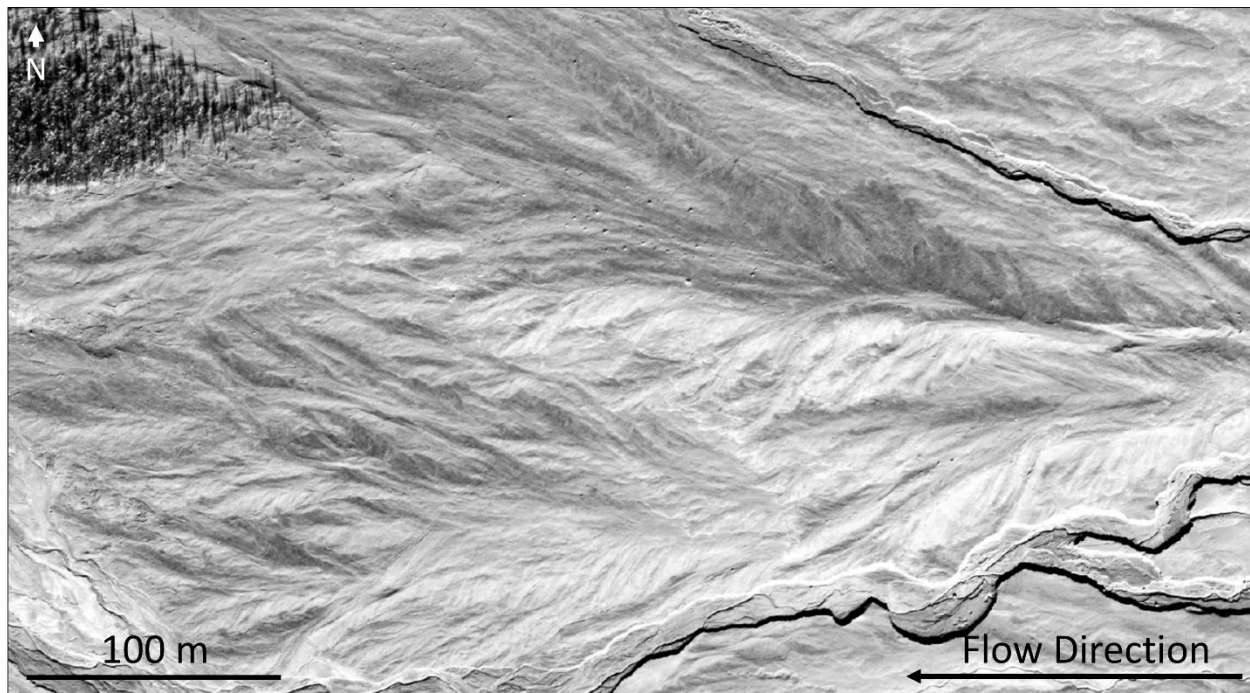
The proximal deposit area extends S-SW from the dome for 9.5 km along the western boundary of the 1964 debris avalanche deposit and the 1964 pumiceous pyroclastic flow deposit. The proximal area comprises an upper fan section that covers  $\sim 9.2 \text{ km}^2$  and has a length of 5 km and maximum width of  $\sim 2.3 \text{ km}$ . South of the upper fan, the deposit is concentrated in the Baidarnaya River channel for  $\sim 2 \text{ km}$ , after which it extends westward into a main deposit fan, including a smaller  $1.9 \text{ km}^2$  section that was emplaced slightly to the south where the BAF traveled over the channel wall.

The distal area comprises the bulk of the material in the main deposit fan where material was emplaced beyond the 1964 debris avalanche fan. The emplacement destroyed  $10 \text{ km}^2$  of forest, and buried the preexisting Baidarnaya River channel. The main deposit fan terminates in five lobes and has a surrounding fringe of singed trees that are clearly visible in satellite data and aerial photographs (Figure 16). Friable clastic material stranded on top of blocks protrude over 3 m above the surface and impact marks on standing trees indicate that the BAF was inflated to at least 3 m thicker than the resulting deposit.



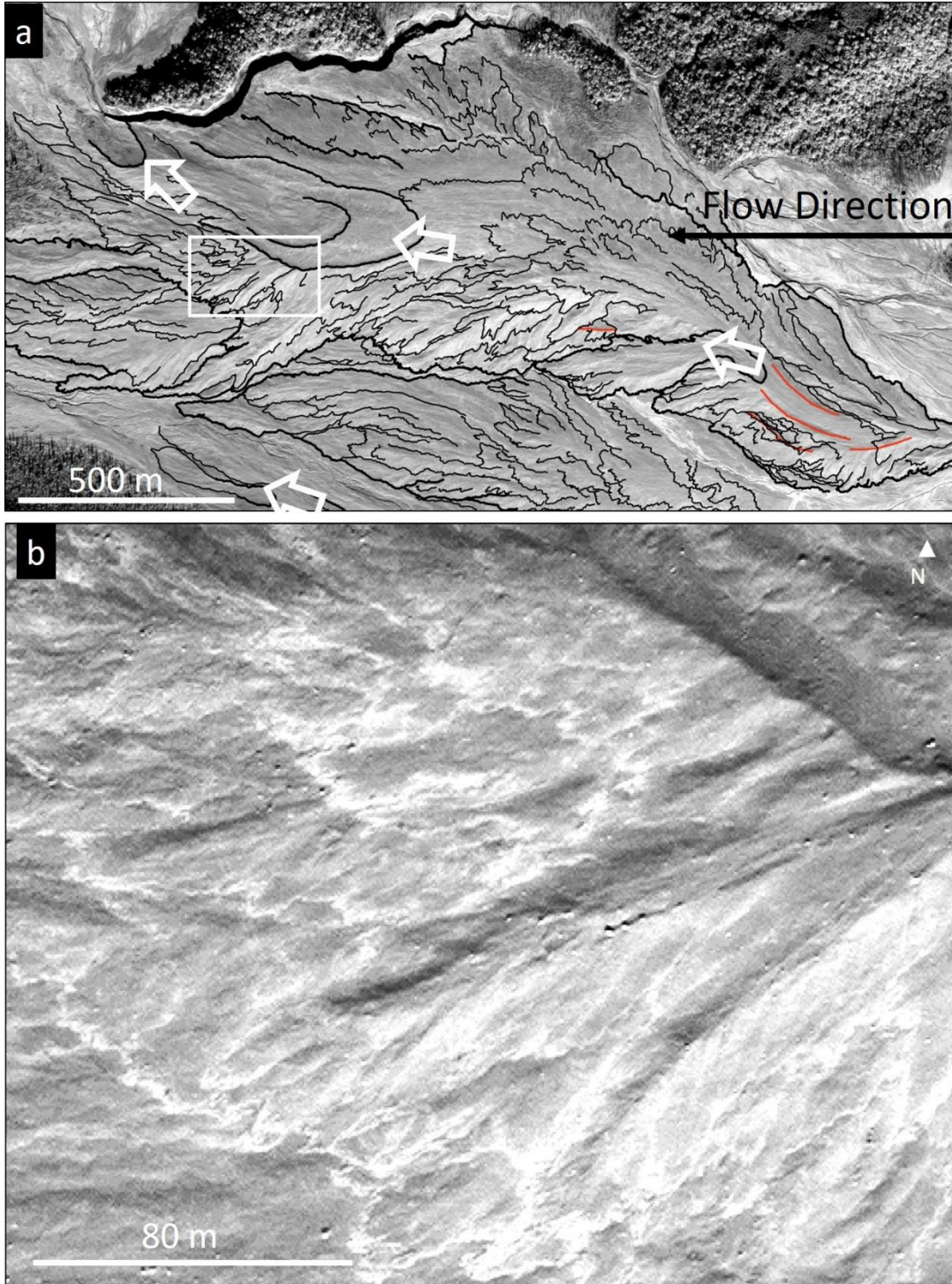
**Figure 16. a) Aerial photograph (looking west) of the 2005 main deposit fan. Band of singed trees (mostly larch and stone birch) up to several hundred meters wide bounds the toes of the 2005 block-and-ash flow deposit. The trees were damaged by low-energy, hot, and fine-grained pyroclastic surge that accompanied the block-and-ash flow. Helicopter views from the N (a) and SW (b).**

Areas of undisturbed deposit surface (Figure 17) are composed of the composite lobate facies with long and narrow (to ~180 m wide and exceeding 2,000 m long) sinuous channelized features with ridge and furrow morphology (levees are also sometimes present). Other areas are comparatively smooth with relatively diffuse boundaries. The channels and lobes radially spread out from a central channel in a dendritic-like pattern. The thickest deposit area is the northern section of the main fan, which is composed of a series of overlapping lobes with varying size, extent, and shape that become shorter towards the central apex, here termed composite lobate features (Figure 18). The composite lobate features contain numerous flow fronts that are visible throughout the deposit fan area. The easternmost/upstream end of the composite lobate feature contains two visible channels with the uppermost channel slightly offset from the underlying channel (Figure 18a).



**Figure 17. Sinuous lobate deposit surface with erosional channels on the 2005 main deposit fan. WorldView-02 image acquired on 29 September 2010.**



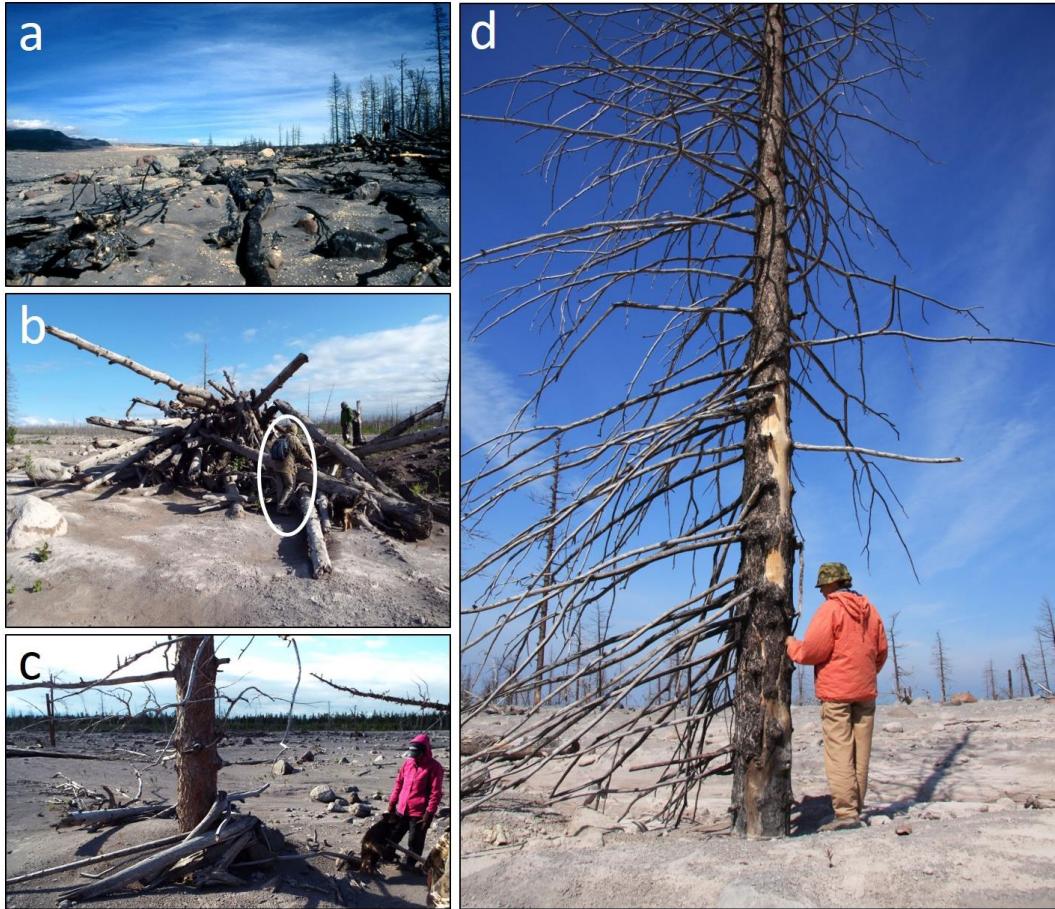


**Figure 18.** Singular pulses of material are indicated by bands of low-density material that were deposited at the flow front. a) Thin black lines annotate the bands, thick black lines are major flow boundaries, yellow lines outline channels, and white arrows indicate areas of remobilization; b) the white bands are visible in the QuickBird-02 scene acquired on 27 August 2010.

### 3.3.1.1 Vegetation damage

Trees that were overcome by the flow were either buried, or removed and transported to the distal edges of the deposit. Trees were generally deposited singularly or as tree dams where snags accumulated in piles with blocks exceeding suspended >2-3 m above the current surface of the flow (Figure 19). Logs and tree limbs are also observed in deposits that are piled against and wrapped around standing trees. Many of the standing and felled trees are stripped of their limbs while others still have branches attached. In addition, many of the trees have segments where branches were removed down to the bark collar, are frayed and sometimes charred, and surfaces contain impact marks and varying degrees of bark damage or complete removal. Some impact marks are charred. The degree of charring varies from completely charred (relatively rare) with portions of the wood burned away, charred at the base of snag in contact with the deposit, and charred smooth-topped stumps (possibly as a result of burning while upright in the hot deposit, causing the tree to topple). The highest degree of charring is found along the distal edge of fine-grained surge deposits (Figure 19a). There is a perimeter around the main body of the flow where the trees are killed but left standing, indicating of the extent of the detached pyroclastic surge.

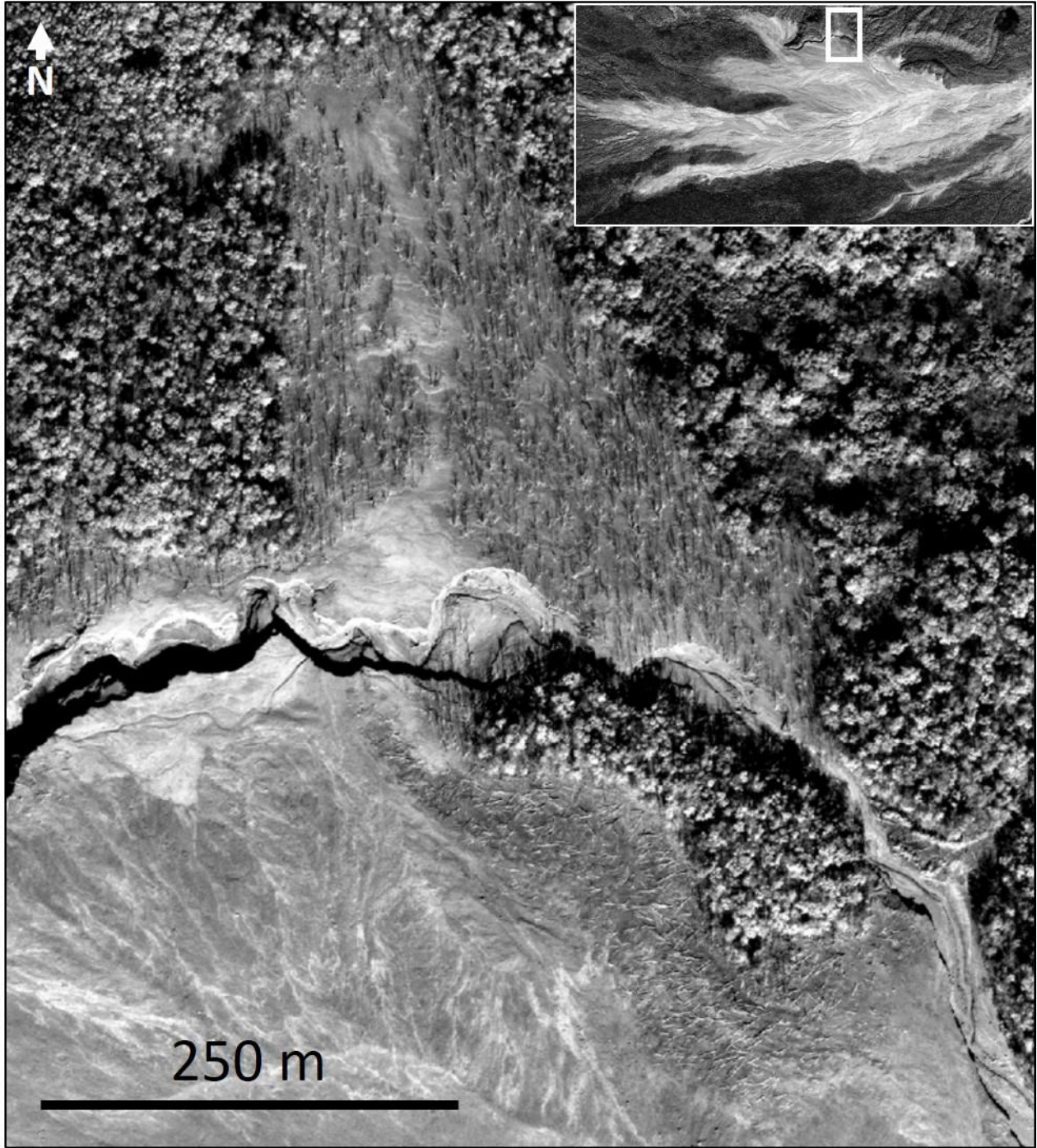




**Figure 19. a) knocked down and partly burned trees along the lateral edge of the 2005 deposit. Some of the trees withstood the dynamic action of the block-and-ash flow, but fell down some time later when the bases of their trunks were charred on the contact with the deposit.; b) tree dam at the distal edge of the 2005 main deposit fan, man in circle for scale; c) trees broken and wrapped around a standing tree; d) Bark and branches removed on the stoss side of the tree up to the height of 3.5 m above the surface of the 2005 deposit. The elevation of the damaged tree trunk indicates the thickness of the gas-inflated BAF before its final deposition.**

Examination of trees in the perimeter of the northernmost lobe of the main deposit fan showed no evidence of burning and some scattered trees survived. The deposit surface contains abundant 1964 vesicular andesite fragments and broken tree trunks and branches. This suggests that the surge was short-lived and not in contact with the trees long enough to cause carbonization. In 2015, it was noted that vegetation is beginning to re-grow in this area. Along the post-2005

eroded Baidarnaya River channel 12 km from the dome, the surge traveled upstream along a tributary channel and killed trees 640 m from the main deposit. Here, the trees are stripped of foliage by the flow but most remain standing. From a cursory inspection in the field, they do not appear to have any scorching or blackening of the outer surfaces. Nearby, the BAF left a 0.2 km<sup>2</sup> patch of living trees on a topographic high, surrounded by felled trees (Figure 20). On the southern slope of the topographic high the felled trees are largely pointing towards the southwest (directly away from the volcano), whereas, the surface patterns formed by the lower density accidental clasts indicate the direction the flow immediately prior to deposition to be towards the northwest. Some of these trees are still attached to their root wads by strands of wood or appear to have been bent over but not severed. These trees still have the papery bark largely attached and do not have surface charring.



**Figure 20. Four zones of vegetation damage: 1) complete tree removal and/or complete burial by deposit; 2) tree stumps remaining/felled trees in situ; 3) single zone where dead trees remain standing reaching over 280 m from the BAF deposit; 4) No tree damage.**



### **3.3.1.2 Deposit remobilization**

The surface of the thickest area of the 2005 deposit contains a series of four arcuate scarps over an area of 0.11 km<sup>2</sup> (Figure 18). The scarps are 3-4 m high and open to the west. Small parallel ridges that are perpendicular to flow direction are visible on the surface within the arcuate scarps. These ridges are visible in both the field and in the satellite data. These scarps are interpreted to be headwall scarps, and the surface that contains ridges is remobilized material. The three uppermost scarps are nested, indicating that they originated through a series of closely-spaced remobilization events. The fourth arcuate scarp is near the flow terminus and opens to the northwest into an open plain.

### **3.3.1.3 Degassing Structures**

Thicker regions of the 2005 BAF deposit contain circular areas a few meters in diameter and consist of a finer-grained, well sorted facies of the deposit with multi-colored precipitate rings consisting of organic growths and mineral precipitants (white to orange to green from the center to the edge, but, not all colors in every area). The surfaces surrounding these circular areas are comprised of finer-grained, ash (typically a few cm thick, to as much as 4 cm in the one structure). Some plants (<20 cm tall) have grown within a few meters of some of the degassing structures. The degassing structures have a higher thermal output than the surrounding deposit surface (they are still warm to the touch), and one that I visited was producing the smell of tar (Figure 21). The hottest of these structures was 52°C on the surface and had a maximum temperature of 83°C at 16 cm depth. The temperature of the BAF deposit nearby (but outside of the structure) at the same time was 13°C and was the same temperature from the surface down to 30 cm. These temperatures were measured using an infrared thermometer in 2015. These circular areas are interpreted to be the surface manifestations of degassing structures along the apex of deposit ridges.

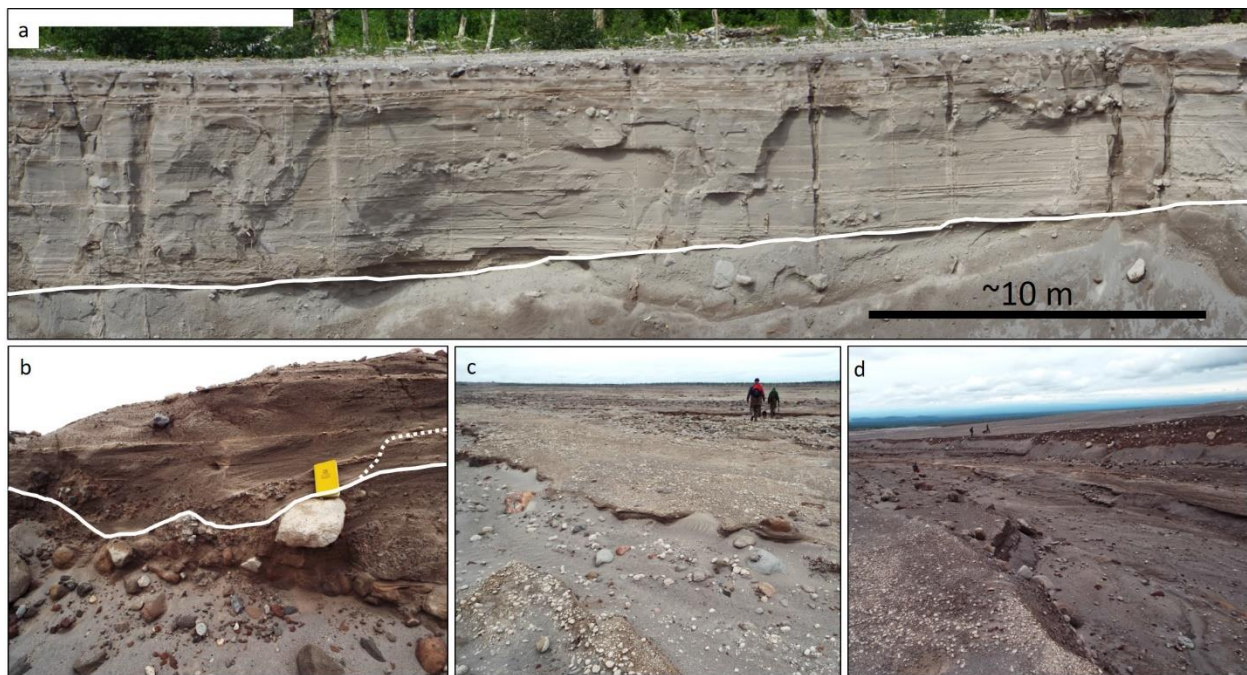


**Figure 21. a-b) The surface manifestations of degassing structures along the thickest area of the 2005 deposit (Figure 3), with surface discoloration and colored rings (field notebook for scale in white circle); c) a line of degassing structures (indicated by arrows) along the 2005 composite lobate feature, taken by done near the area of 14a and are similar size of those in the photographs.**

### **3.3.1.4 Erosion and redeposition**

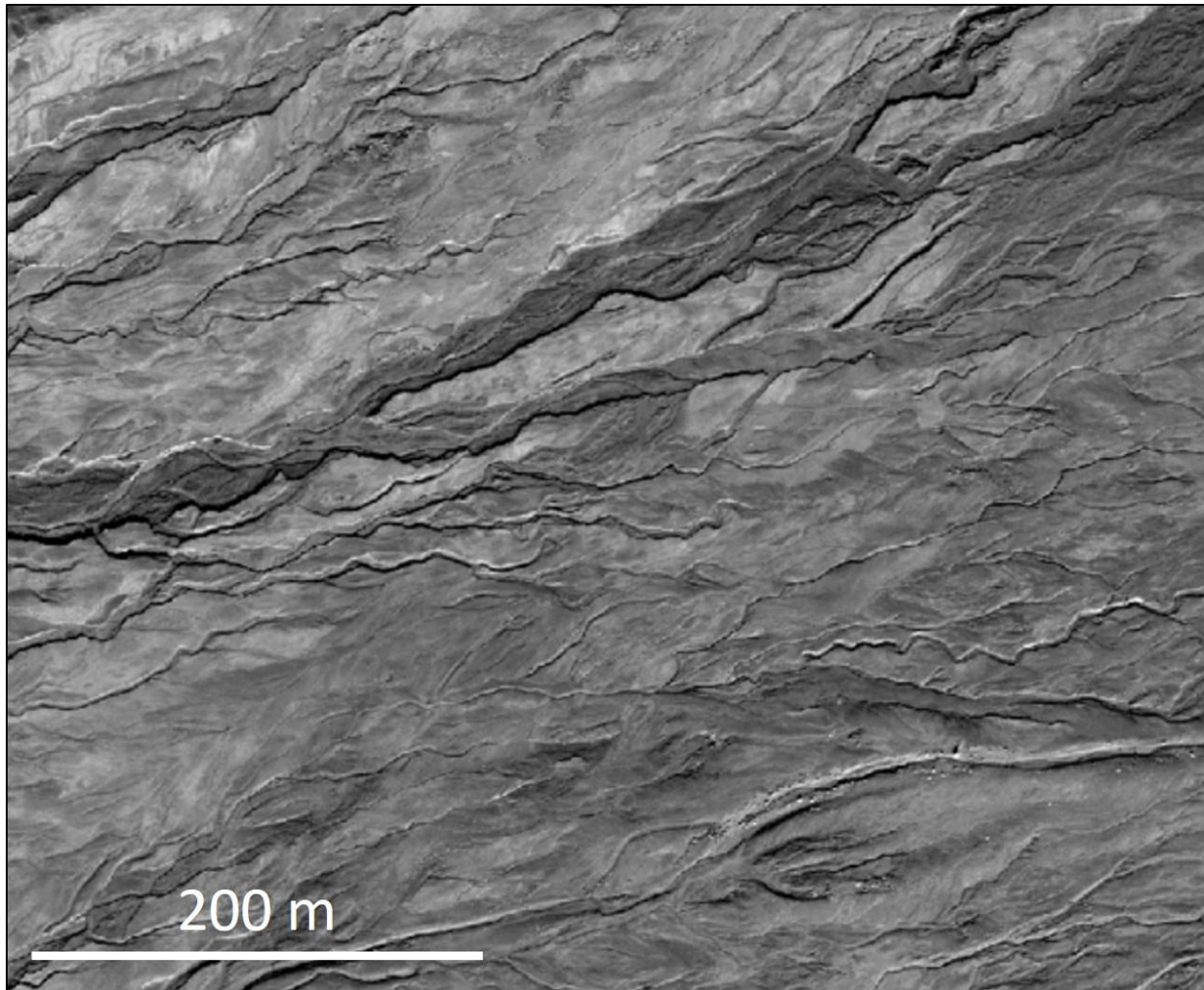
Approximately 40% of the 2005 main deposit fan (a total area of  $\sim 10 \text{ km}^2$ ) surface underwent erosion over 4.5 years between February 2005 and September 2010, when I visited the deposit. In 2010, reworked deposits were exposed in cross sections that cut through the 2005 deposit (Figure 22). The eroded areas are also visible in high-resolution panchromatic high resolution WorldView-02 satellite data as lighter in color (flatter areas reflecting more light) and covered with meandering and braided channels (Figure 23). Because erosion has preferentially removed fine-grained materials, the channels have an increased abundance of blocks. The edges of some channels are lined with lobate zones of low density vesicular andesite and wood that are

much higher in concentration, thickness, and width than the linear bands of vesicular andesite from primary depositional processes. This suggests that the andesite clasts floated at the top of the floods/lahars and spilled out over their channel walls. In places, the 2005 deposit is capped by laminated fine-grained reworked flood deposits and lahar deposits (distinguished by larger clasts and relatively fines-poor character) that overlie a sharp boundary. These laminated deposits show variations in grainsize but are mainly composed of ash and lapilli with intermittent beds or lenses containing larger clasts and vegetation. On the northern side of the Baidarnaya River channel, the reworked capping deposits are thicker (Figure 22), and in some areas of the southern wall they are absent or only a few centimeters thick.



**Figure 22. a) laminated water flow deposits with dispersed lenses of coarser clasts (above the white line) in the northern eroded channel which is up to 40 m-wide at this location. The channel is 1~ km long and erodes into the pre-2005 substrate, to a depth of over 18 m in places; b) erosion and deposition (above the white line) into the 2005 deposit along the southern boundary. The dashed line is where erosion took place into preexisting reworked deposits; c) the eroded surface exposing a higher number of blocks and with sheets of 1964 andesite; d) an eroded channel in the 2005 deposit up to 45 m wide (people for scale).**



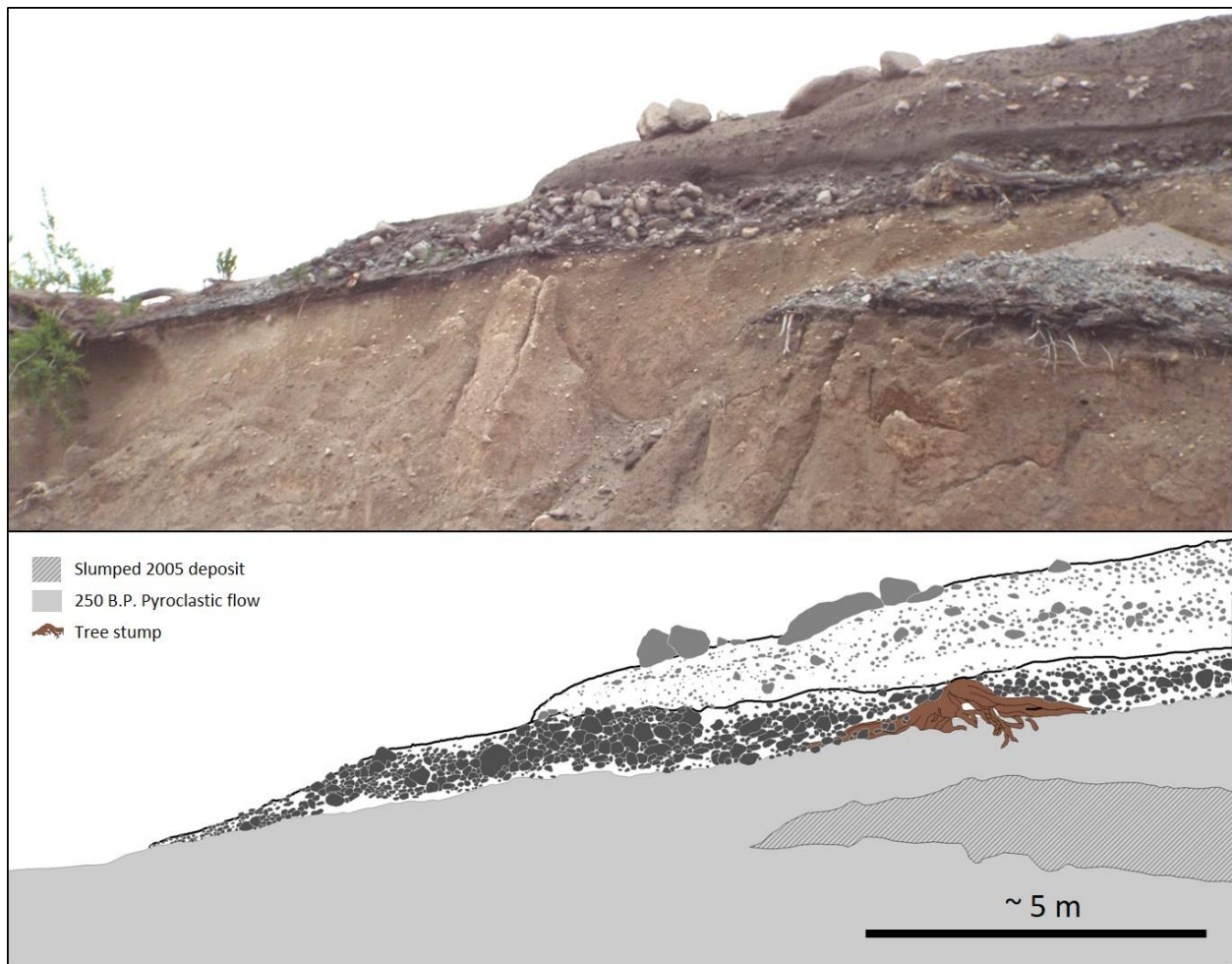


**Figure 23. The eroded surface of the 2005 block and ash flow deposit with braided and dendritic patterns. WorldView-02 image acquired on 29 September 2010.**

### **3.3.1.5 Stratigraphic exposures**

A stratigraphic section that was eroded into the southwestern section of the 2005 BAF deposit exposes the toe of the 2005 deposit where it overlies a pyroclastic flow deposit that was emplaced ~250 BP (Ponomareva et al., 2007) (Figure 24). This section is located 13 km from the dome. There is a sharp boundary between the underlying pyroclastic flow and the 2005 BAF, with

roots protruding out of a thin paleosol between them. The lowermost 2005 unit at this locality is fines-poor and has a relatively thick distal flow front. Here, a sharp boundary the 2005 lower unit from the upper unit, which is matrix supported and consists of two weakly-reverse-graded units. The base of a tree and its roots are also exposed here, and the trunk is truncated at the contact between the two 2005 deposit units, showing that the tree was sheared off the upper matrix-supported unit.



**Figure 24.** The distal end of a lobe located along the southern edge of the 2005 deposit. The underlying unit is fines-depleted and has a thicker termination, also visible on the other side of the erosional channel. The fines-poor unit is overlain by a matrix-supported unit.



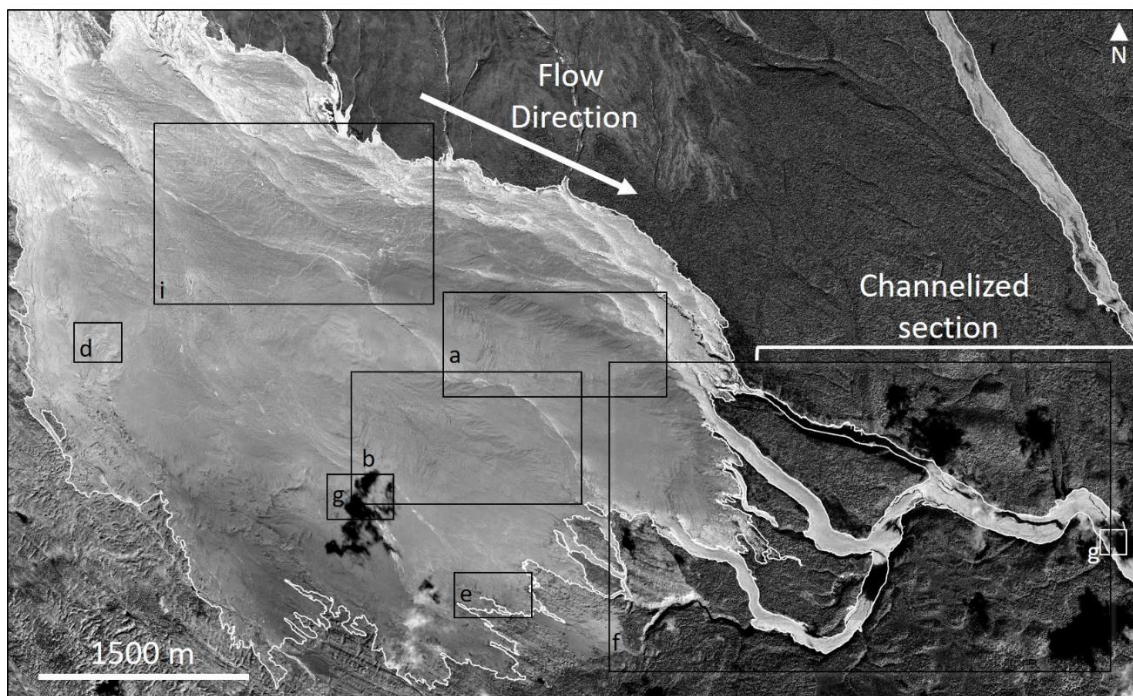
The largest vertical exposure through the 2005 deposit is present along the northern margin of the 2005 main deposit fan (Figure 25), where fluvial erosion has formed the new 25- to 50-m-wide by >1km long Baidarnaya channel. Multiple stages of erosion have cut terraces into the deposit in this area. On the southern wall of this channel, the river channel exposes a stratigraphic section of the deposit that is more than 20 m thick, while the northern wall of this channel is almost entirely composed of older pre-2005 deposit, including newly-dissected 7000-year-old maar deposits (A. Belousova, pers. comm.). Exposures near the distal end of the channel reveal a rapid thinning of the deposit towards its northern distal end.



**Figure 25. The southern wall of a cross section cut by the Baidarnaya River with reversely-graded units indicated by white arrows. Note that no fresh deposits are on the northern (right) side of the channel.**

### 3.3.2 Shiveluch 2010 BAF Deposit

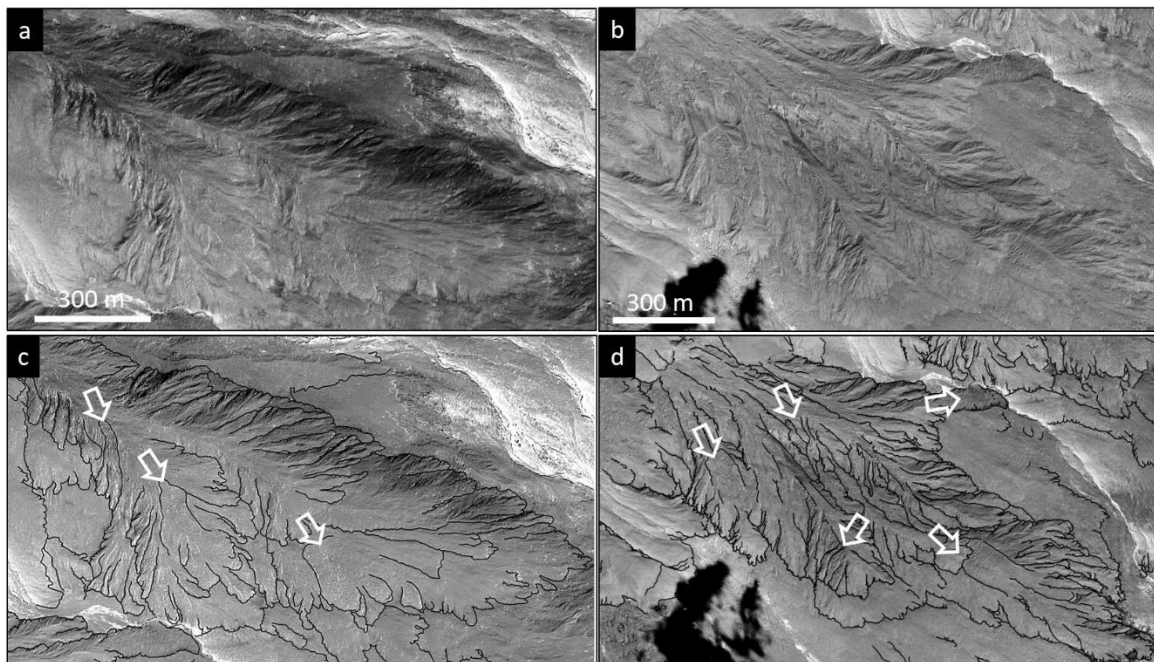
The eruption description and distribution of the October 2010 dome collapse and resulting BAF deposit are described in Chapter one. The following results discuss the 2010 BAF main deposit fan and the channelized deposit that continued to the SE for 5.4 km beyond the distal edge of the fan. The locations of the following figures are given in Figure 26. The deposit above the fan is visible in ASTER TIR data and appears to be thin and patchy. This is evident from the lower degree of snow melt in this area after post-emplacment snow deposition in ASTER VNIR images, and is not discussed further here.



**Figure 26. The Shiveluch 2010 BAF deposit (panchromatic QuickBird-02 scene acquired on 27 August 2013). The white boxes and letters indicate areas where the photographs in the following section were taken. The black boxes and letters indicate the areas of the figures that are enlargements of this WorldView-02 scene. a) Figure 27a, c; b) Figure 27b, d; c) Figure 28a d) Figure 28b; e) Figure 29; f) Figure 30; g) Figure 31; h) Figure 32 (WorldView-02 scene acquired on 19 March 2011 used in Figure 29 due to shadow in the 17 August 2013 scene); i) Figure 33.**

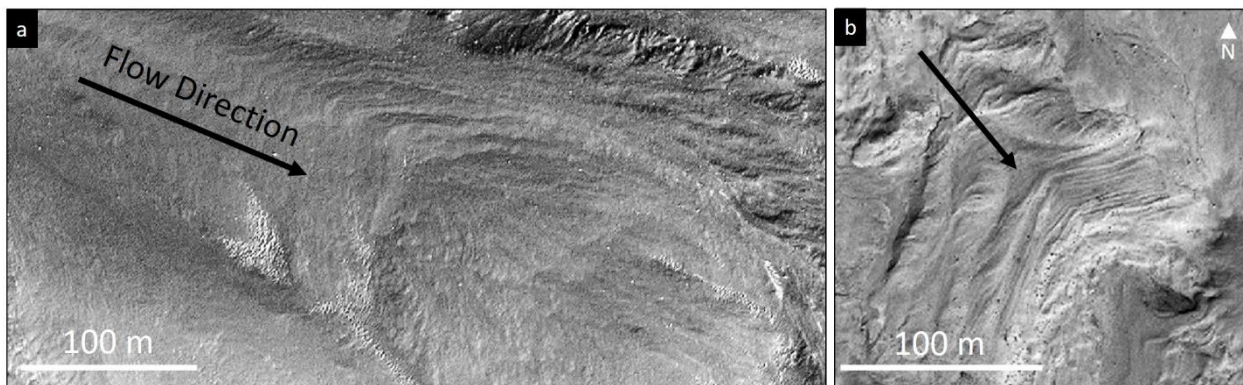


The 2010 main deposit fan covers an area of 16.2 km<sup>2</sup>. Approximately 9.5 km from the dome, the main deposit fan has two large composite lobate features with differing flow lobe morphologies and overlapping relationships (Figure 27). These two composite lobes vary in size (>750 m wide) and distance from source (to 12 km). Within these composite lobes, the largest singular lobes display dendritic ridge and furrow morphologies, and some levee and channel features >30 m wide. Most of the furrows and channels have been filled by deposits of slightly younger flows. Lobes vary in surface roughness, block contents, and degree of toe development. In some areas, larger surface blocks are concentrated in these channels. Blocks of dome rock with diameters up to 7.5 m were deposited at the distal reaches of the flow, at distances of >12 km from the dome. The composite lobe surfaces contain arcuate scarps upstream of areas of rough deposit surfaces and of smaller lobes. These are interpreted to be zones of shallow deposit remobilization.

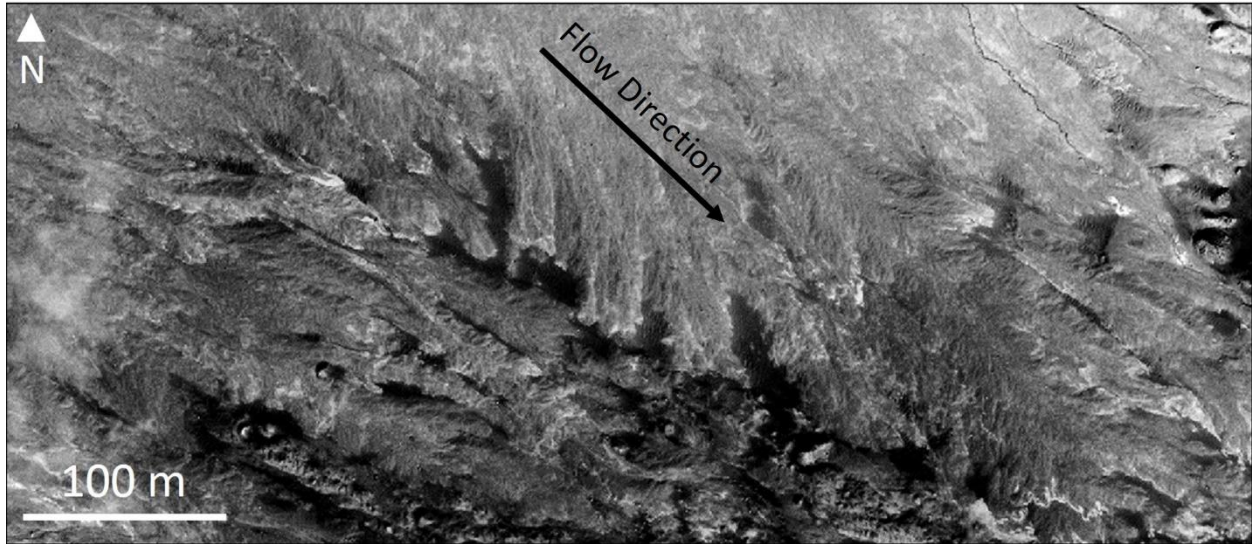


**Figure 27. a) The main deposit fan of the 27 October 2010 block and ash flow deposit and the channelized section that continued for 5,400 m; the composite lobate features are shown in b and c with black lines in d and e indicate the lobe fronts. White arrows indicate the location and direction of remobilization. Images are of the QuickBird-02 scene acquired on 27 August 2013.**

Evidence of the flow interacting with underlying topographic highs is present in the main deposit fan, with bifurcating flow and herringbone features (Figure 28), and material onlapping onto, or depositing around, underlying hummocks. The southern perimeter of the 2010 main deposit body has a higher proportion of vesicular andesite, within both sheet-like and elongate lobate deposits. The distal fan deposit area also contains elongate lobes (up to 130 m- wide but usually under 30 m) and they have diffuse feathery flow boundaries (Figure 29). The surfaces of these deposits have very few large blocks; only a few large enough to be visible in the high-resolution satellite data. The feathery lobes deposited onto the underlying 1964 debris avalanche deposit and in places were redirected by the hummocky surface topography that includes linear ridges and troughs.



**Figure 28. Herringbone structures on the 2010 deposit a) 8,000 m and b) 8,500 m from the dome (QuickBird-02 scene acquired on 27 August 2013).**

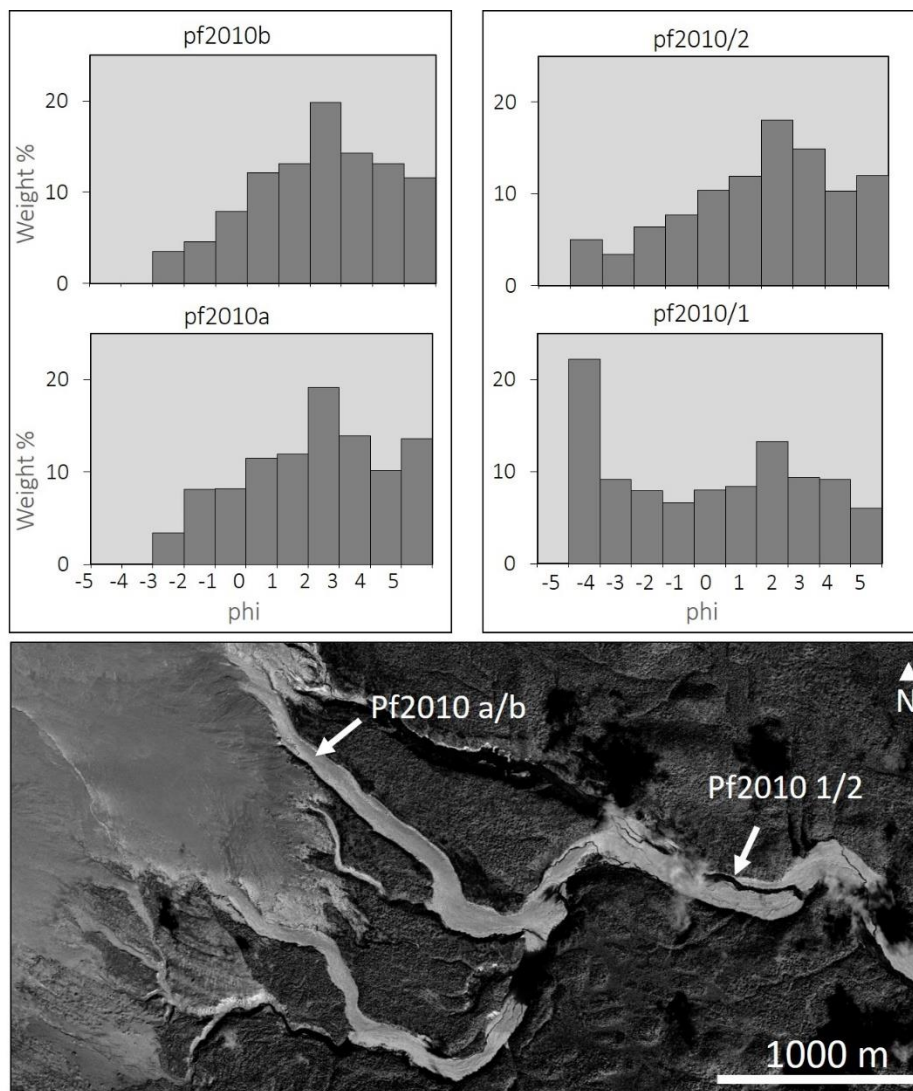


**Figure 29.** Feathery lobes in the 2010 deposit, 11,000 m from the dome. Here, the distal deposit was emplaced onto the hummocky 1964 debris avalanche deposit (QuickBird-02 scene acquired on 27 August 2013).

### **3.3.2.1 2010 channelized deposit**

The 2010 BAF traveled down two river channels at the distal reach of the BAF, converged into the Kabeku River channel, and then flowed for an additional 5.4 km (Figure 30). The Quickbird-02 scene data show the surface of the channelized section. Lobe and remobilization features similar to those on the main fan deposit are present in this area. The scarps are arcuate, and the surface of the remobilized material is irregular, and the terminations are lobate. The current river has exposed an outcrop through the entire deposit (Figure 31) showing a mainly massive, poorly sorted, matrix-supported deposit. Some areas contain discontinuous horizontal concentrations of blocks, usually in the upper portion of the deposit. The channel is up to 11 m deep, with over 6 m of deposit visible above the talus slope. The base of the channel is likely at or near the old channel bed as indicated by presence of regrown plants, assumed to be due to the recovery of pre-deposition root-stock. At this locality, nearly 14 km from the dome, the channel is ~170 m wide. The lower few meters of the exposed deposit has a grey ash-rich matrix,





**Figure 30. Grain-size distributions with relative abundances measured in phi. The samples pf2010b and 2010/2 were overlying 2010a and 2010/1, respectively. Locations are shown on the QuickBird-02 scene acquired on 27 August 2013.**

whereas, the upper 90-100 cm contains a brown ash-rich matrix with a gradational boundary between the two subtle changes in color, likely due to the upper surface being oxidized. In one area, there is a horizontal section containing a higher concentration of subangular to subrounded blocks at the otherwise gradational boundary. The deposit with the grey ash-rich matrix appears to contain a higher proportion of relatively large clasts up to 20 cm in diameter. The Kabeku River

channel contains greater amounts of clasts of vesicular andesite and variably-charred wood fragments on the surface that were emplaced as thin sheet-like deposits. The 1964 andesite clasts are light brown in color, as opposed to the usual white that the dominant clast type of the deposit fan. Small surface hummocks are present on the channelized deposit surface; they are especially common at a bend in the river channel.



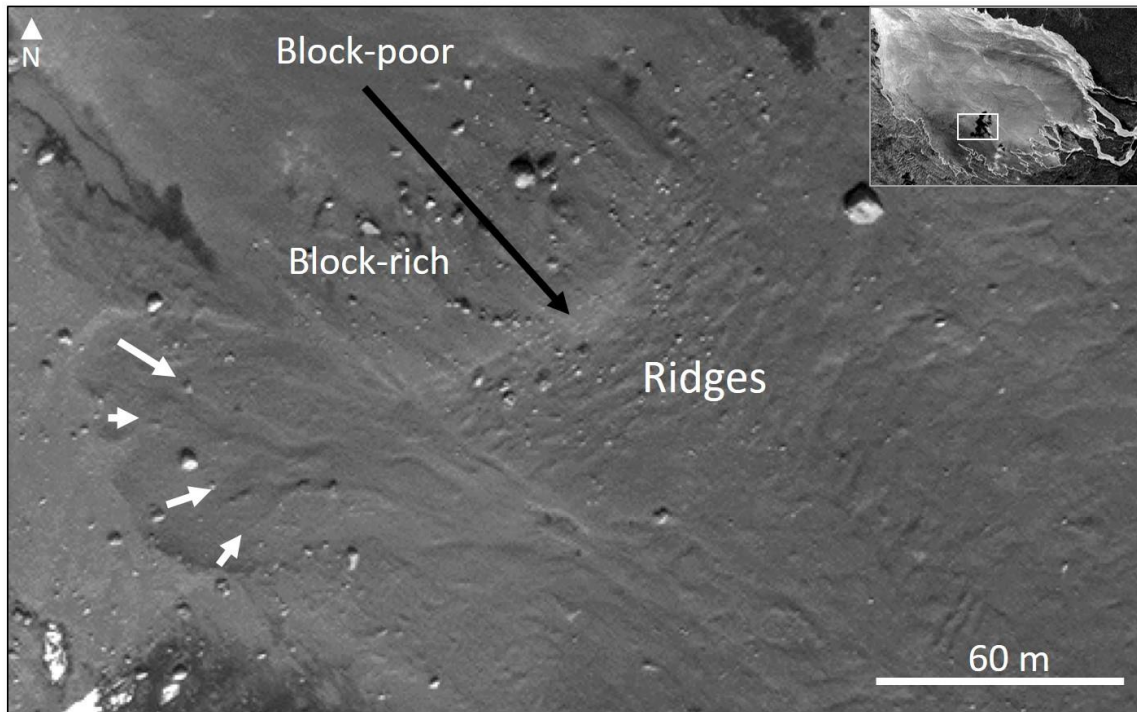
**Figure 31. Cross section through the channelized 2010 deposit ~14,000 m from the dome where the deposit is cut down to the original riverbed surface.**

In the Kabeku River channel, the trees along the upper valley walls are scorched (blackened) and bent in the direction of flow, indicating an inflated zone of high temperature flow. The amount of damage to the vegetation within the channel varies locally, with damage ranging from felled trees (still attached to the base) but no signs of burning, to carbonized and charred snags, and to trees that are removed completely (no longer attached at the base). All of these tree types are exposed within a short distance of each other. The degree of damage to the bark varies from none, with the papery bark remaining, to completely stripped. Within a section of the newly

eroded channel (down to the previous river bed) remaining tree stumps display no burning of the basal ~0.5 m, whereas the sections above this level are charred and then above this level, the top of the trees were removed completely at 2-3 m. Roots are exposed at the base of these trees.

### 3.3.2.2 Ridges and scarps

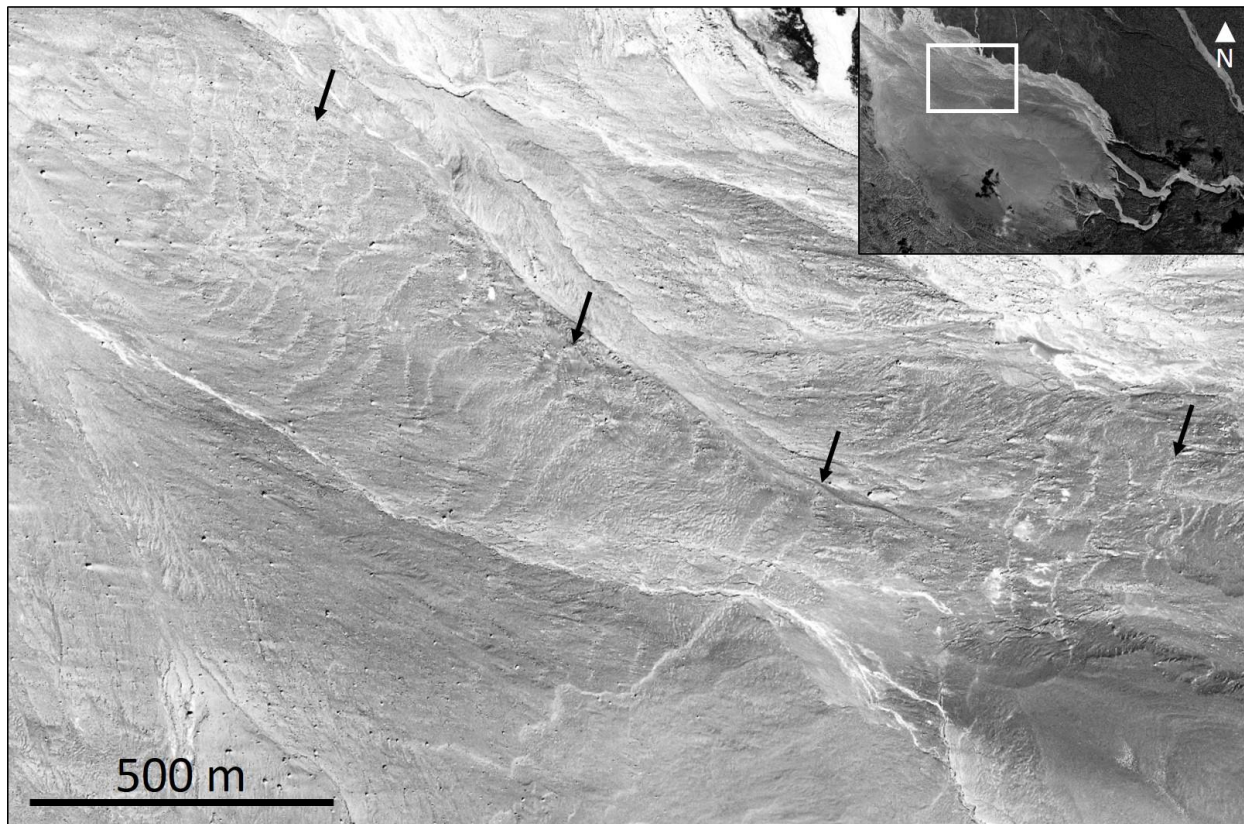
An area of the 2010 deposit (Figure 32) ~9.7 km from the dome contains multiple parallel ridges that are perpendicular to flow direction. Here, the surface block abundance varies sharply within short distances. The surface of the lowermost unit in this section that contains these ridges has a moderate surface block content overlain by a ~50 m long section containing a much larger range of block sizes (up to ~5 m in length), and the uppermost layer has only a few scattered blocks, grading to areas with no surface blocks present.



**Figure 32. Varying block contents over a short distance with the smoother block-poor deposit surface in the upper left of the image. Black arrow indicates flow direction and white arrows indicate deposit remobilization (QuickBird-02 scene acquired on 27 August 2013).**



Bench and scallop topography is common in the 2010 deposit. In the northeastern section of the 2010 main deposit fan there is a series of around 30 parallel benches up to 400 m-wide with a maximum of 80 m between them (Figure 33). The lowermost bench has a height of 180 cm. Field investigations revealed numerous degassing structures and small hummocks in this area. Narrower benches occur to the west of this section. South of these benches, the scarps are more scalloped or arcuate in shape. These structures such as these are present over a significant proportion of the 2010 deposit.



**Figure 33. Bench and Scallop topography (area indicated in inset image) with black arrows indicating four out of the ~30 benches present. Black specks in the image are large blocks on the deposit surface.**

### **3.3.2.3 Erosion**

A QuickBird-02 scene acquired nearly three years after the emplacement of the October 2010 deposit (on 27 August 2013) shows that fluvial erosion was limited to the areas around the thickest deposit regions and to a strip along the northernmost fan boundary that was up to 500 m wide. Over this time, 15% of the deposit surface was eroded, and shallow sinuous channels formed.

### **3.3.2.4 Degassing structures**

Degassing structure surfaces occur on the 2010 deposit fan, and have the same characteristics as those described in the 2005 deposit. The features appear in clusters along the thickest areas of deposit and below the benches described above.

### **3.3.2.5 Surface block content**

Outsized blocks up to 12 m in diameter litter the deposit surfaces of both the 2005 and 2010 deposits (Figure 34). The blocks are dome rock that are characterized by oxidation and vesicle banding. In the composite lobate areas, surface blocks are sometimes concentrated within the central channels of channel and levee formations. Surface block abundance rapidly change over a short distance. Concentrations are expectedly much higher in eroded areas as finer material has been removed, and suggesting that some of the blocks were formerly embedded within the deposits. Many blocks show evidence of clast interactions and stress during transportation in the flow such as randomly-oriented impact marks and fracture networks. Some blocks are fractured to the extent that fragments can be broken off by hand (probably containing microfractures). The impact marks on the block surfaces are both rounded and elongate.



Figure 34. Large blocks of dome rock, a) 12 km from the dome base on the 2005 deposit, b) 15 km from the dome base in the 2005 deposit, c) 10 km from the dome base in the 2010 deposit, and d) 13 km from the dome base in the 2010 deposit.

### 3.4 DISCUSSION

The parameters of the 2005 and 2010 BAF deposits are summarized in Table 9. The 2005 and 2010 BAF deposits were produced during gravitational collapse of the active Shiveluch dome over the course of 6.8 hours and 6.7 hours, respectively (Ovsyannikov and Manevich, 2010, Kamchatka Volcanic Eruption Response Team (KVERT report 28 October 2010). As discussed,

the two deposits are composed of fragmented heterogeneous dome material and entrained material from the underlying 1964 debris avalanche and pyroclastic flow. There is no evidence that the collapse involved dome rock with significant melt as the deposits contain no observable breadcrust bombs.

**Table 9. Summary of the 2005 and 2010 block and ash flow (BAF) deposits. Deposit and collapse scar values are from Chapter one.**

	<b>27-28 February 2005</b>	<b>28 October 2010</b>
Collapse scar area (km <sup>2</sup> )	0.86	1.17
Collapse scar max. width x length (m)	550 x 2400	1100 x 2540
BAF runout distance (km)	15.6-17.8	16.4-19
BAF runout from dome base (km)	15.4	15.7
BAF deposit area (km <sup>2</sup> )	24.1	22.3
Maximum deposit width (m)	2490	4100
Flow direction	SW, W	S, SE
Channelized deposit length (m)	2000	5400
Main deposition begins (m from dome base)	9500	7300
Breadcrust bombs?	No	No
Levee/channel	Yes	Yes

There is little evidence of strongly hydrothermally altered rock (yellow-orange colored, disintegrating, and containing clay) from the dome. The presence of rounded and elongate impact marks on the surfaces of boulders indicate both collisional and longer-duration frictional interactions during transportation (Dennen et al., 2014). Rare elongate impact marks show evidence for impact-induced melting with an outer glassy (psudotachylite) layer. This is also seen on blocks in 1998 BAF deposits on Merapi volcano, and in the 1995-1999 BAF deposits on Soufriere Hills (Grunewald et al., 2000; Schwarzkopf et al., 2001).

In Chapter one, footage of the December 2013 eruption event showed multiple pulses of collapse that formed the BAF deposit. In previous sections (in this chapter), the morphology and

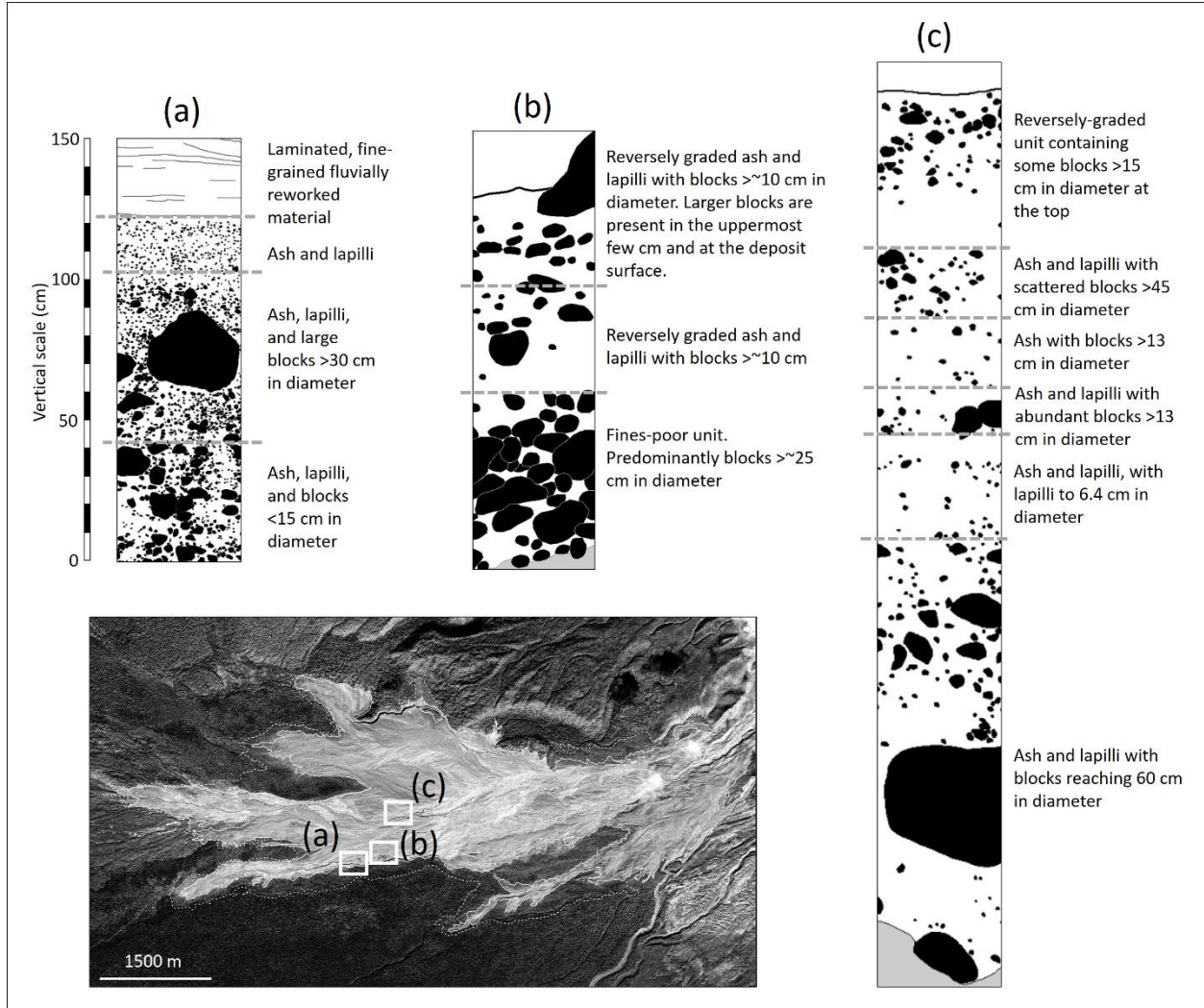
stratigraphy of the 2005 and 2010 BAF deposits are characterized using field and satellite data to explore this unsteady, retrogressive, pulsatory collapse mechanism occurring during these larger events. BAFs are unsteady currents with instabilities that originate both from the source via unsteady collapse (Cole et al., 2002; Loughlin et al., 2002), and from kinematic waves developing, which has been described for BAFs and debris flows (Iverson, 1997; Schwarzkopf et al., 2005). It is likely that both of these processes contributed to the resulting deposits.

A pulsatory dome collapse event could be expected at a large dome that has been extruding viscous lava and is producing ash explosions around different locations, as Shiveluch has been doing since 2001. Events such as this likely created instability in the dome rock, and the steep walls of the collapse scars became unstable and continued to collapse over periods of hours during the eruption to produce multiple BAF units that formed one large eruption deposit. Supporting evidence includes different degrees of fragmentation and thermal heating (oxidation banding) within blocks in the deposits, which likely represent different areas of the dome – such as hot, more gas-rich inner parts of the dome, and the outer/older, cooler, degassed dome carapace.

The variations in surface block abundances across similar distances from the dome show differences in the ability of dome rock to break apart during transportation. Because the blocks traveled the same distance over the same or very similar surfaces, this implies that the cause for the difference in abundance is due to heterogeneity in the collapsing dome rock. The areas containing higher concentrations of large dome blocks likely originate from areas of the dome that have undergone higher degrees of degassing (outer and/or older areas of the dome). Areas lacking surface dome blocks are likely from the more gas-rich areas of the dome, resulting in more extensive fragmentation due to gas-related autobrecciation during transportation.

Several stratigraphic sections were cut through the 2005 deposit by fluvial erosion to expose sections to over 20 m thick (Figure 35). In some places, these sections contain discontinuous units, which laterally grade into massive and containing no units. The deposit sections contain units that underlie the overlapping lobate deposit surfaces, while the massive deposit sections that lack the internal units underlie the areas lacking surface lobes. The stratigraphic data are limited as the eroded sections are parallel to the direction of flow, and no perpendicular sections are available. The erosion in the 2010 main deposit fan area is still shallow and not as extensive as the 2005 deposit. Time in the field was also limited due to the dangerous nature of Shiveluch volcano. More time would have allowed a more extensive investigation, and allowed more features identified in the satellite data to be described. During previous field work, exposures were cut into the surge deposits that surround the 2005 BAF main deposit fan area. They contain degassing pipes which gives evidence for the high gas content during deposition. The surge traveled up to 300 m from the BAF deposit, killing vegetation out to a sharp boundary that is visible in aerial photograph and orbital remote sensing data. Detached pyroclastic surges have traveled further than this on other volcanoes. The November 2010 eruption of Merapi volcano in Indonesia produced a BAF with an associated surge that extended up to 10 km from the main deposit (Cronin et al., 2013).





**Figure 35. Three stratigraphic sections in the 2005 main deposit fan that show the discontinuous nature of the units within a 550 m distance.**

The BAFs were highly erosive and entrained significant amounts of 1964 pyroclastic flow material. Lower-density material bands of 1964 materials and wood fragments in the Shiveluch BAFs are present in the earliest and latest surfaces emplaced during the eruption, which suggests that substrate entrainment occurred throughout the eruption, even as the flow was waning to produce shorter runout distances and emplace material towards the rear of the thickening deposit

(Figure 5). Channel and levee structures (most apparent in the 2010 deposit) indicates that the system formed as a result of levee breakouts, similar to levee breaches seen on the Mount St. Helens ignimbrite fan (Branney and Kokelaar, 2002). Ridge and furrow structures along with the concentration of low density material at deposit margins was also described by Cole et al. (2002) in the unconfined regions of the Soufriere Hills 1995-1998 eruption deposits. The authors attribute this to: (1) the flow front entraining low-density material (which concentrates towards the upper surface and front of the flow); (2) the lower flow region decelerating and emplacing material, while the overlying material continues forward; and (3) the final deposit being emplaced such that material is stranded on large blocks. Such a transport model can also be applied to the Shiveluch BAFs. In addition, and similar to, the BAFs at Merapi volcano (Schwarzkopf et al., 2000), the features described here indicate that the 2005 and 2010 Shiveluch BAFs were unsteady granular flows that deposited starting at the flow front and progressing rearward and upward.

The remobilized surface features are groups into three facies: 1) parallel linear scarp, 2) arcuate scarp, and 3) curvilinear bench and scarp facies. Secondary lobate deposits occur below the arcuate scarp, and scarp and bench facies, both in the main deposit fans and the 2010 channelized deposit section. During or soon after deposition (while subsequent material was still being transported and emplaced) portions of these thick lobes were transported forward, forming deposits that continue for over 500 m from the scarps, and terminated either in lobate deposits similar to the primary deposition features or in more rounded bulbous lobes with several ridges parallel to the lobe front. The areas below the scarps are often rough compared to the smoother primary deposit surfaces, and contain short ridges (meters wide) perpendicular to flow direction. Direct evidence for syn-depositional remobilization is seen in the 2010 deposit, where one of the earlier lobes shows evidence of remobilization (ridged surface, scarp flanks, and new lobes



emanating from these areas). These syn-depositional features are likely due to inflation of the BAF as a consequence of initially high gas content. Evidence for high gas content is also shown by the presence of degassing structures on the deposit surfaces. Secondary pyroclastic density current deposits have also been noted in the 12 June 1980 Mount St. Helens pumice plain hours after the eruption and they occurred within the 1991 Pinatubo ignimbrite deposits for as long as two years after emplacement (Rowley et al., 1981; Torres et al., 1996).

Different flow pulses are also recognized on the basis of varying surface block contents (Figure 19). The concentrations of large dome blocks differ in overlapping sections of the deposit, indicating different degrees of fragmentation in subsequent flow pulses. A retrogressive, pulsatory dome collapse style is further supported by data from cross-sections through the deposits. Extensive cross-sections have developed along the northern edge, within the center, and along the southern edge of the 2005 deposit. The presence of stacked, multiple reversely-graded units coincide with areas of overlapping lobate deposits and areas lacking internal structure coincide with areas lacking such surface features. Thus, when studying older deposits in the field, it should be noted that: (a) stratigraphic subunits within large BAFs are discontinuous and therefore may be completely lacking in some areas (so may be missed), and (b) if reversely-graded units are visible in cross-sections they may be interpreted as smaller BAF events, but could be part of a much larger eruption with multiple subunits within one larger eruption deposit. This has obvious implications for determining the eruption history at volcanoes where individual eruption size is being determined in order to estimate future volcanic hazards and the distribution and magnitude of potential eruptions.

The channelized section of the 2010 deposit occurred before the final stages of emplacement. Prior to the 27 October 2010 event, the Kabeku River channel extended much closer

to the dome, providing a large distance (over 7 km) where the flow may have entered the channel. The point of entry is no longer visible as deposition that occurred later in the eruption sequence was emplaced over the channel area. This includes a thick composite lobe. The channelized section is determined to be primary (not remobilized material) due to: 1) the lobes present on the surface that are not emanating from a scarp source, 2) the presence of small hummocks that are also seen in the main deposit fan area, 3) the remobilized deposit features on the deposit surface, 4) the subsequent deposition of BAF material in the main deposit fan area, and 5) the dead trees that were killed and bent towards the direction of flow up the Kabeku River channel walls above the deposit surface, probably from an overriding ash plume. The channelized section of the 2010 deposit also shows evidence for unsteady flow behavior through localized changes in tree damage. Exposed tree snags in the eroded channel incurred burning to the top of the tree, but none at the base. This could be due to the initial pulses of flow mixing with snow and ice and cooling before it got to this point >15 km away from the dome. Whereas, subsequent flow pulses moved over the that deposit while retaining more heat. Alternatively, the initial pulses of the flow comprised a large volume of the outer cooler carapace of the dome, and later pulses incorporated a larger proportion of the inner, hot dome material.

Confirmation of a pulsatory collapse style at Shiveluch was provided by KVERT webcam photos taken of the 3 December 2013 BAF event, and documented three large collapse pulses that caused energetic pulses that extended to the end of the deposit, as well as numerous smaller pulses occurred before, between, and afterwards. This eruption produced a deposit with a maximum runout distance of 13.6 km, from a dome collapse scar with a planimetric area of 0.4 km<sup>2</sup>. This smaller episode was recorded over six hours before nighttime prevented further observation (chapter one).

Small hummocks are present on surfaces of both deposits. On several hummocks, blocks or log pieces are seen protruding from the interior. These appear to be small-scale hummocks like those described by Glicken (1996), where increased basal shear stress decelerates the material (in this case due to a block or log deposited on the surface) and causing it to pile up around the object (Figure 36). Small hummocks were noted at the northernmost point of the 2010 deposit (8.2 km from the dome), and in the channelized portion 13.4 km from the dome, and were less common on the 2005 deposit although this could be due to extensive erosion.

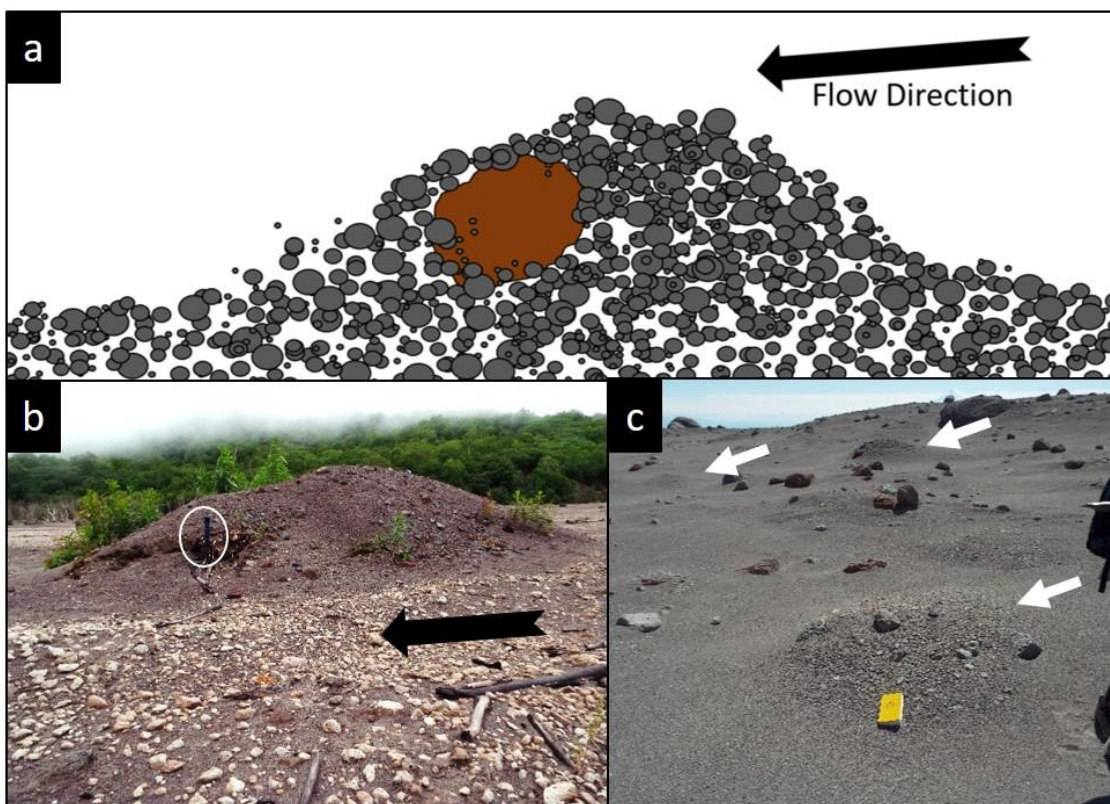


Figure 36. a) small surface hummocks are formed over and around blocks or portions of logs; b) 0.9 x 3.7 m hummock in the channelized 2010 deposit >14 km from the dome (rock hammer for scale in white circle). A portion of tree trunk/branch is protruding out the side; c) small surface hummocks (white arrows) on the 2010 deposit >8 km from the dome. Flow direction is indicated by the arrows.

Implications of these results from Shiveluch should be considered in field investigations of other dome collapse deposits, and in numerical modeling efforts. These large deposits contain discontinuous units that are absent in many cross-sections. Many BAFs undergo rapid erosion that remove sections containing internal structures that are important for interpretation, for example by removing evidence of multiple pulses during eruption. Or multiple units could be misinterpreted as indicating separate smaller eruptions if more complete sections are not exposed. Physical models should take into account that such large deposits as those at Shiveluch can be emplaced in multiple stages throughout an eruption to form a single large deposit.

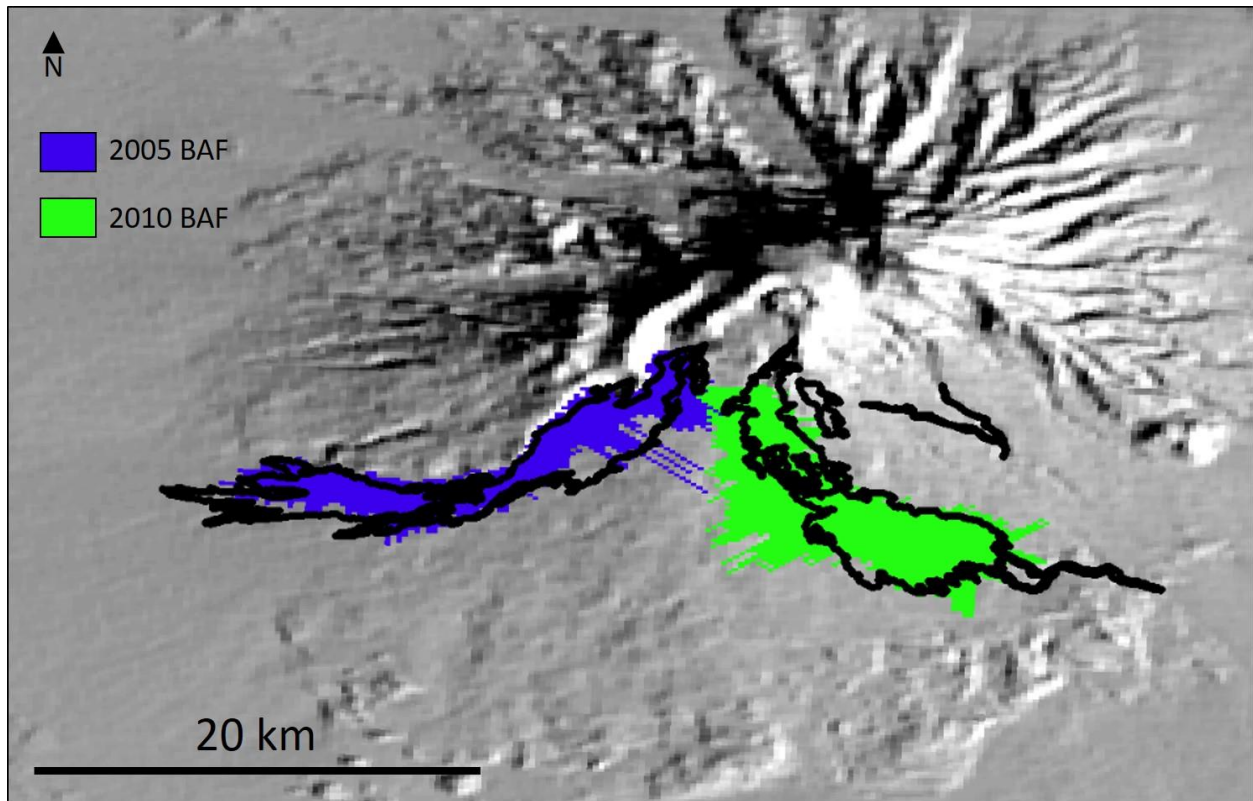
### **3.4.1 Application to LAHARZ model**

The LAHARZ model was developed for automated mapping of lahar-inundation hazard zones on volcanoes (Iverson et al., 1998; Schilling, 1998). Using a GIS platform and a Digital Elevation Model (DEM) along with user-specified volumes, the program maps out potential routes of lahar inundation zones. Widiwijayanti et al. (2009) assessed this model for the application to BAFs, and calibrated the two main model equations  $A=(0.05 \text{ to } 0.1)V^{2/3}$  and  $B=(35 \text{ to } 40)V^{2/3}$ , where  $A$  is cross-sectional area of inundation,  $B$  is planimetric area and  $V$  is deposit volume. The applied the model with their calibrated equations to Merapi and Soufrière Hills volcanoes to test against documented BAF deposits. Here, I applied this model to the Shiveluch 2005 and 2010 BAF deposits with the volumes specified in this chapter. The model was run in Matlab using the code written by Escobar-Wolf (personal communication). The study by Widiwijayanti et al. (2009) used 10 m and lidar-derived DEMs for the Montserrat model (the resolution for Merapi not defined but appears to be a similar resolution). In this study, a SRTM DEM was used, which has a pixel resolution of approximately 140 m in this area (manually measured in ArcMap). The lower

resolution DEM is a limitation in this study as the smaller-scale details may be omitted, but the surface hydrology raster that was produced in the LAHARZ model did show the stream networks that the BAFs traveled through. The parameters that provided the best fit to the two BAF deposit sizes and shapes are given in Table 10, and the areas produced using these parameters are given in Figure 37.

**Table 10. Best-fit parameters for the two BAF deposits used in the LAHARZ model.**

	<b>2005 BAF</b>	<b>2010 BAF</b>
Volume ( $V$ )	0.11 km <sup>3</sup>	0.28 km <sup>3</sup>
Cross-sectional area ( $A$ )	0.05	0.09
Planimetric area ( $B$ )	130	85



**Figure 37. The two best-fit LAHARZ simulated inundation results for the Shiveluch 2005 and 2010 BAF deposits on the SRTM DEM. The deposit outlines are shown in black.**

To get these best-fit simulated inundation models, different cross-sectional area and planimetric area values were required. The Widiwijayanti et al. (2009) study examined BAFs that were channelized, while the Shiveluch BAFs produced fan and channelized deposits. The simulated inundations for the fan areas for the Shiveluch deposits are not accurately portrayed, either creating cross-sectional widths too narrow or too wide. The simulated inundation results for the Shiveluch 2010 BAF deposit could not portray both the correct runout distance for the main deposit fan and the extended channelized deposit. For the simulated inundations that did manage to extend down the Kabeku River channel, the runout distance for the main deposit fan was overestimated by over 2.5 km.

It is likely that the inability of the model to incorporate the changes in topography that occurred due to the multiple pulses of deposition within the eruptions, reduces the applicability of this model to these large fan deposits. The Shiveluch BAFs are not channel confined (except for the distal 2010 BAF deposit section), and singular collapse pulses likely change the topography, and therefore, the subsequent direction of later flows. This model simulates the entire collapse volume descending through the flow paths in one event, using the topography present before the eruption began.

### **3.5 CONCLUSIONS**

The 27-28 February 2005 and 28 October 2010 BAF deposits were produced by two of the largest historical dome-collapse events on Earth. The deposit morphology is relatively well preserved, with 40% of the 2005 deposit surface eroded over the 4.5 years preceding the data used for this study. The deposits contain thicker areas composed of numerous onlapping surficial lobes outlined by lower density entrained clasts. Stratigraphic sections reveal that these are discontinuous stratigraphic units. Thicker areas of the deposits contain degassing structures and areas of syn- or immediately post-depositional shallow remobilization. Large blocks up to 12 m in length litter the surface of the deposits, having traveled considerable distances from the dome. Field and satellite data show evidence of pulsatory collapses, such as the presence of large composite lobate fans, discontinuous units, and variable surface block contents. We infer that the dome collapsed in multiple phases over the hours of each of the two eruptions, such that each produce a single large and composite deposit. This study shows how extensive large dome



collapses can be, and that the transition from open to channelized topography plays an important role in extending flow for a significant distance beyond the main area of deposition.

### **3.6 ACKNOWLEDGEMENTS**

Funding for this work was provided through NASA Earth and Space Science Fellowship (2014-15, 2015-16, 2016-17), a Henry Leighton Memorial Graduate Scholarship, University of Pittsburgh Hewlett International Grant, University of Pittsburgh International Studies Fund, and GSA (The Geological Society of America) Graduate Student Research Grant. The high-resolution QuickBird-02 and WorldView-02 data were provided by a DigitalGlobe Foundation Imagery Grant. Thank you to Rudiger Escobar-Wolf for the LAHARZ Matlab code, and help with the Shiveluch simulations. Thank you to Alison Graettinger and John Pallister for comments and discussions.

## **4.0 A COMPARISON OF COLUMN COLLAPSE-DERIVED PYROCLASTIC FLOW DEPOSITS ON MOUNT ST. HELENS VOLCANO, USA, AND DOME-COLLAPSE-DERIVED BLOCK-AND-ASH FLOWS ON SHIVELUCH VOLCANO, KAMCHATKA**

### **4.1 INTRODUCTION**

The term ‘pyroclastic density current’ encompasses the range of volcanic granular flows that are produced by collapse of a vertical ash column, pyroclastic material boiling over from a vent, remobilization of hot material accumulated around a vent, or lava-dome collapse. The final moments of deposition of a pyroclastic density current are recorded on the surface of the deposit. Morphological features formed on the surface of these deposits are often rapidly altered due to erosion or covered by subsequent deposits. High resolution aerial photography and orbital satellite data acquired prior to erosion offer a chance to investigate these surface features across deposit types. This paper discusses the similarities and contrasts between dome-derived BAF (BAF) deposits at Shiveluch volcano in Kamchatka, and column-collapse pyroclastic flow deposits at Mount St. Helens (MSH) volcano, WA, United States (Figure 38). These deposits were characterized using high-resolution aerial photograph, and orbital remote sensing data, before field studies to further examine the deposit surfaces.

Compared to other pyroclastic density current end members, relatively little is known about BAFs because of the “seemingly uniform and bland appearance” and rapid erosion of their deposits. (Schwarzkopf et al., 2005). Recently, new insights have come from studies undertaken shortly after dome collapse events (e.g., Charbonnier et al., 2012; Cronin et al., 2013; Komorowski, et al., 2013).

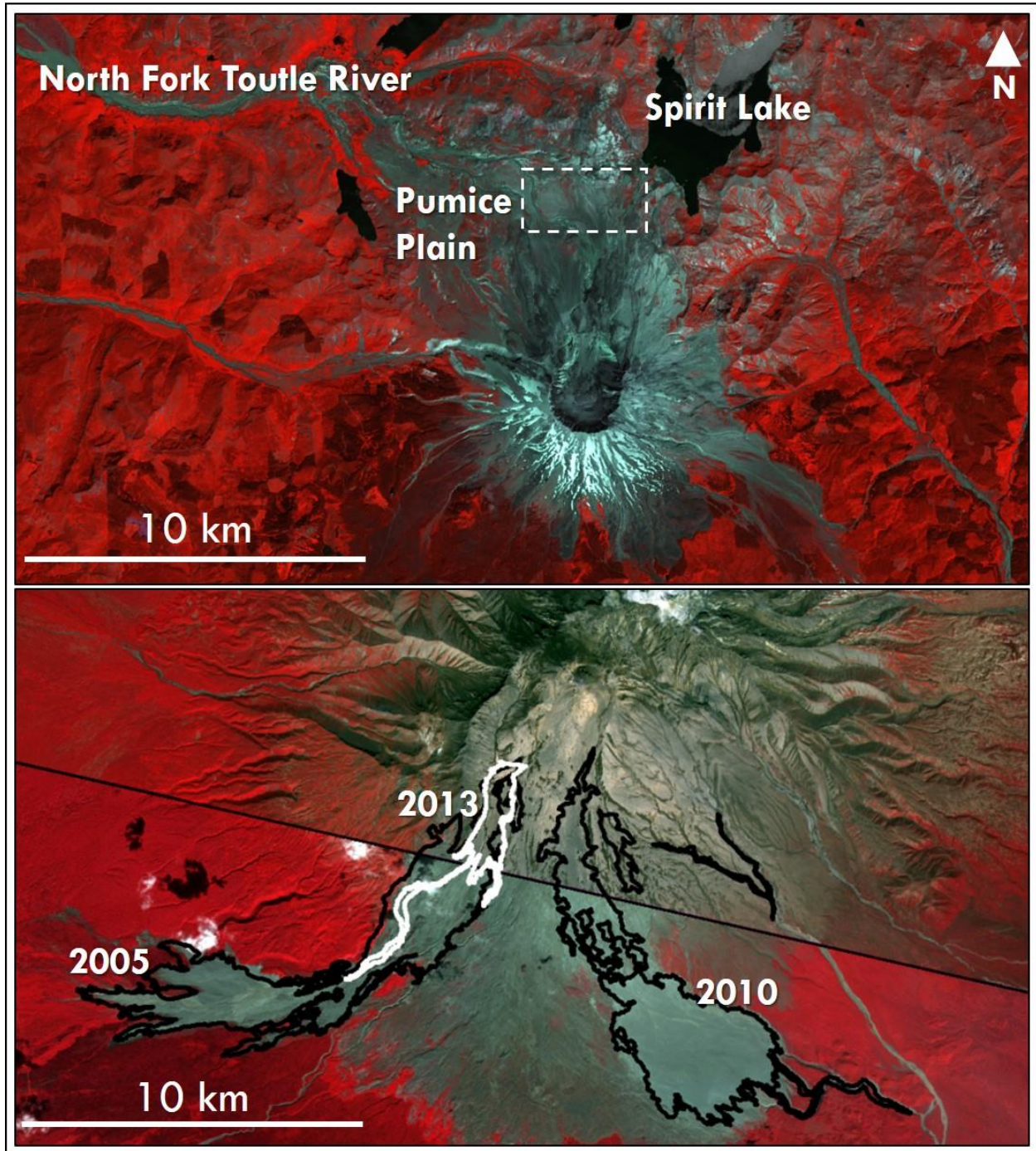


Figure 38. a) Mount St. Helens volcano (ASTER VNIR data acquired 08 August 2001. The white box outlines the area of the pumice plain area that is the focus for this study (see Figure 39 for more detail). False color image RGB: 3,2,1) and; b) Shiveluch volcano with the 2005 and 2010 main deposits with black outlines, and the 2013 deposit outlined in white. ASTER VNIR data acquired 06 June 2013. False color image RGB: 3,2,1).

Significantly more data from studies of column-collapse pyroclastic flows have resulted in sophisticated physical models for transportation and deposition of these deposits (e.g., Branney and Kokelaar, 2002; Burgisser & Bergantz, 2002; Neri et al., 2007; Cas et al., 2011). The eruption deposits of MSH that were produced during the 1980 eruption are some of the most comprehensively studied deposits in the world (e.g., Criswell, 1987; Rowley et al., 1985; Hoblitt, 1986; Brantley and Wait, 1988; Mackaman-Lofland et al., 2014). Because studies have focused on column-collapse events, a comparison to BAFs is expected to highlight their similarities and differences, and identify the relative importance of the vent/dome dynamics versus the flowage dynamics that occur during transportation. The different deposit types share similarities in flow and deposition, but they also have characteristics that reflect their distinct componentry and different initiation types. The results of this study indicate that these characteristics are reflected in the deposit surfaces. Aerial photographs taken by USGS in the initial years following the 1980 eruption were recently digitized and I used these digital images to map characteristics of the pyroclastic flows of the Pumice Plain that resulted from column collapse. Access to these early 1980 images allowed a new digital analysis of the Pumice Plain column collapse deposit area prior to the erosion of the surface features. High resolution satellite data with a comparable spatial resolution is available for the 2005, 2010, and 2013 Shiveluch BAF deposits that result from dome collapse events. The 2005 and 2010 deposit morphology and cross-sections have been analyzed using field and satellite data (Chapter two). These high-resolution datasets are used to compare and contrast the surface features of these deposits, which resulted from the two different eruption styles and initiation types.

The morphologies described for the MSH and Shiveluch deposits in this study are also recognized in pyroclastic density current systems from other volcanoes. In the following sub-

sections, I provide a compilation of these similar features and demonstrate how links between surface morphology and characteristics can be used to rapidly assess pyroclastic density current deposits from satellite and aerial data, and thereby provide information on changes in the flows produced through time.

#### **4.1.1 The 1980 eruption of Mount St. Helens**

The 18 May 1980 eruption of MSH began at 08:32 Pacific Daylight Time (P.D.T) with a magnitude 5.1 earthquake related to flank collapse, when three slide blocks travelling towards the north and then west to form a 2.5 km<sup>3</sup> hummocky debris avalanche deposit (e.g. Christiansen and Peterson, 1981; Glicken, 1996). The flank collapse depressurized the cryptodome, resulting in an explosive eruption that produced a lateral blast and devastated an area of 600 km<sup>2</sup>, and emplaced a dilute density current (“blast deposit” with a maximum thickness of approximately 1 m near the volcano (Lipman and Mullineaux, 1981). The afternoon of the 18 May 1980 eruption produced a series of column-collapse pumiceous pyroclastic flows (Christiansen and Peterson, 1981; Rowley et al., 1981). The pyroclastic flows traveled up to 8 km north in a fan-shaped (500 m wide, 1500 m long) succession of sheet, lobe, and toe deposits, that cover an area of 15.5 km<sup>2</sup> with a volume of 0.12 km<sup>3</sup> (Rowley et al., 1981). Individual flow unit thicknesses are 0.25-10 m with a total thickness of as much as 40 m (Rowley et al., 1981). Subsequent eruptions during the summer of 1980 produced pyroclastic flows by collapse of Plinian ash columns as well as by collapse or “boiling over” of low ash columns up to (<1 km above the vent) (Rowley et al., 1981; Hoblitt, 1986).

An eruption on 12 June commenced around 21:11 PDT and produced pyroclastic flows with a total volume of 0.01 km<sup>3</sup>, an extent of 8.3 km<sup>2</sup>, and a maximum thickness of 5-8 m. At least

two separate flows were emplaced onto the Pumice Plain during this eruption. Within these deposits, extensive remobilization of surface material occurred during and soon after these flows were emplaced, forming secondary pyroclastic flow deposits. Where these secondary flows broke away from the just-emplaced deposits arcuate linear scarps in the earlier flow deposits were produced (Rowley et al., 1981).

An eruption on 22 July eruption produced pyroclastic flows after 18:35 that were emplaced to a distance of 6.5 km north-northeast toward Spirit Lake. A subsequent eruption the same day (after 19:01) produced flows that extended 7 km north and northwest towards a large phreatic explosion pit that had formed in the 18 May deposits. The deposits formed an 800 m-wide sheet-like deposit, with the furthest extent nearly reaching the explosion pit. They have a volume of 0.006 km<sup>3</sup>, an aerial extent of ~4.8 km<sup>2</sup>, and maximum thicknesses of 2-4 m (thicker in the explosion pit area) (Rowley et al., 1981). Descriptions and a series of photographs of the 12 June and 22 July pyroclastic flows while in motion are given in Hoblitt (1986).

The pyroclastic flow deposits produced by successive eruptions during the summer of 1980 show trends of decreasing volumes and porosity, and (slightly) more mafic composition (Banks and Hoblitt, 1981; Christiansen and Peterson, 1981; Lipman and Mullineaux, 1981; Rowley et al., 1981; Kuntz et al., 1981). The deposits consist of pumice, dense dacite lithics, and ash, with poorer sorting and a higher block and lapilli to ash ratio with time (Rowley et al., 1981). The area that is underlain by debris avalanche and overlying pumiceous pyroclastic flows is called the 'Pumice Plain', which extends from the base of the MSH cone to Spirit Lake and the North Fork Toutle River, and has a surface slope of 2-3° (Rowley et al., 1981).

This paper focuses on the pyroclastic flow deposits emplaced on the afternoon of 18 May, and on 12 June, and 22 July. The 12 June and 22 July deposits comprise the upper units of the



Pumice Plain. The pyroclastic flow morphologies and surface characteristics of the Pumice Plain are distinct in aerial photographs from USGS aerial surveys of 8 July 1980 and 31 July 1980. Fieldwork and interpretation of these images led Rowley et al. (1981) to conclude that the difference between sheet and lobe morphologies are a result from variations in abundance of block-sized pumice, volumes of the flows, and underlying surface morphology. According to Rowley et al., deposits with a higher proportion of pumice blocks formed long, narrow lobes with high, steep margins, and resulted in a lower flow mobility and velocity.

#### **4.1.2 Shiveluch 2005, 2010, and 2013 eruptions**

The following Shiveluch dome collapse events and BAF deposits distributions are described in detail in Chapter one. Descriptions of the eruption events are provided in Appendix A, and the eruption parameters are summarized in Table 3 (Chapter one). The 2005 and 2010 BAF deposits were investigated in the field and are characterized using this data, and high resolution orbital satellite data, in Chapter two.

The Shiveluch 2005 BAF was emplaced during a 6.8-hour eruption on 27-28 February. The flow was produced by the gravitational collapse of the long-lived summit lava dome of Shiveluch and it traveled 17.8 km. The resulting 24.1 km<sup>2</sup> deposit terminates in a large pyroclastic fan located southwest of the volcano. The maximum width of the fan is 2.5 km.

The Shiveluch 2010 dome-collapse BAF deposit was emplaced on 27 October and it extends 19 km east from the source collapse scar on the dome. The bulk of the material was emplaced in a pyroclastic fan deposit with a maximum width of 4.1 km. A portion of flow continued an additional 5.4 km down the Kabeku River channel to the east from the fan.

I include information about the 26 July 2013 dome collapse because it produced a much smaller deposit because it is comparable in size to the MSH deposits. This deposit extends 11.6 km from the dome scar, and covers an area of 9.2 km<sup>2</sup>. It also produced a pyroclastic fan deposit and an additional channelized deposit.

The Shiveluch 2005 and 2010 block-and-ash-type PDC deposits are composed of poorly-sorted, fragmented dome material. The deposit surfaces and cross-sections are described in detail in Chapter two. Here, I briefly summarize key features of the eruptions and their deposits. The 2013 deposit is smaller than those of 2005 and 2010, and although I have not examined the deposit in the field, I assumed that it is composed of the same material, because of a similar dome-collapse initiation type (chapter one) and because the appearance in high-resolution images is similar to that of the larger flows.

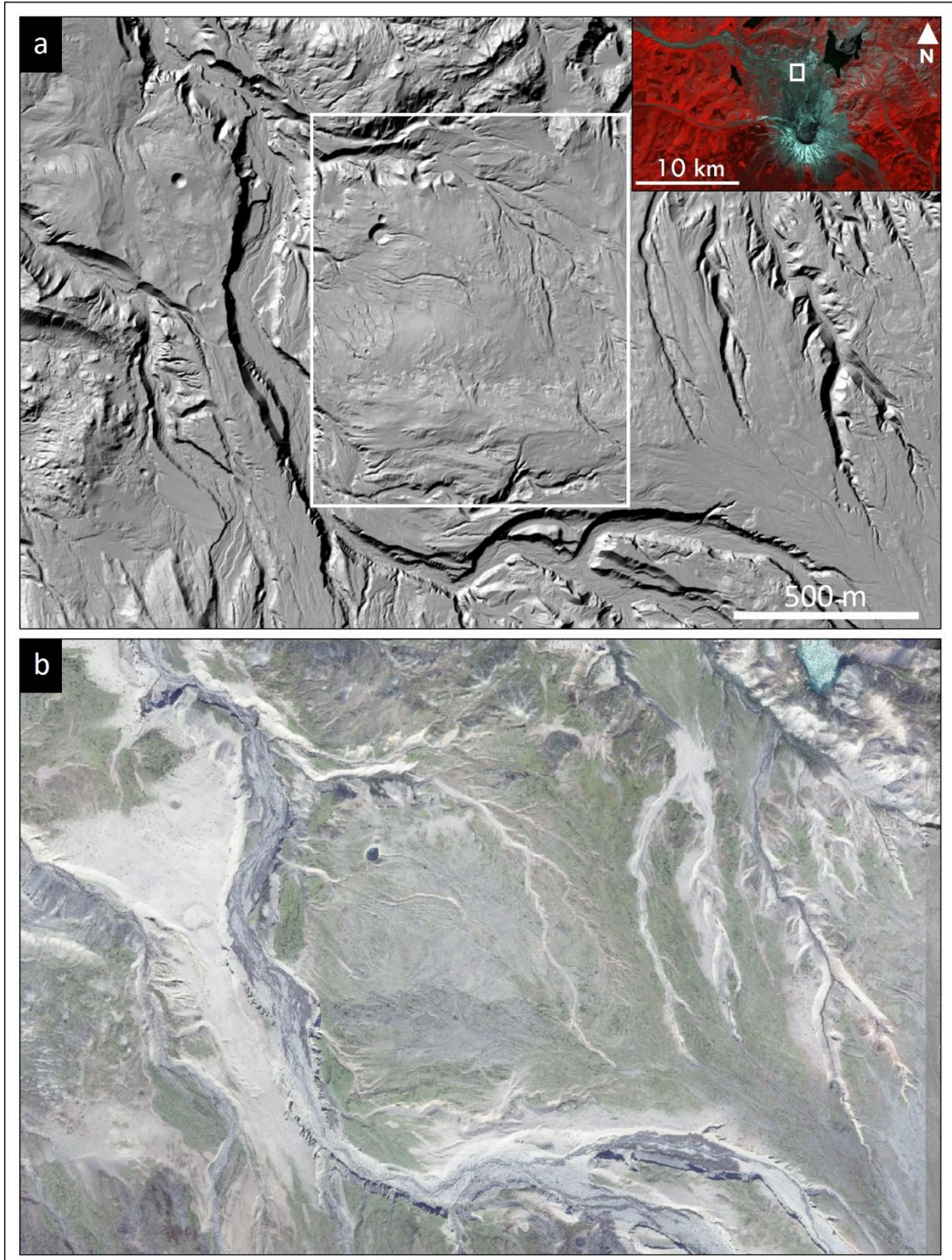
## **4.2 METHODS**

On the MSH Pumice Plain, the majority of the 1980 pyroclastic flow deposit surfaces are now altered or removed as a result of post-eruption lahar erosion and deposition and due to fluvial reworking of the loose pumiceous deposits. As noted previously, I re-mapped the pre-erosion deposit surfaces of the pyroclastic flow deposits using newly-digitized 1980 USGS aerial photographs to better characterize the surface morphology of the deposits. These high-resolution (approximate pixel size of 20 cm) photographs were taken on 7 July 1980 and 31 July 1980. They were manually geolocated using a bare-earth 1-m-resolution lidar survey that was acquired on 16-20 September 2009 (Mosbrucker, A.R., 2014). Elevation profiles were compiled using this lidar survey in the ESRI ArcGIS platform. A section of the pumice plain containing mostly 18 May

deposit, and minor 12 June deposit, surfaces that have been preserved between erosional gullies (Figure 39). This area was visited in the field in 2016 to investigate lobate morphologies that were characterized using aerial photographs, and to compare flow fronts to those seen on Shiveluch.

Two large 27-28 February 2005 and 27 October 2010 BAF deposits, and a smaller deposit that was emplaced during the dome collapse event on 26 July 2013 at Shiveluch were imaged by high-resolution orbital satellite images (Table 11). A scene acquired by the QuickBird-02 satellite sensor (0.65 m pixel resolution) on 27 August 2013 was used to analyze the 2005 BAF deposit, and scene acquired by the World-View-02 satellite sensor (0.46 m pixel resolution) on 29 September 2010 was used to analyze the 2010 and 2013 deposits.

Deposit samples were collected and were prior to this research. The MSH sample data is from Pallister et al. (2017), and the Shiveluch samples were previously collected and processed by A. Belousov and M. Belousova.



**Figure 39.** The preserved area of the pumice plain pyroclastic flow deposits are shown in the white box (in a and within inset) in a) the 2009 lidar data; and b) an OrbView-3 image (Table 11) acquired on 5 October 2004. Erosional channels are visible throughout the pumice plain.

**Table 11. High resolution data used in this study with technical parameters.**

<b>Satellite sensor</b>	<b>Acquisition Date</b>	<b>Spectral Range (nm)</b>	<b>Spatial Resolution /swath width (at nadir)</b>	<b>Deposit imaged</b>
WorldView-02	12-Mar-05	Panchromatic 450-800	0.46 m/16.4 km	Shiveluch 2005 BAF deposits
QuickBird-02	27-Aug-13	Panchromatic 450-900	0.65 m/ 16.8 Km	Shiveluch 2010 and 2013 BAF deposits
OrbView-3	5-Oct-04	MS1: Blue 450-520	4 m*/8 km	Pumice Plain, Mount St. Helens pyroclastic flow deposits
		MS2: Green 520-600	4 m*	
		MS3: Red 625-695	4 m *	

\* Pan-sharpened to 0.2-0.3 m pixel resolution

### 4.3 RESULTS

The Shiveluch deposits are remarkable due to their size (>24 km<sup>2</sup>), extent of transport (>19 km from the source dome), and by the long distance that large dome blocks were transported (blocks that exceed 6-m-diameter traveled >12 km from the dome). In addition, they lack breadcrust bombs and peripheral forest damage indicates that they were accompanied by dilute pyroclastic surges. My remote sensing and field data indicate sequential emplacement of flow lobes as a result of regressive dome collapse eruption, and are described in detail in Chapter two. The Mount St. Helens pumice plain deposits have been newly interpreted using aerial photographs (Figure 40) for the purpose of comparing the two deposit types. Here, I compare the surface morphology of the Shiveluch and MSH column collapse deposits and to features in the published literature.

As describe below, I propose that the two different eruption styles - column collapse or “boiling over” from the vent at MSH, and dome collapse at Shiveluch, both produce unsteady flows that emplace deposits with varying morphologies and componentry. These factors vary with distance from the vent, and laterally across the deposits. I propose that the variation in surface morphology discussed in this chapter results mainly from changing flowage dynamics, and that changes in rock components that form the flows results from both changing conditions at the dome or vent, as well as from changes in flowage dynamics.



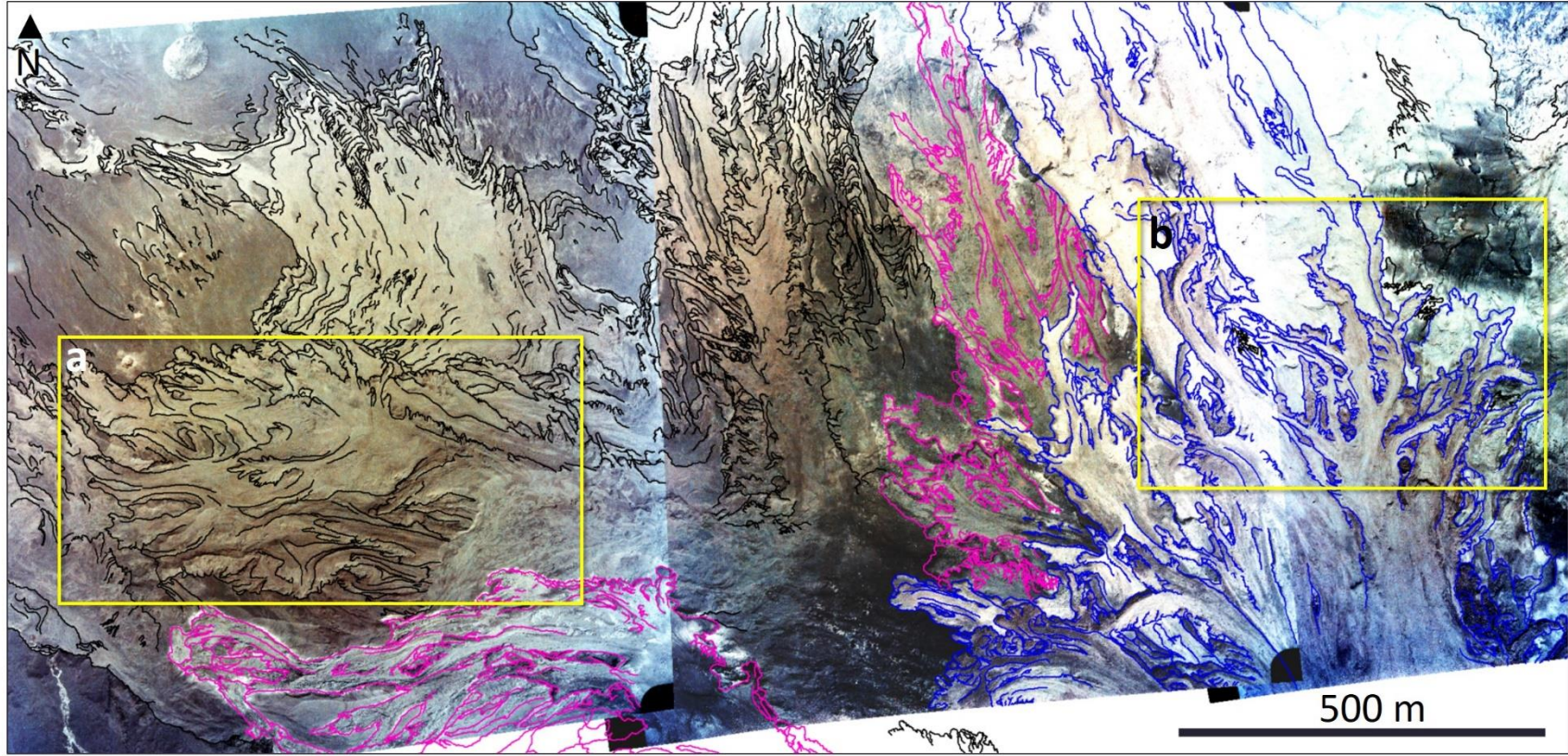


Figure 40. The Mount. St. Helens Pumice Plain shown in three overlapping aerial photographs. The 18 May 1980 (black outlines), 12 June 1980 (pink outlines), and 22 July 1980 (blue outlines) delineate pyroclastic flow deposits. Yellow boxes indicate areas shown in Figure 44.

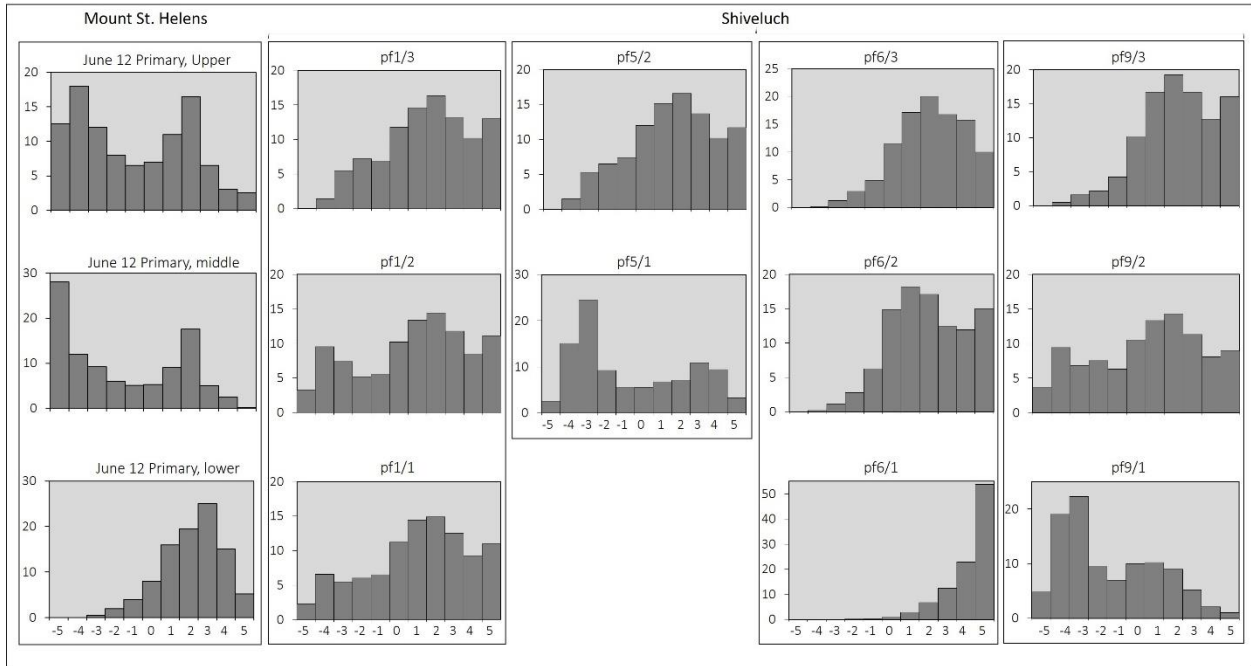
### 4.3.1 Componentry and composition

The Shiveluch BAFs are composed of fragmented dense andesite dome material, and accidental lithic clasts from the underlying 1964 pyroclastic flow deposits. Large blocks as large as 12 m in diameter were transported with the flows and are present on the surfaces of the BAF deposits. The dome is composed of 60.4-63.9 wt.% SiO<sub>2</sub> silicic andesite (Table 2, Chapter one). The silica content of the dome has increased over the temporal development of the dome.

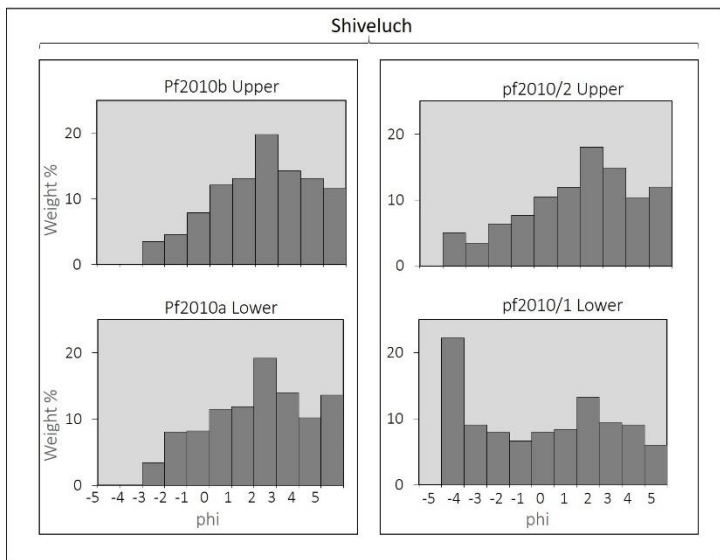
The Pumice Plain deposits are composed of poorly sorted ash (pumice, glass shards, and fragmented phenocrysts), pumice (white dacitic with 63-64 wt.% SiO<sub>2</sub> and denser grey andesitic pumice with 61-62 wt.% SiO<sub>2</sub>), and lithic clasts (dense dacite) (Rowley et al., 1981; Criswel, 1987). Through time, the eruptions produced smaller pyroclastic flow volumes with poorer sorting, larger particle sizes, and lower porosity pumice clasts (Kuntz et al., 1981). The coarsest clasts are concentrated in lateral levees and lobe margins.

Because they are more commonly exposed at the surface, in this image analysis data is included for the upper units of the PDCs from MSH and Shiveluch (Figure 41) that are most likely to contribute most to the surface morphology that we observe in the remote sensing data. Relative to the upper units of the 12 June 1980 MSH deposit, the Shiveluch 2005 and 2010 upper units all have a lower proportion (<50%) of lapilli-sized clasts (-2 to -6 phi, or 4 to 64 mm) (Figure 42). In contrast, the MSH 12 June upper sample has a higher proportion of lapilli (75%), due to a concentration of pumice lapilli. Grain-size data is not available for the 2013 Shiveluch BAF deposit; however, satellite images shows a concentration of coarser blocks along some of the lobe boundaries. The componentry data presented here is based on only brief reconnaissance field studies at Shiveluch and MSH. Although adequate to provide first-order ground truth for my

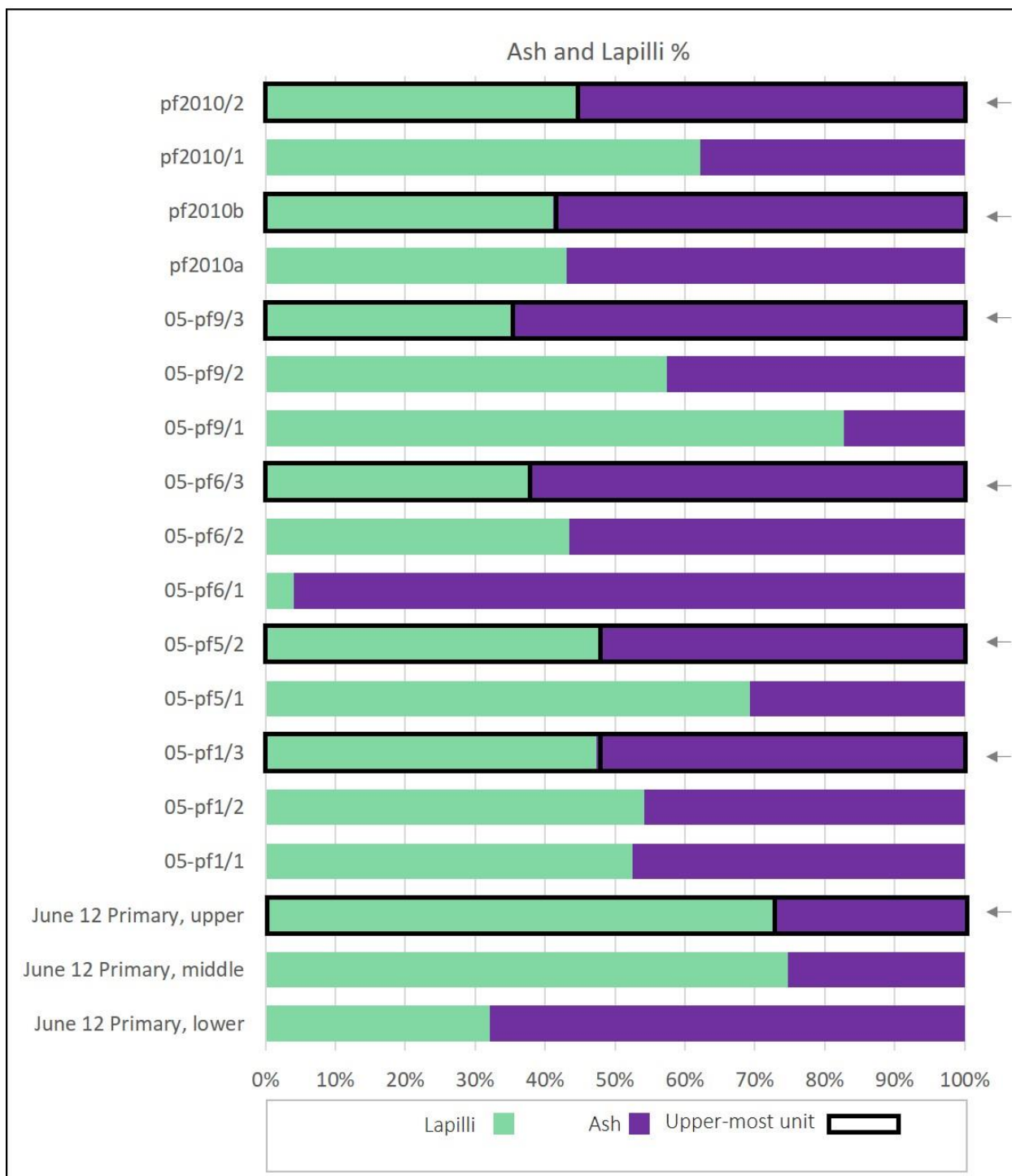
remote sensing interpretations, more detailed componentry analyses would likely improve interpretation of details in the surface morphology of the deposits.



**Figure 41. Componentry plots for the Mount St. Helens 12 June pyroclastic flow deposit, and the Shiveluch 2005 and 2010 deposit. Plot titles indicate original sample names.**



**Figure 41. continued.**



**Figure 42. Abundance of ash and lapilli in the Shiveluch 2005 (-05-pf) and 2010 (pf2010) BAFs (Chapter two); b) and Mount St. Helens June 12 pyroclastic flow deposits (Pallister et al.,2017). The upper-most units are outlined and indicated by arrows.**

### 4.3.2 Aerial Deposit Distributions

The Shiveluch and MSH Pumice Plain deposits have a range of areal distributions (Table 12). The Shiveluch BAFs traveled over a greater distance and elevation before producing fan deposits. They traveled maximum distances of 17.8 and 19.0 km and descended 2.4 and 2.2 km in 2005 and 2010, respectively. The 2013 Shiveluch deposit extends as much as 11.6 km from the dome, and 4.6 km of this extent is as a channelized flow beyond the main fan. The MSH pyroclastic flows traveled as much as 8 km from the vent, and descended up to 1.7 km from the crater floor and over the Pumice Plain.

**Table 12. Shiveluch 2005, 2010, and 2013; and Mount St. Helens (MSH) 18 May, 12 June, and 12 July deposit distributions.**

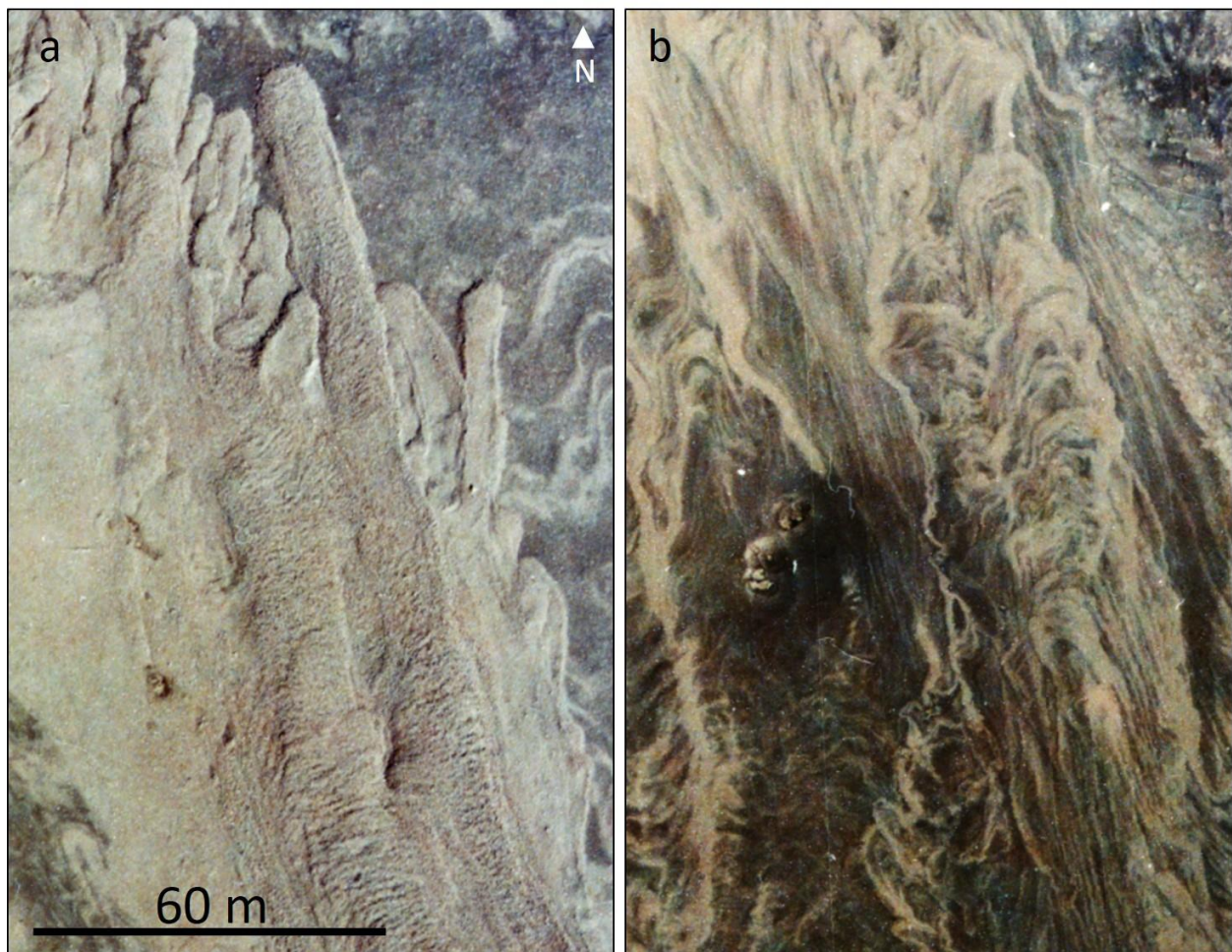
Deposit	Flow initiation	Max. Runout (km)	Deposit Area (km <sup>2</sup> )	Elevation change (km)	Max H/L	Deposit Volume (km <sup>3</sup> )	Reference
Shiveluch 2005	Dome collapse	17.8	24.1	2.4	0.13	0.11*	Shevchenko et al., 2015; Krippner et al. (in Prep.a)
2010	Dome collapse	19	22.3	2.2	0.16	0.28*	Dvigalo et al., 2011; Shevchenko et al., 2015; Krippner et al. (in Prep.a)
2013	Dome collapse	11.6	3.5	2.07	0.23	N/A	Krippner et al. (in Prep.a)
MSH 18 May	Column collapse	8	15.5			0.12	Rowley et al., 1981
12 June	Column collapse	7.5	8.3			0.01	Rowley et al., 1981
12 July	Column collapse from 400-800 m	7	4.8	1.2-1.7	0.26	0.006	Rowley et al., 1981; Hoblitt, 1986

### 4.3.3 Sheet-like deposits

Sheet-like deposits at both volcanoes fan out over a broad areas and contrast with the smaller lobate units that are morphologically diverse. The lowermost visible 18 May pyroclastic



flow deposits at MSH are sheet-like with lower-relief or smooth deposit surface (Figure 43). Surfaces of these flows are marked with flow bands – multiple linear and curvilinear bands that are lighter in color in aerial photographs. Higher-relief lobate deposits overlie these sheet-like deposits. The 22 July 1980 MSH lobate deposits have an underlying section made up of small lobes near the perimeter of the deposit, but they generally lack the distinctive morphological features of the overlying lobes that were deposited later in the depositional sequence.



**Figure 43. Differing degrees of surface relief in the 18 May deposits: a) thicker lobate deposits with shadows visible in the aerial images due to the thickness of the lobes; b) low-relief surface morphologies formed by thinner deposit in the darker areas of the 18 May deposits. Photographs from the USGS 31 July 1980 survey.**



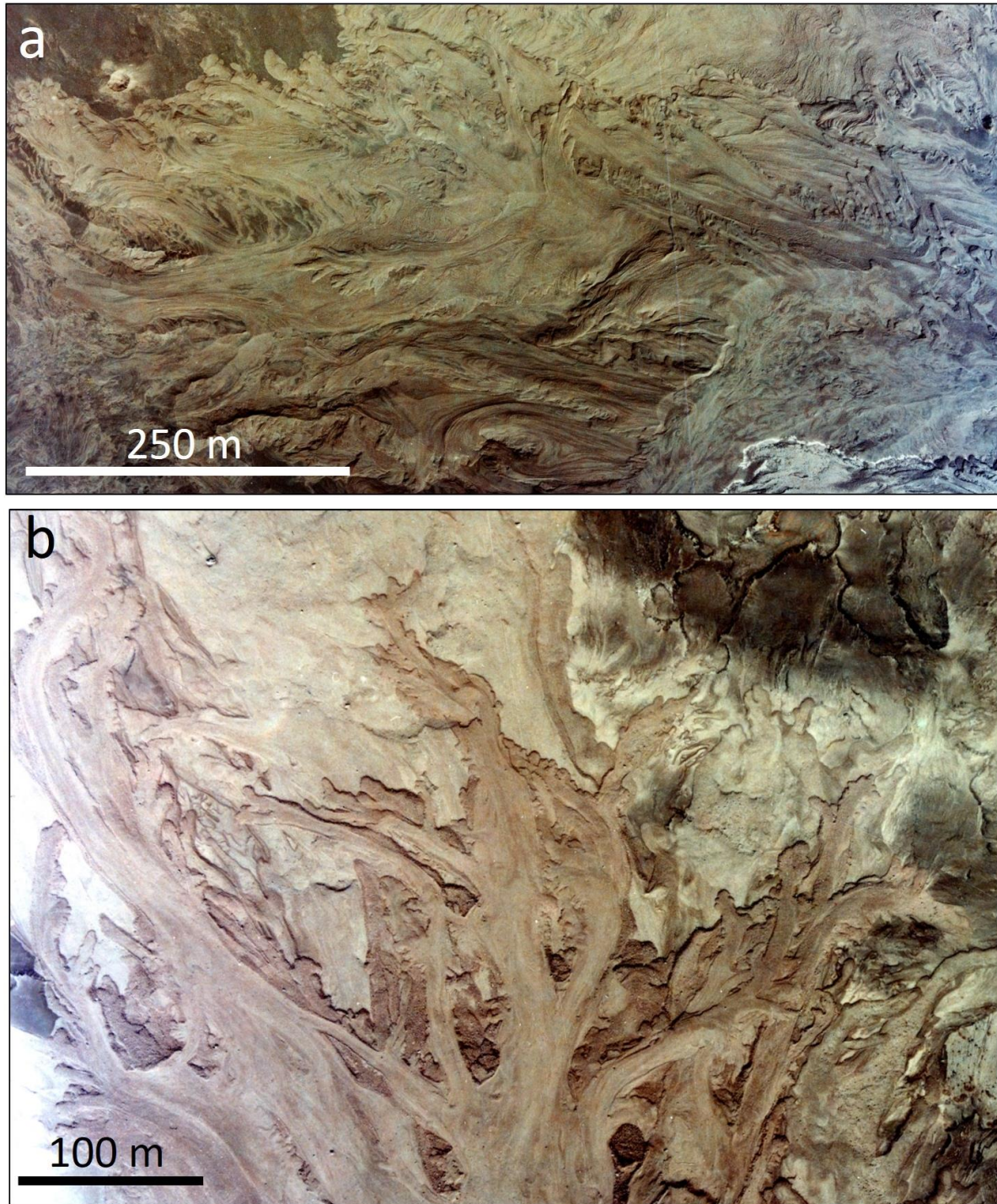
The Shiveluch 2005 and 2010 deposits both contain areas that were deposited in a sheet-like manner, spreading out to form a relatively uniform surface that lacks distinct lobate morphologies. On the sheet-like deposit surfaces the morphological features are low-relief banding (Figure 43b), in contrast to the lobate deposits with ridge and furrow morphologies (Figure 43a), and channel and levee features. As at MSH, the sheet-like deposits also underlie the areas with more distinct morphological features.

The distal 2 km of the Shiveluch 2013 deposit has a lower surface relief with feathery lobes and faint lineations. Emplaced later in the eruption episode is the uppermost section (closer to the dome) of the 2013 deposit. This area contains well-developed channel and levee systems, and lobate morphologies, where coarser clasts are concentrated along the lateral edges. These are discussed further in section 4.3.5.

#### **4.3.4 Composite lobate deposits**

The Shiveluch and MSH deposits both contain sets of stacked lobes and individual deposit pulses where deposition occurred sequentially in the same location to build up a thicker deposit. The Pumice Plain contains two main composite lobate features, one within the 18 May deposits, and the other within the 22 July deposits. The 18 May composite feature is 580- to 780 m-long and contains a range of lobate morphologies (Figure 44a). Stratigraphically, the lowermost lobes tend to have cats-paw or lobe and cleft terminations, while the upper lobes tend to be more elongate and are draped over underlying topography. The southeastern section is eroded or remobilized and covered by 12 June deposits. The 22 July deposit composite lobate feature (Figure 44b) is approximately 680 x 700 m in area. The lobes within this feature are more elongate and distinct than the in the 18 May deposit and they overlap each other. The long lobes have smaller lobes or

toes developed along the lateral edges. Some underlying lobes and smaller lateral lobes have a higher concentration of coarser clasts. Levees are present in some areas.



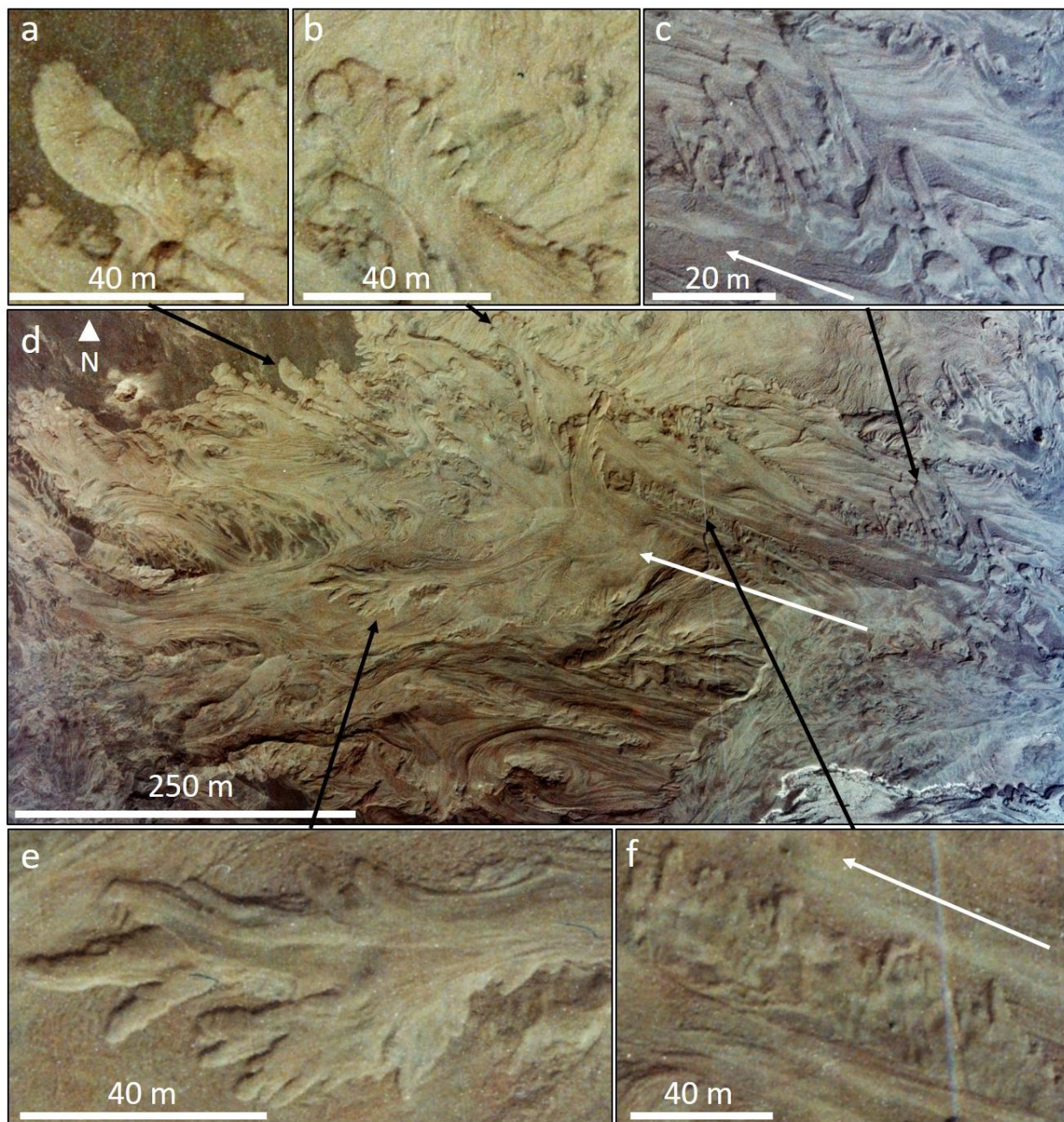
**Figure 44.** Composite lobate features in the: a) 18 May 1980 deposit; and b) 12 June 1980 deposits on the Pumice Plain. Locations given in Figure 40.

The Shiveluch composite deposits are described in Chapter two. Individual flow pulse-boundaries are evident within the Shiveluch deposits due to the low-density of accidental material that outlines each flow pulse and shows in detail the sequence of deposition. The composite deposits on Shiveluch are comparable in size, but are more elongate than the Pumice Plain deposits, with dimensions of as much as 750 x 2000 m. The flow boundaries are less pronounced than their Pumice Plain analogues and they have tapering, irregular flow fronts. They also contain levee and channel formations.

#### **4.3.5 Lobate morphologies**

The deposits on the MSH Pumice Plain contain lobes with different degrees of relief. Higher relief lobate features display shadowing in the images, and have distinct boundaries in the imagery. Thicker lobes with higher relief have steep flow fronts that are clearly visible in the field. The lobate morphologies are much more diverse on the MSH Pumice Plain than in the Shiveluch deposits. They include overlapping, elongate lobes with some levee and channel development; stacked sets of elongate lobes visible along the lateral edges of deposits; lobes with numerous rounded toes (Figure 45).



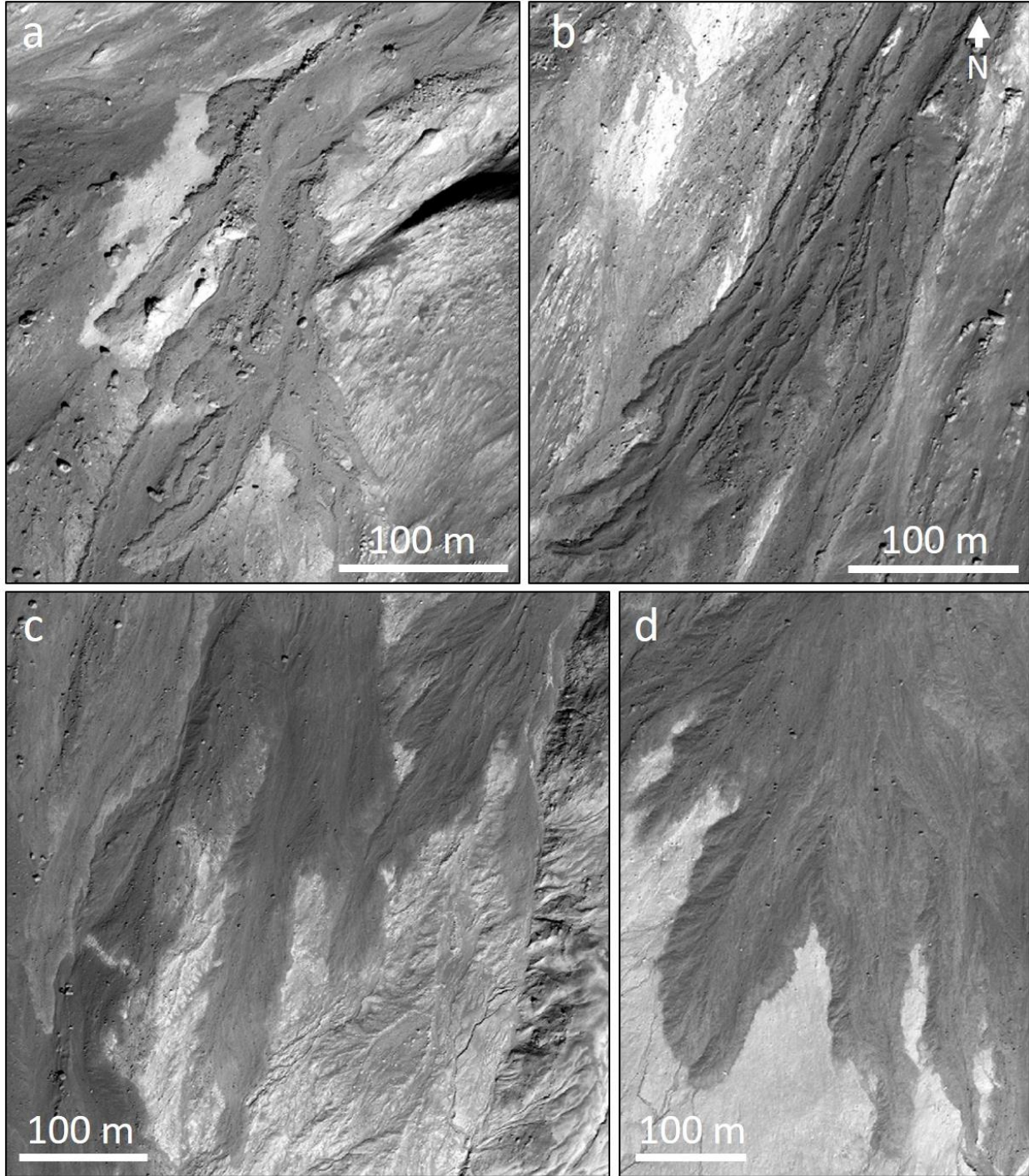


**Figure 45. Lobate morphologies in the 18 May 1980 pyroclastic flow deposits with white arrows showing flow direction: a) lobe set with stacking of deposit material in the same place and each subsequent pulse is shorter; b) cats-paw or lobe and cleft morphology; c) stacked sets of narrow, elongate lobes forming off the side of a flow; d) entire section of stacked lobes with black arrows indicating feature locations; e) elongate overlapping lobes originating from the same feeder channel; f) sheet-like deposit with poorly-defined lobate terminations perpendicular to the main flow direction. Images are from the 31 July aerial survey.**

In contrast, the Shiveluch deposits have more diffuse and tapering (gradually decreasing in thickness) flow boundaries. It would be difficult to distinguish flow boundaries in the field without the presence of bands of low-density clasts and wood fragments that were emplaced along them. The Shiveluch flows' irregular boundaries also contrast with the smooth boundaries of the Pumice Plain flows, and they do not form elongate singular lobes with sharp flow fronts. Distal deposits at the end of the main 2010 Shiveluch deposit fan contain low-relief elongate lobes with few surface blocks and feathery edges. Lobate terminations are also present in the remobilized 2005 and 2010 Shiveluch deposit. These terminations are bulbous or rounded in shape, similar to terminations of the primary lobes.

The Shiveluch 2013 deposit contains lobes with both feathery and sharp lobate terminations. The lobes with sharp terminations (Figure 46a-b) contain well-developed channel and levee structures and a higher concentration of coarser blocks along the levees and flow fronts. The feathery/diffuse flow boundaries occur further downstream in the deposit and have few surface blocks. They are similar in these respects to the 2010 deposit (Figure 46c-d). Multiple sets of lobes occur along different intervals of the deposit.



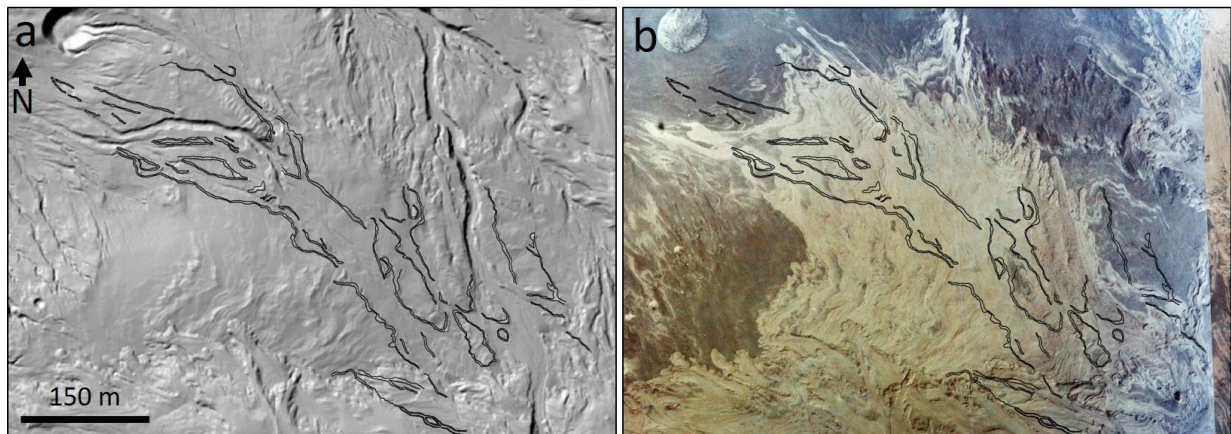


**Figure 46. Lobes of the 26 July 2013 Shiveluch BAF deposits, a) sharp terminations with coarser clasts concentrated along the flow boundaries 620 m from the dome; b) well-defined levees and sharp flow boundaries 1070 m from the dome; c) diffuse flow boundaries 1600-1800 m from the dome, d) diffuse flow boundaries 3150 m from the dome.**

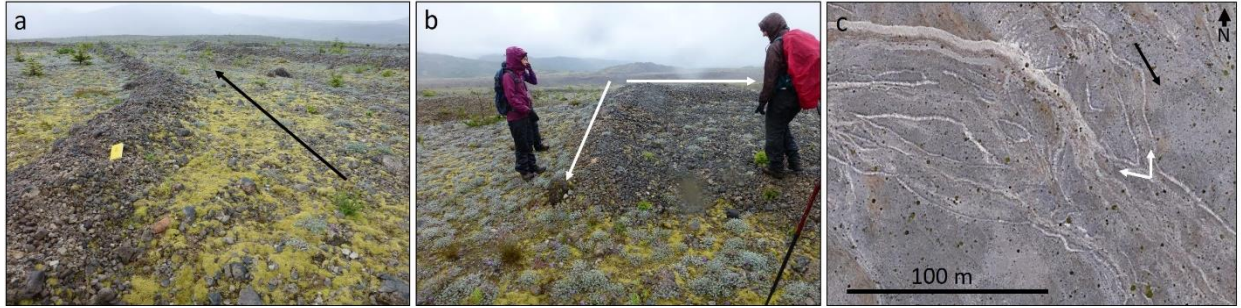


#### 4.3.6 Primary and secondary levees and channels

Channel and levee systems form on both pyroclastic flow and BAF deposit types. In both deposit types at Shiveluch and MSH, they occur within areas of overlapping lobes within these composite deposits. Levees on the MSH Pumice Plain deposits were described by Rowley et al. (1981) and Wilson and Head (1981). The MSH Pumice Plain surface also contains a system of levees that do not correlate with pyroclastic flow deposits (Figure 47), but instead are composed of blocks derived from the underlying deposit (Figure 48). In the field, they look nearly identical to primary pyroclastic flow levees and they vary in width to as much as 2 m-wide. They occur as straight or sinuous linear levees, or as V-shaped structures where redirected around a topographic high (Figure 10). The levees are not present in aerial photographs taken on 27 July 1981, but they are present in an aerial photograph taken on 23 March 1982, indicating that they formed between these times, likely by floods that swept the Pumice Plain surface in this area.



**Figure 47. Secondary levees at MSH. a) As mapped in a 2009 lidar survey image and; b) the same location with levee locations overlain on a USGS 31 July 1980 aerial photograph.**



**Figure 48. Secondary levees at MSH with locations shown by the black (a) and white (b) arrows on the Google Earth image in c.**

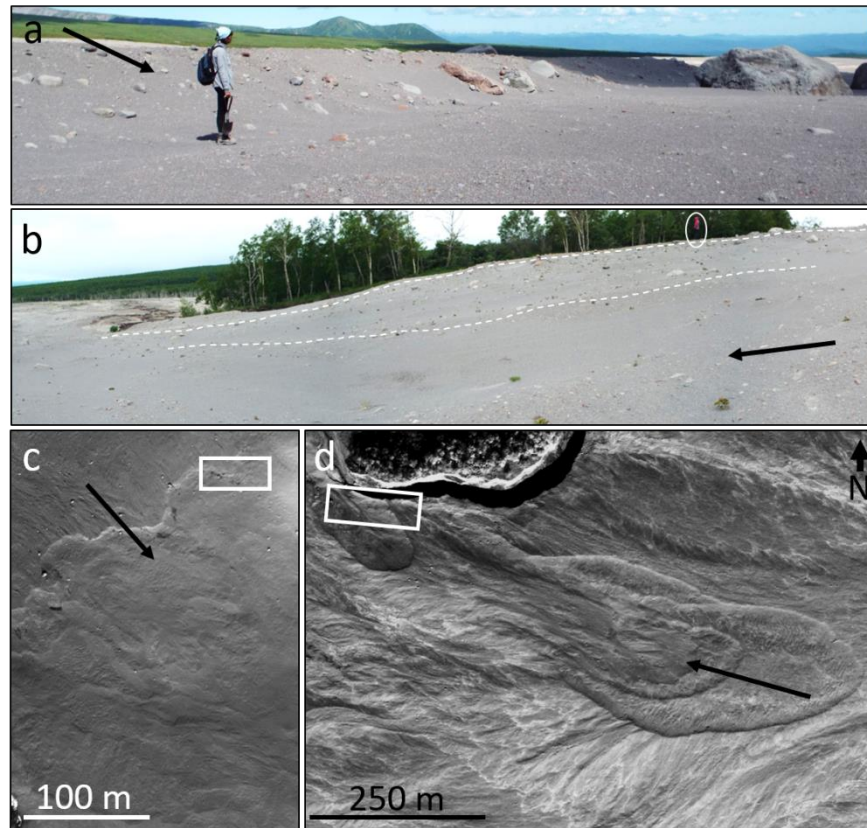
#### **4.3.7 Shallow deposit remobilization**

The 12 June MSH deposit contains large areas with scalloped scarps and remobilized material extending from the scarps (Figure 49). These formed soon after deposition and are described by Rowley et al., 1981.

Remobilized areas in the 2005 and 2010 Shiveluch deposits are described in Chapter two. Headwalls of these remobilized areas occur as arcuate and curvilinear scarps, where they formed in thicker composite lobate areas and sheet-like areas (Figure 50a, c). Arcuate scarps are observed at the upslope edge of the remobilized areas in the thicker composite lobate features (Figure 50b, d). The 12 June MSH scarps are more rounded (scalloped) than the scarps in the Shiveluch deposits.



**Figure 49.** Scalloped remobilization scarp in the 12 June 1980 pyroclastic deposit on the Pumice Plain. Area is show in the white box in (b), which is an aerial photograph taken during a USGS survey on 8 July 1980. Black arrows indicate flow direction.



**Figure 50.** Remobilization scarps in the Shiveluch deposits: a) scarp headwall of a curvilinear scarp (area indicated in the white box shown in c) in the northern section of the 2010 deposit; b) the sidewall of the arcuate scarp (area indicated in the white box in d) with person (in white circle) for scale; c) bench topography above the curvilinear scarp in the 2010 deposit fan; d) nested arcuate scarps in the 2005 deposit

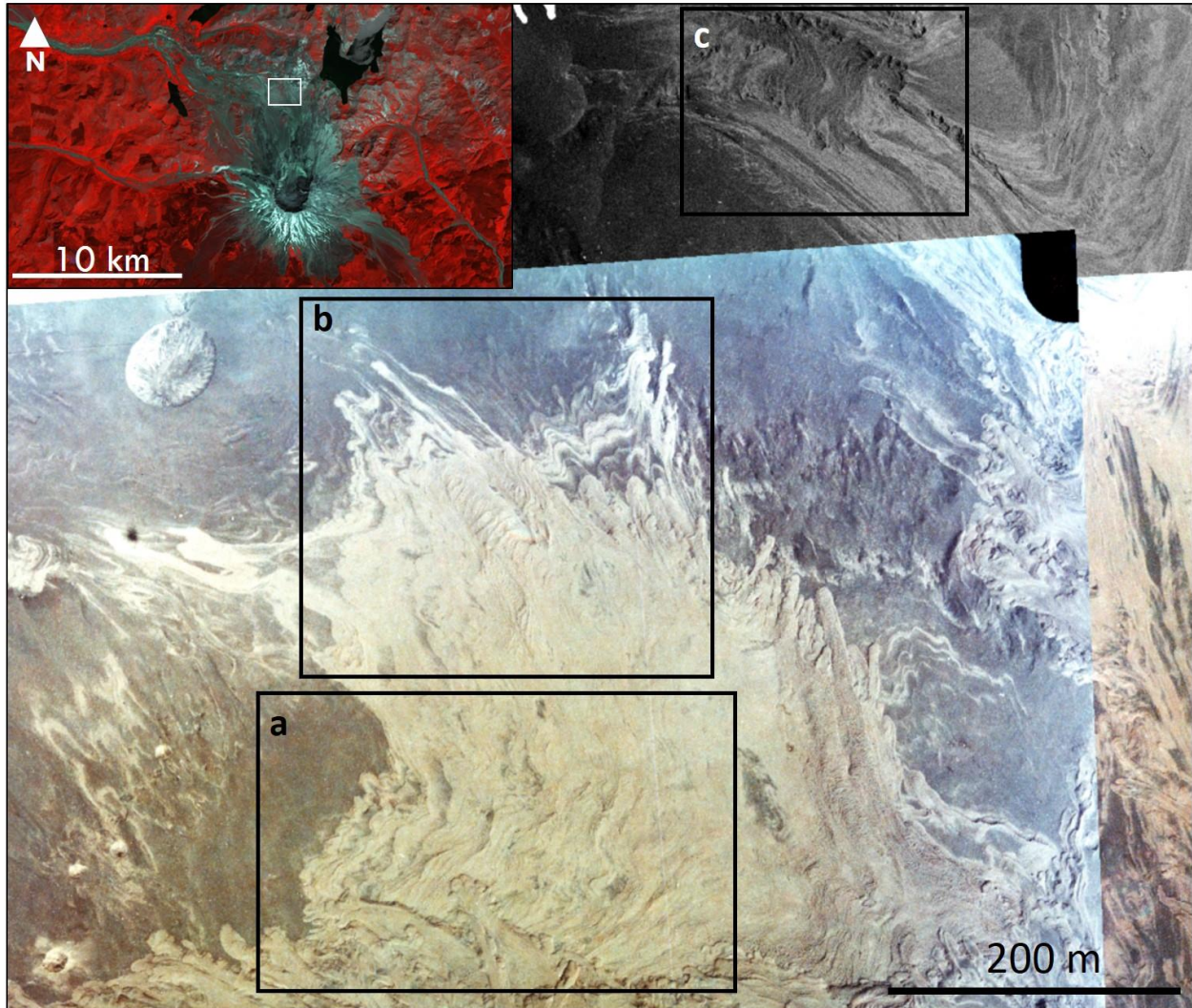
#### 4.3.8 Ridges

The 18 May MSH deposits contain thinner sheet-like deposits that overlie darker, smooth, extensive sheet-like deposits, which formed earlier in the day (Figure 51). These smaller-volume deposits underlie the 18 May lobate deposits that were emplaced immediately to the south. They contain several areas in which ridges perpendicular to the flow direction are visible on the surface. The most extensive set of these ridges are shown in Figure 52, where they are observed over a minimum area of 250 x 130 m (they may extend further in the subsurface, beneath overlying lobate deposits). Lidar images show that the ridges elevated above the deposit surface and many are coupled with depressions forming an elongate, parallel, ridge-and-trough pattern. A section to the north of this area and within this same sheet flow deposit, contains three narrow elongate areas with surface ridges (Figure 53). These areas also have ridge-and-trough features that occur perpendicular to flow direction. In Figure 53, the section with line A-A' is a part of the same sheet-like deposit as the ridged area in Figure 52. Lines B-B' and C-C' are within the section and immediately underlie this sheet deposit.

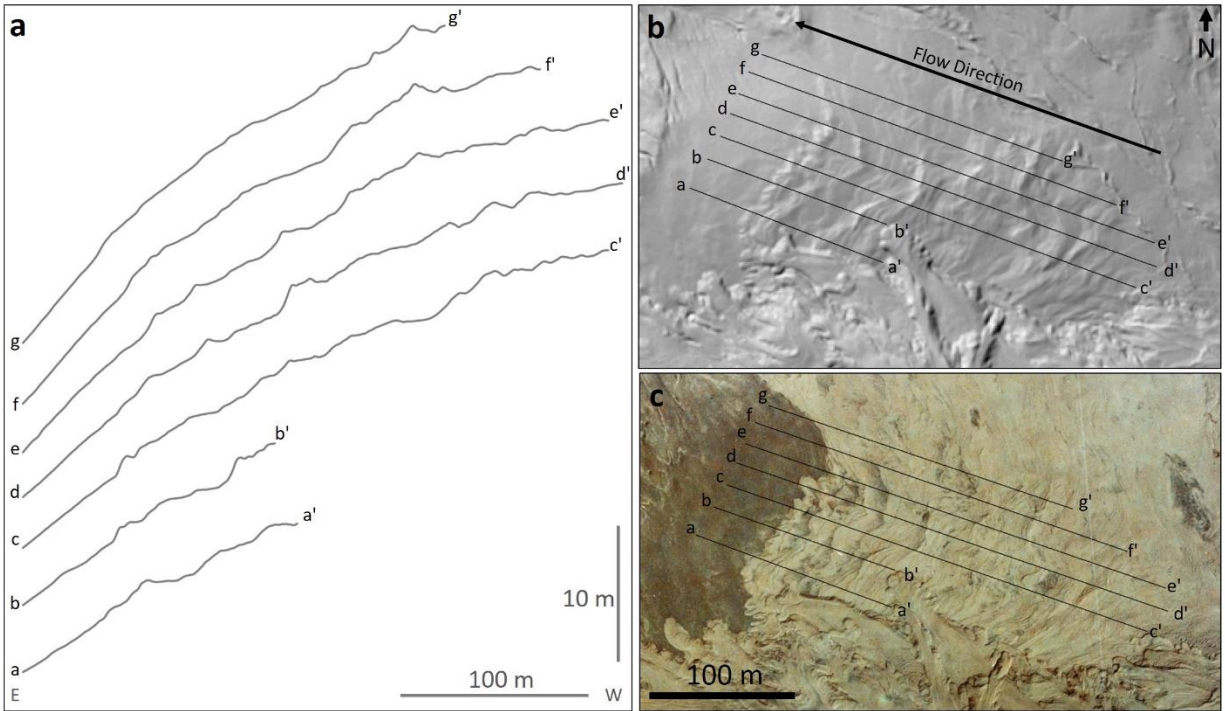
In the northern area of the 18 May deposits (Figure 51) is an elongate lobe that contains rounded, parallel, perpendicular to flow ridges with smaller lobe toes along the outer edges (Figure 54). They also show evidence of being compressional in nature, because lidar data show the same ridge-and-trough morphology. Here, the center of each ridge is convex downstream to the direction of flow. They are rounded on both outer edges, with some smaller toes present. There are several



of these features emplaced in the same location so that multiple toes are visible around the lateral lobe boundaries due to the stacked deposits.

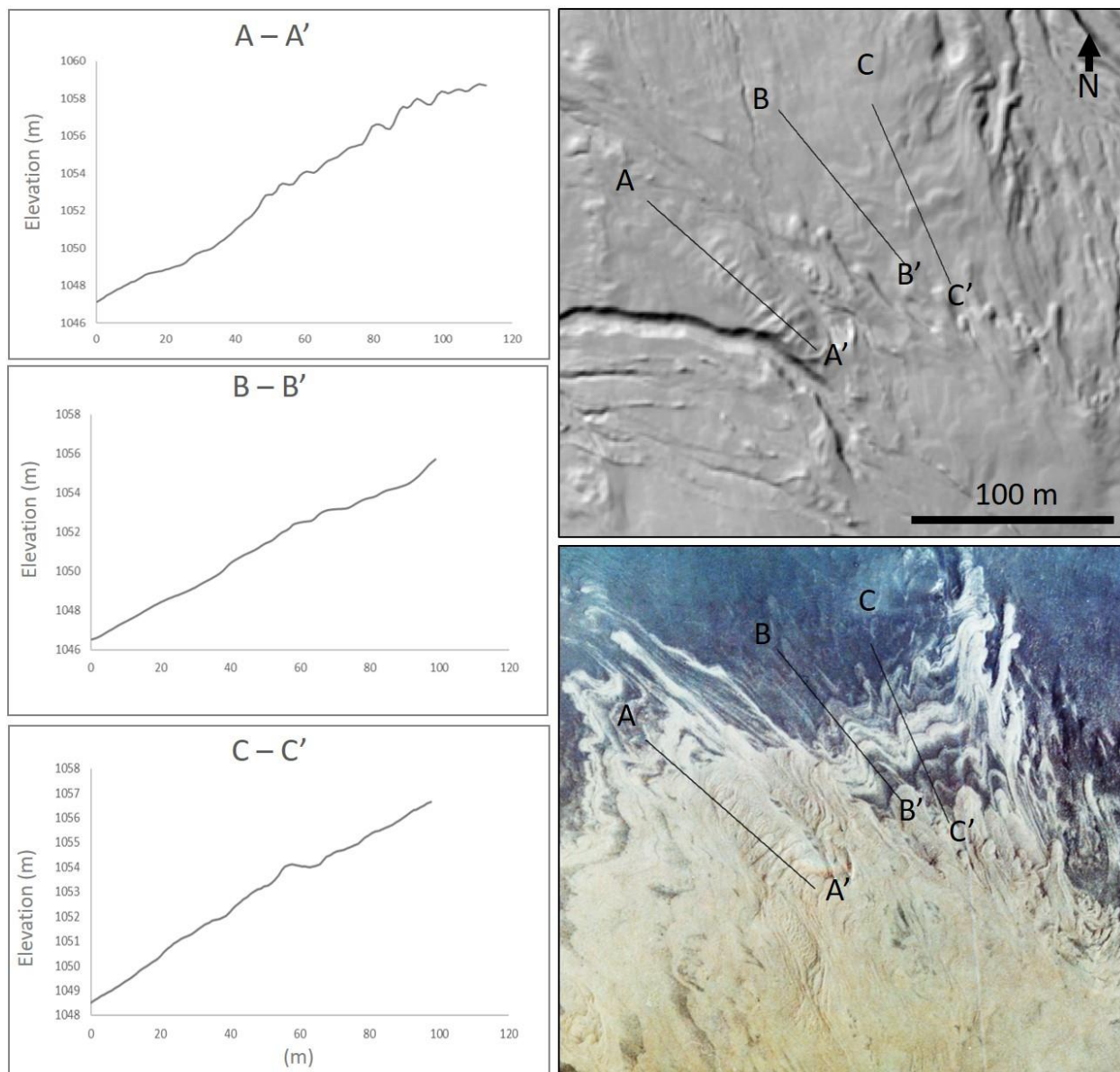


**Figure 51.** The MSH 18 May sheet-like pyroclastic flow deposits that contain the surface ridge-and-trough features shown in more detail in: a) Figure 52; b) Figure 53; and c) Figure 54. The area is indicated by the white box within the inset image.

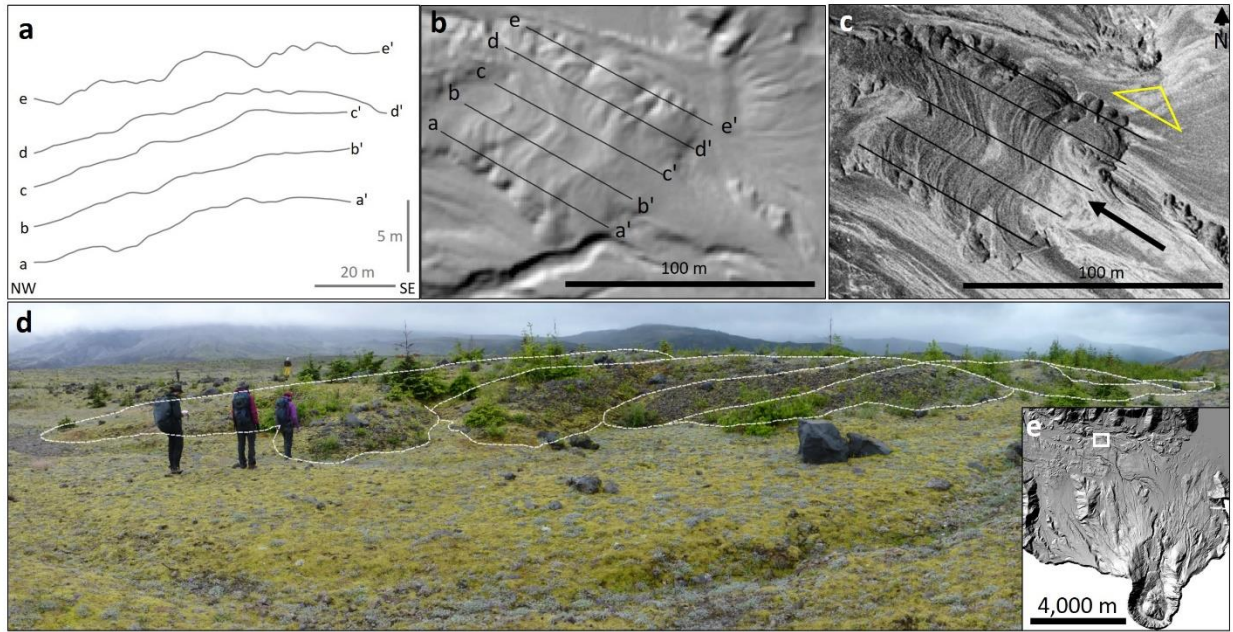


**Figure 52.** The USGS September 2009 data series 904 Lidar survey over the sheet-like section that contains surface ridges. Small black arrows (in a and b) indicate a few examples where a ridge is immediately followed by a furrow. An aerial photograph from the 31 July 1980 survey is shown in (c) over the same area.





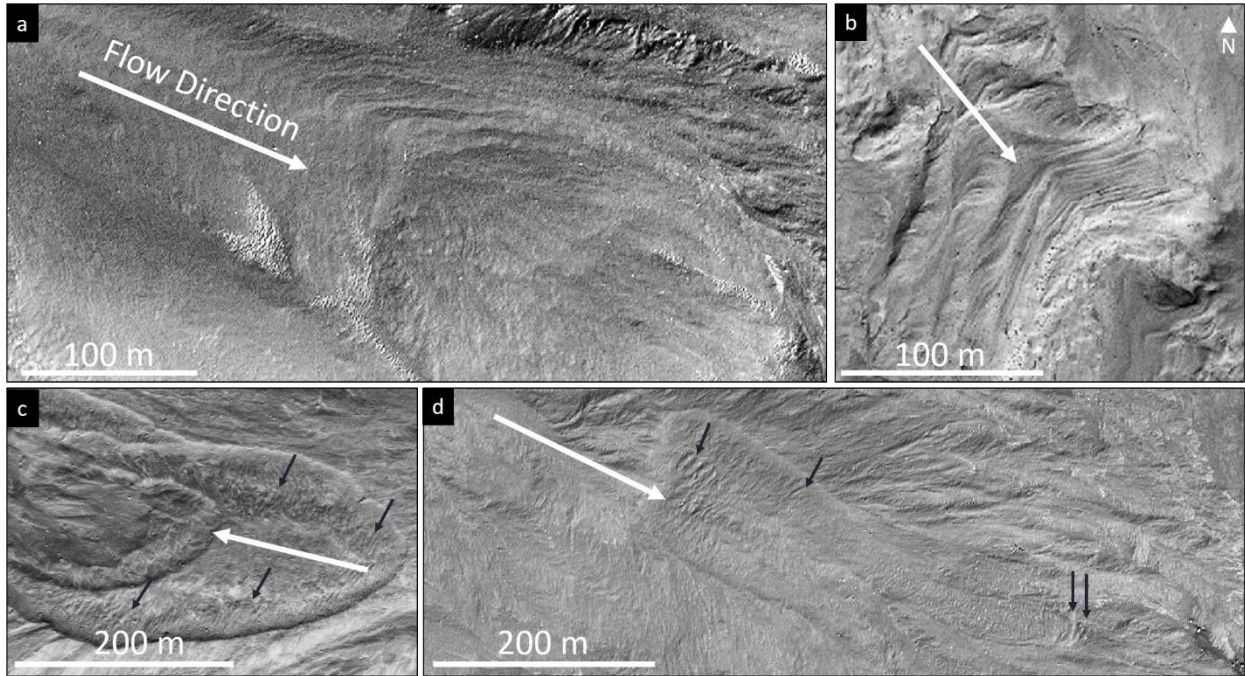
**Figure 53. Elevation profiles across the NW section of the MSH 18 May pyroclastic flow deposits taken from the USGS September 2009 Lidar survey (data series 904) and overlain on a USGS aerial photograph taken in the 31 July 1980 survey.**



**Figure 54. Elongate lobe containing multiple parallel ridges and toes along the lateral edges within the 18 May deposit: a) Lidar surface morphology sections shown in b; b) 2009 lidar survey with surface survey lines; c) aerial photograph taken 8 July 1980, the same area shown in b, yellow triangle indicates the photograph d; d) side view of the NE section showing multiple lobes overlaying each other. Area of interest is shown in inset.**

Ridges are also observed with herringbone morphologies where there is a topographic high in the underlying topography. This occurs within the MSH Pumice Plain deposits where lobes bifurcate around thicker deposit areas that were emplaced in the same flow sequence.

In the Shiveluch deposits, compression ridges are not as common. However, herringbone features occur in the 2010 deposit, where they form repeating parallel V-shaped sections (Figure 55a-b). No such features are preserved in the 2005 deposit. Smaller discontinuous ridges are present on the surface of some remobilized zones (Figure 55c-d). Compression ridges also occur in one location where a 2010 deposit pulse ‘bulldozed’ into the underlying deposit, forming elongate ridges perpendicular to the flow direction.



**Figure 55. a-b) Herringbone features in the Shiveluch 2010 deposit upstream from topographic highs, from Chapter two; b) compression ridges in the remobilized deposit within the arcuate scarps in the Shiveluch 2005 deposit; d) compression ridges on the surface of 2010 deposit. White arrows show flow direction, black arrows indicate examples of compression ridges.**

#### 4.4 DISCUSSION

Similarities between the two deposit types are present despite the differences in initiation mechanism (column-collapse versus dome-collapse), different eruption lengths, and different materials. The Shiveluch BAF deposits are predominantly ash and lapilli formed from low-vesicularity dome rock, while the MAH pumice plain deposits are predominantly composed of coarser vesicular pumice clasts. The Shiveluch BAF deposits formed during multiple collapse pulses over six to eight hours, while the MSH 22 July deposit was emplaced in a single event that occurred in five to ten minutes (Pallister et al., 2017). Instabilities in the flows are considered to

be a result of both source effects (fluctuations in dome or column collapse) and path effects (transportation prior to deposition). Pallister et al. (2017) discuss the formation of wave packets due to the development of roll waves, which are instabilities in the flow. The following sections discuss the similarities and differences seen across the two deposit types (Figure 56), and the implications of these results.



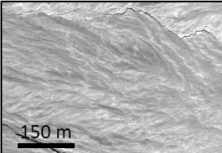
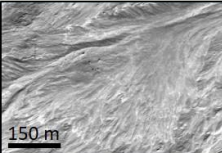
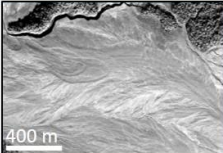
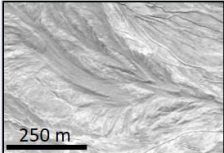

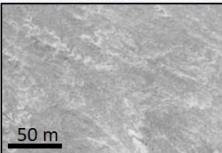
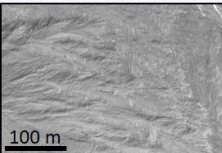
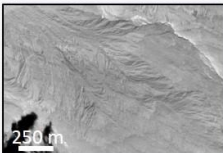
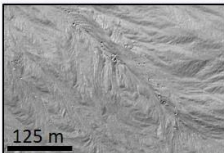
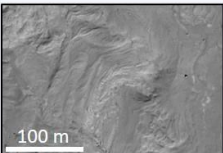
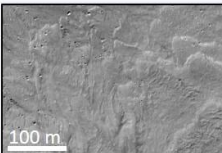
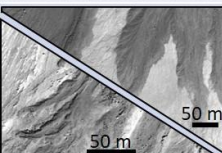
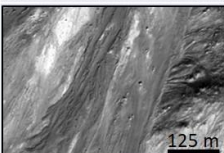

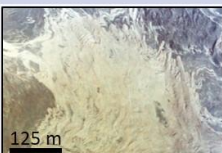

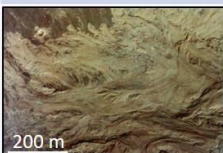




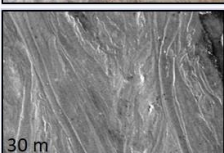

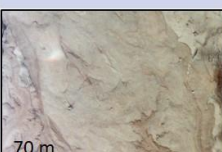
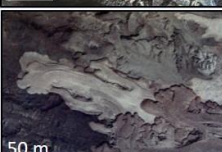

	Sheet-like	Lobes	Composite lobes	Primary levees & channels	Compression ridges	Remobilization
Shiveluch 2005						
2010						
2013						
MSH 18 May						
12 June						
22 July						

Figure 56. Examples of the similar morphological features across the MSH and Shiveluch PDC deposits, where present.

#### **4.4.1 Composite lobate features**

Retrogressive stacking of flow lobes in the same location to form larger composite lobate features is seen in the Shiveluch 2005 and 2010 deposits, and in the MSH Pumice Plain deposits (Figure 56). The BAF lobe fronts gradually taper in thickness and fan out, while the column-collapse deposits have steep lobe fronts and lateral boundaries, giving them a well-defined appearance in the field and in aerial photographs. The individual lobes are believed to have formed during the sustained collapse of an ash column that developed instabilities at the source, or through the development of kinematic waves during flow (Iverson, 1997; Major, 1997). In the case of Shiveluch, the lava dome has been shown to undergo multiple partial collapses during a single eruption (Chapter two), in addition to the kinematic wave development. The two eruption types probably have vent or dome instabilities during the initiation of the flows, but the similarities in morphological features in both deposit types suggests that they are also a consequence of shared transportation processes.

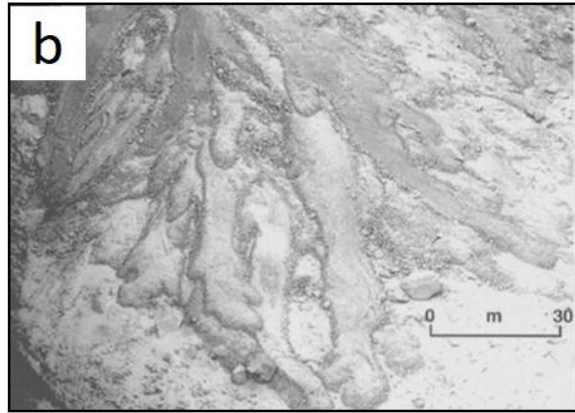
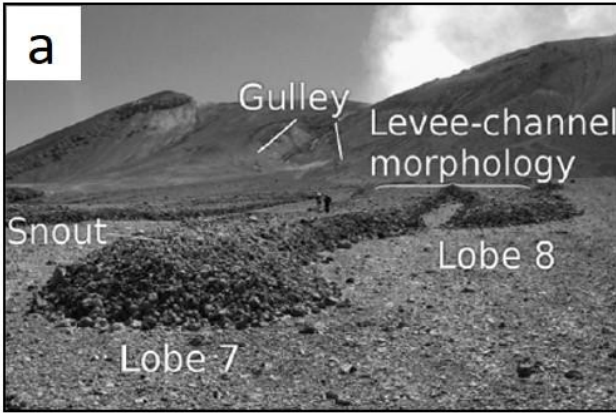
#### **4.4.2 Lobate morphology**

Both deposit types contain lobes and smaller toes along lobe edges. However, the MSH Pumice Plain lobate deposits are thicker have much better-defined boundaries with steeper walls and snouts than their analogues at Shiveluch which are diffuse and tapering (Figure 56). Rowley et al. (1981) recognized that the more elongate lobes with steeper flow fronts at MSH have a higher proportion of larger clasts. This is also evident in the 2013 Shiveluch BAF deposit; lobes that have low-relief, tapering, feathery flow boundaries also have a low proportion of blocks. Whereas,



elongate lobes with a higher relief (steeper flow fronts) contain a high concentration of blocks, which are visible in the flow fronts and levees. The higher concentration of coarser clasts decrease the flow mobility and velocity, which promotes migration of the clasts to flow fronts and lateral levees (Rowley et al., 1981; Johnson et al., 2012). This occurs in both the pumiceous low-density flows at MSH and the higher-density block and ash flows at Shiveluch.

A range of lobate morphologies formed in the deposits included in this study, with varying degrees of rounding, definition (sharp or diffuse), size, and length, and they occur singularly or in stacks or clusters. Similar features have also been produced during eruptions at other volcanoes (Figure 57). Lobate deposits have also been described in the 1993 Lascar pyroclastic flow deposits that occurred as a result of the collapse of a 23 km-high sub-Plinian column (Sparks et al., 1997; Jessop et al., 2012). These elongate lobe deposits extended as much as 8.5 km from the Lascar vent. They developed channel and levee structures, and they occur in numerous overlapping lobes with sharp terminations. Fountain-collapse and dome-collapse eruptions also produced lobate deposits during the 1997 eruption of Soufrière Hills volcano, Montserrat (Cole et al., 2002). The narrow and sinuous lobes have coarse, fines-depleted levees and snouts, similar to the MSH Pumice Plain deposits. Similar features occur in lobes formed on Ngauruhoe volcano during the 1975 Vulcanian eruption by column collapse and the remobilization of material that accumulated near the vent (Lube et al., 2007). Lube et al. (2007) concluded that the morphology of the levee and channel facies are affected by the underlying slope and the degree of lateral confinement (channelized or non-channelized). The 1990-1995 Unzen dome-forming eruption produced BAFs that extended to 5.5 km from the dome (Miyabuchi, 1999). The resulting deposits formed elongate, overlapping lobes, with most lobes up to 10 m-wide (maximum 20 m-wide) and tens of centimeters



**Figure 57. a) Lascar 1993 lobate pyroclastic flow deposits (Jessop et al., 2012); b) lobate dome collapse BAF deposits from the 11 April 1997 eruption of Soufriere Hills volcano (Cole et al., 2002); c) lobate flow front within the 2006 BAF on Merapi volcano (Gomez et al., 2009); d) BAF lobate deposits of the April 16-17 1991 eruption of Colima volcano; e) multiple distal lobes in the 1993 Lascar column collapse pyroclastic flow deposits (Sparks et al., 1997); f) distal lobate ends of the 1990-1995 Unzen volcano BAF deposits (Miyabuchi, 1999); g) lobate deposits**

thick. Small-volume BAF deposits were generated by dome collapse at Colima volcano on 16-17 April 1991 and extended to 4 km from the vent (Rodriguez-Elizarrards et al., 1991). These deposits formed a succession of overlapping lobes with steep flow fronts and levees. Dome collapse eruptions on Merapi volcano in 2006 produced channel-confined BAFs that extended to 7.78 km from the dome collapse site (Gomez et al., 2008, Thouret et al., 2010). During this Merapi eruption, lobes formed within the channelized deposit from 4.13 to 7.78 km distance from the dome (Thouret et al., 2010). Overlapping lobate morphologies have also formed in pyroclastic deposits generated by explosive lava-ice/water interactions on Klyuchevskoy volcano (Belousov et al., 2011). These deposits extend 2 km from the site of interaction, and reach 2 m in thickness with have steep lateral margins and lateral levees.

As described above, it is evident that lobate morphologies form in pyroclastic flow deposits produced by a range of processes and from eruptions characterized by Plinian or sub-Plinian column collapse, Vulcanian column collapse, collapse of lava domes or accumulated dome material, as well as from pyroclastic flows that are formed by lava-water/ice interactions. It is apparent that a range of PDC source mechanisms produce similarities in deposit morphology, which argues that deposit morphology is strongly controlled by transportation processes that are similar across PDC types.

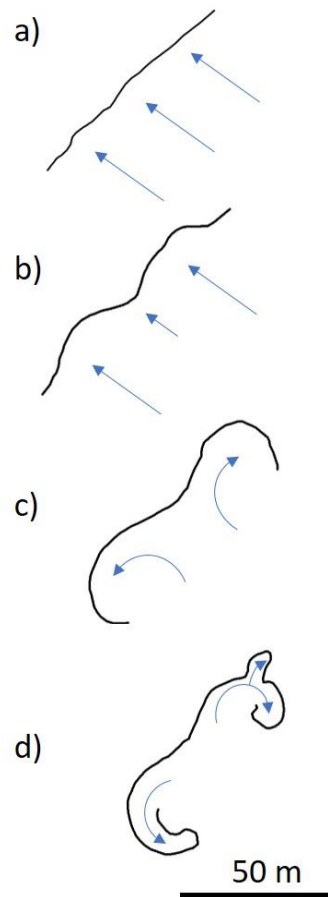
The most prominent difference between the Shiveluch and MSH deposits is the sharp versus diffuse character of the flow boundaries. The MSH deposits have thick, sharp flow fronts with a concentration of coarser clasts, whereas, the 2005 and 2010 Shiveluch deposits have tapering flow fronts and margins and these lack coarse clasts. Remarkably, the smaller 2013 Shiveluch deposit contains lobes similar to those observed in the MSH deposits, consequently, I suggest that in addition to the concentration of larger clast sizes within the flow, the size of the flow pulse itself likely controlled these features.

#### **4.4.3 Compression ridges versus levees**

The PDC deposits at Shiveluch and MSH both display features that are indicative of a rapid reduction in velocity during the final moments of deposition. These compressional ridges are a result of deposition during flow deceleration where the interaction with the underlying medium increases frictional resistance, causing the top of the flow to accumulate in linear ridges (Figure 49) (Dufresne and Davies, 2009). This friction between the lower material that was no longer in motion, and the overlying material as it comes to rest, results in the formation of these ridges and troughs.

This occurs as the material within the flow deposits from the bottom-upwards. In the field, these can appear to be stacked levees or breakaway scarps. Primary lateral levees are formed during rapid deceleration of clasts along the edges of flows due to the interaction with a relatively stationary substrate. The velocity gradient between the two (moving and stationary material) will slow the outer margins of the flow where coarser clasts accumulate due to grain-size segregation (Dufresne and Davies, 2009; Johnson et al., 2012). The foremost difference between compression

ridges and primary levees is that compression ridges occur perpendicular to flow direction, and stacked levees form parallel to flow direction.



**Figure 58. Sequence showing the formation of the rounded ridges in Figure 15. a) a flow front of the pyroclastic flow section moving with relatively similar velocities across the front; b) friction possibly caused by interaction with underlying topography, or material being emplaced directly ahead, causing the center to slow down; c) the material towards the edges slows and forms a rounded; d) the lateral edges of the lobe have curved around the central material and a smaller toe has broken out through the outermost edge. This sequence has occurred multiple times from the front to the back of the feature, and stacking from the base to the top.**

Secondary levees may also form by lahar or flood processes and look like primary flow levees in the field in situations where they are composed of the same material. Secondary V-shaped



ridges form when a flow bifurcates around a topographic high, and may look similar to levees in the field. It is also possible that additional componentry analysis of these levees could distinguish them from primary levees, as fines may have been removed during the secondary flowage event.

#### **4.4.4 Secondary remobilization**

Differentiating pyroclastic deposits that were produced by late depositional versus certain types of post-depositional processes can be difficult to distinguish in the field, but in certain situations they can be distinguished using remote sensing data. In places, the secondary material forms lobate morphologies similar to primary deposit features. PDCs at both volcanoes have undergone gravitational remobilization the uppermost layers of the deposits, creating break-away deposits that extend downslope from scarps. This is likely due to the high gas content within the fresh deposits, allowing the fluidization of the material. The high gas content within the MSH Pumice Plain deposits is described by Wilson and Head (1981) where they experienced the release of gas over a few seconds (sometimes in a jet) when applying a load to the deposit for several weeks after emplacement. A similar process was noted in the 2013 Shiveluch deposit where remobilization of gas-rich material occurred when pressure was applied (Gorbach et al., 2013).

The BAF and column-collapse deposit types contain morphological similarities over different deposit sizes, runout distances, and eruption styles, but changes in characteristics such as componentry and flow size result in distinct differences that are apparent in the lobate deposits. This investigation shows that the depositional processes that control the morphology of pyroclastic density currents are similar across initiation types, but they have distinct characteristics that differentiate them. Although both PDC types likely contain instabilities in column and dome

material collapsing, the similarities discussed here strongly suggest that the flow dynamics control the surface morphology.

## 4.5 CONCLUSIONS

The column-collapse and dome-collapse pyroclastic flow deposit morphologies at MSH and Shiveluch are the result of unsteady deposition caused primarily by flowage dynamics, with influence from an unsteady eruption rate or variable rates of dome collapse. They are composed of different material (vesicular pumice versus dense dome rock), of different compositions (dacite versus andesite). Even though the initiation type and physical material properties are different, they share similar morphological features and emplacement patterns. Both flow types result in: 1) pulsatory sheet-like deposition; 2) development of distinct lobate deposits; 3) retrogressive stacking of deposits with channel and levee systems; and 4) deposit remobilization. These similarities in morphologies across the different eruption types suggests that the flow transportation dynamics largely control the features, as opposed to the eruption dynamics.

The differences in lobate morphology is likely a result of the higher concentration of coarser clasts along lobe edges in the MSH deposits, causing the flow fronts to be steep and well-defined, while the ash-sized material in the Shiveluch BAF deposits produces a tapering margin that is less distinct. The smaller Shiveluch 2013 deposit has coarser blocks within the levees of the upstream lobes, resulting in sharp boundaries, while the block-poor downstream lobes are less defined, tapering, and feathery. This confirms the relationship between block size and boundary sharpness.

Compression ridges are formed on the surface of both deposit types through friction between the material that is nearing deposition, and the underlying material that deposited immediately before. This produces repeating lineations that differ from remobilization scarps as the ridges are raised, often with a depression or trough immediately behind (upstream). This is enhanced when the flow reaches a topographic high, forming herringbone (V-shaped) ridges or the redirection of flow lobes.

#### **4.6 ACKNOWLEDGEMENTS**

Funding for this Mount St. Helens research was provided through NASA Earth and Space Science Fellowship (2014-15, 2015-16, 2016-17), a USGS Jack Kleinman Grant for Volcano Research, and the Henry Leighton Memorial Graduate Scholarship. Field work was supported by the USGS Cascades Volcano Observatory (CVO). Photograph surveys were provided by USGS CVO and Brittany Brand.

## 5.0 CONCLUDING REMARKS

Using remote sensing tools coupled with field studies to examine explosive volcanic deposits provides insights into a volcano's recent eruptive history and eruption mechanisms. This information can be important to provide a safe and rapid assessment of eruptive products at dangerous and/or remote volcanoes around the world. The spectrum of pyroclastic density currents (PDCs) range from dense debris avalanches and block and ash flows (BAFs), to dilute pyroclastic flows and surges, resulting from different eruption, transportation, and depositional processes. Investigating these deposits from outcrop-scale in the field to aerial and satellite imagery, enables evaluation of eruption deposits for the purpose of characterizing deposits and interpreting late-stage flow behavior.

This research has focused on quantifying the distribution of eight dome collapse events, their related BAF deposits, and precursory thermal anomalies on the dome, on Shiveluch volcano in Chapter one; then described the two largest Shiveluch 2005 and 2010 BAF deposits using high-resolution- and field-data in Chapter two; and compared these results to the 1980 pyroclastic flow deposits at Mount St. Helens volcano in Chapter three. This study utilized a range of spatial and wavelength and scales: from orbital Advanced Spaceborne Thermal Emission and Reflection Radiometer ASTER Thermal Infrared (TIR, 90 m<sup>2</sup> pixel size) and ASTER Visible-Near Infrared (VNIR, 15 m<sup>2</sup> pixel size) data; to high-resolution WorldView-02 and QuickBird-02 panchromatic (0.46 and 0.65 m<sup>2</sup> pixel size, respectively), Lidar (1 m<sup>2</sup> pixel size) and aerial photography (~ 0.2 m<sup>2</sup> pixel size) data; down to observations of the deposits in the field. Shiveluch volcano was selected because of the range of BAF deposit sizes that have been emplaced since 2001, and the availability of ASTER data to image the deposits and dome collapse scars. Mount St. Helens

volcano was selected because of the great wealth of data collected and analyzed during and after the eruptions. This is an excellent opportunity to compare two different PDC deposit types to identify the similarities and differences in order to determine source (eruption) versus path (transportation) effects on the resulting deposit morphology.

Thermal data were collected for dates prior to six of the eight Shiveluch partial dome collapse events to investigate whether there were any increases in thermal output in the collapse areas that could be retrospectively identified (Chapter one). Thermal anomalies were identified in the upper or middle regions of the associated dome collapse, although all except one (the 2009 collapse event) did not correspond with the area and size of the collapse. This increase in thermal output prior to the events may be due to the opening of fractures that exposes hot interior dome material leading to the collapse.

The BAFs are a result of partial collapse events and their flow direction is controlled by the location of collapse on the 1,350 m-wide dome, and the topography at the base of the dome. The BAF deposits on Shiveluch volcano have long runout distances, emplacing material to 19 km from the collapse scars, including large blocks with >11 m maximum diameter to distances greater than 11 km. Runout distances were often increased due to the BAF material entering channels, forming an elongated narrow deposit section beyond the main deposit fan. The 2010 BAF produced a large fan deposit, and an additional 5.4-km-long channelized deposit in the Kabeku River channel. Evidence for pulsatory dome collapse events is present in the surface morphology of the BAF deposits, and in stratigraphic sections that show discontinuous units within the 2005 deposit (described in Chapter three). This hypothesis was confirmed in webcam footage of the 3 December 2013 collapse event. The footage showed three large collapse pulses with multiple smaller pulses between them, that together formed the BAF deposit.



The Shiveluch 2005 and 2010 BAF deposits are two of the largest historical deposits of this type. They were emplaced through multiple stages of retrogressive dome collapse and both have evidence for associated dilute pyroclastic surge deposits, surrounding the 2005 deposit and up the walls of the 2010 channelized section. The surface facies and discontinuous stratigraphic units are described in Chapter two. This study shows how extensive dome-collapse BAFs can be, and how topography can play an important role in extending the flow for a significant distance beyond the main depositional area. Understanding these prolonged dome growth episodes and describing the largest of these deposits to understand the extreme end of the deposit size and runout range is important for determining the maximum hazard extent of other dome collapse events.

The comparison of the BAF and pyroclastic flow deposits at Shiveluch and Mount St. Helens volcanoes show the similarities in surface morphology, even though they are composed of different material. Additionally, differences that allow the remote identification of the two different initiation mechanisms are described. The two flow types produced deposits that share similar emplacement patterns: 1) pulsatory sheet-like deposition; 2) development of distinct lobate deposits; 3) retrogressive stacking of deposits with channel and levee systems; and 4) deposit remobilization.

This work demonstrates the additional understanding of deposits that can be gained through using a range of spatial and wavelength scales acquired in remote sensing data. This, coupled with field studies, provides a basis for identifying the eruption type, and the sequence of deposition. This is especially useful in the large Shiveluch BAF deposits, where the extensive size makes it difficult to understand these larger-scale processes in the field.

## APPENDIX A

### SHIVELUCH ERUPTION DESCRIPTIONS

#### A.1 PRE-2001 ACTIVITY

Activity increased in 1964 and culminated in the formation of a horseshoe-shaped crater during a 70-minute-long eruption on 12 November of that year, involving a large-scale edifice collapse towards the south and a Plinian eruption that emplaced pumiceous fall and pyroclastic density current deposits (Belousov, 1994; Gorelchik, 1996). The fan-shaped hummocky debris avalanche deposit has a volume of  $1.154 \text{ km}^3$  and an aerial extent of  $98\text{-}100 \text{ km}^2$  (Belousov, 1995). The Plinian eruption produced an eruption column about 15 km high and deposited  $0.3\text{-}0.5 \text{ km}^3$  of vesicular andesite pyroclastic density current material over a  $50 \text{ km}^2$  area around the eastern and western edges of the debris avalanche deposit, with thicknesses up to 30 m (Belousov, 1994; Gorelchik et al., 1996).

Activity from late 1964 to August 1980 was limited to fumarolic activity (Gorelchik et al., 1996). Activity resumed with three dome-forming cycles: 1980-1981, 1993-1995, and 2001-onwards (Fedotov, S. A., et al., 2004). The first cycle of extrusive dome growth began in late August 1980, with no recorded precursory seismic activity (Gorelchik et al., 1977; Zharinov, N. A. and Y. V. Demyanchuk, 2008; Zharinov, N. A. and Y. V. Demyanchuk, 2013). Dome growth began in the 1964 collapse crater and from 1980 to 1981, a  $0.0198 \text{ km}^3$  dome formed (Belousov, 1994 and references therein). The maximum extrusive dome growth rate was observed through

August-September 1980, which ceased by the end of 1981 (Gorelchik et al., 1996). Dome growth occurred without any notable explosive activity, gravitational collapses, or pyroclastic density current formation. Minor activity occurred between the first two dome-forming cycles with explosive activity (producing small avalanches and block and ash flows) on the stagnated dome in 1984 and episodic ash plumes until 1992. The 1993-1995 dome-forming cycle began on 21 April 1993 with the most vigorous eruption since 1964 producing an ash plume up to 18 km with pyroclastic density currents and lahars extending to a distance of 15-20 km, erupting a total volume of 0.05 km<sup>3</sup> (Gorelchik et al., 1997). During this time, the maximum discharge rate was up to 1.25 million m<sup>3</sup> per day (Zharinov and Demyanchuk, 2008). Other dome processes over the study period (2001-2013) have been summarized by Gorbach et al. (2016).

## **A.2 19 MAY 2001**

The following account of the activity leading to the 2001 activity is from Fedotov et al. (2001) and others where referenced. Prior to 2001, Shiveluch had been in a period of quiescence since January 1995 with occasional tremor and steam/gas emission occasionally containing ash. The renewed activity commenced with emissions in early January, intensifying fumarolic activity in February, and weak seismic swarm events in March with a significant increase in intensity in late April occurring several kilometers below the summit. Extrusive dome-building was preceded by an increase in seismic activity. Another sharp increase in seismicity occurred on 29 April 2001 and marked the extrusion of an andesitic lava flow. Ash emissions began on 1 May with and the eruption evolved to produce pyroclastic density currents on 7 May that extended southwest to 1.5-

2 km from the dome. On 12 May, a new extrusive dome was observed on the western side of the older dome. The 2-hour long May 19 paroxysmal eruption produced an ash column to 10-20 km a.s.l., a block and ash flow, and a lahar that traveled over 30 km, covering an area of 70 km<sup>2</sup> up to 10 m thick (Fedotov et al., 2001). Explosive eruptions over 19-22 May largely destroyed the newly formed dome and part of the old 1980-1995 dome. A field excursion by Fedotov et al. (2004) noted a deposit thickness up to 8 m and temperature of 120°C at 1 m depth, two months after emplacement. The composition of the deposit is mainly of rounded juvenile pumiceous amphibole-plagioclase andesite clasts and dense dome material.

### **A.3 10 MAY 2004**

Endogenous dome growth occurred through 2003 and reverted to extrusive activity around the time of the 10 May 2004 eruption (Shevchenko and Svirid, 2014). An explosive eruption began either immediately before or after the dome collapse commenced, with ash-producing eruptions occurring over the following two days. The 10 May eruption began around 0110 local time with the most active phase continuing for ~5 hours producing an ash plume up to 8-11 km a.s.l. (Girina et al., 2004). A lahar produced by hot deposits melting snow destroyed a bridge over the Bekesh River (Girina et al., 2004). Activity at the dome subsided (no visible activity was recorded) for 5-7 months until a 400 m-long, 100 m-wide viscous lava flow extruded from May to August, which subsequently collapsed in September (Zharinov and Demyanchuk, 2008).

#### A.4 27-28 FEBRUARY 2005

By early February the dome was the largest it had been since dome growth began in August 1980 (Zharinov and Demyanchuk, 2008). Based on seismic data the explosive eruption commenced at 18:25 (local time) on 27 February and the most intense activity occurred from 2334 on the 27, to 0115 on 28 February, after which the seismic station located on an elevated area 7.5 km southwest of the dome (station SVL) stopped recording due to being destroyed by the block and ash flow. The 8 hour and 50-minute eruption comprised multiple explosions and block and ash flows, lowering the dome height by 125 m. After this, seismic signals were difficult to distinguish from those produced by nearby Klyuchevskoy volcano. The eruption produced the second largest block and ash flow on Shiveluch (which was later exceeded by the 27 October 2010 eruption) with a dome rock volume of  $0.11 \text{ km}^3$  (Shevchenko and Svirid, 2014). An ASTER TIR scene acquired 29 days after the eruption registered the largest thermal anomaly ever recorded in Kamchatka over the dome and deposit area (Carter and Ramsey, 2010). Phreatic explosions occurred within the deposit over 3-5 May due to the interaction between meltwater and the hot dome material at a distance of 10-12 km from the dome (Zharinov and Demyanchuk, 2008).

A viscous lava flow grew from the location of the dome collapse from March to July reaching a length of 400 m (Girina and Nuzhdaev, 2013, Zharinov and Demyanchuk, 2013). Geochemical data suggests that the explosive-extrusive activity of 2004-2005 was due to the introduction of a high temperature melt, with rapid crystallization leading to an increase in volatile content and heating of the magma chamber. This is supported by the presence of gabbro-diorite inclusions in the 2005 lavas (Gorbach, 2006). By August 2005 a new dome with a width of 300 m had grown in the collapse scar, and a crater formed in the center of the dome due to explosive activity in June and July (Ramsey et al., 2012; Girina and Nuzhdaev, 2013; Zharinov and

Demyanchuk, 2013). An explosive eruption from the southwest side of the new dome occurred on 22 September over 8.6 hours, producing a narrow 4-5 m thick block and ash flow deposit that extended 20 km down the Baidarnaya river channel recently formed within the 28 February deposit (Girina and Nuzhdaev, 2013).

Following the 27-28 February eruption, the activity at Shiveluch consisted of 3-4 ash eruptions per year until an increase to 21 ash eruptions in 2007. Over 2006 there was little change in the dome height with activity limited to lava extrusion on the eastern side of the dome and moderate fumarolic activity. Explosive ash eruptions recommenced in December 2006 (Zharinov and Demyanchuk, 2008, KVERT reports) and in November 2007 lava extrusion returned to the southwest side of the dome (Zharinov and Demyanchuk, 2013).

#### **A.5 18-19 DECEMBER 2007**

Prior to the 18-19 December 2007 collapse event, ash and lava discharge and avalanches from the dome were frequent with nightly incandescence visible from January to November. The maximum dome volume of 360 million m<sup>3</sup> was reached by October (Zharinov and Demyanchuk, 2008, KVERT reports).

#### **A.6 25-26 JUNE 2009**

There was a decrease in explosive activity over 2008 with a total of six ash explosions and a lava flow on the southern side of the dome that extruded from January to May-October (Zharinov



and Demyanchuk, 2013). Over 2007-2008 the dome height grew by 96 m on the eastern side (Zharinov and Demyanchuk, 2013). Explosive and extrusive activity increased in late-January to early March 2009, increasing the dome height by an additional 38 m (Zharinov and Demyanchuk, 2013). The 25-26 June 2009 eruption occurred after a week of elevated activity, producing block and ash flows and ash plumes up to 5 km a.s.l.

#### **A.7 27 OCTOBER 2010**

Over the 13 days prior to the 27 October 2010 dome collapse there was a sharp decrease in seismicity, which elevated again on October 26 to ‘slightly above background level’ (Shevchenko and Svirid, 2014). The 27 October eruption is one of the most explosive eruptions at Shiveluch since activity renewed in August 1980 (Zharinov and Demyanchuk, 2013) and at the time of writing Shiveluch has not produced a larger eruption since. The collapse formed an elongate scar in the eastern side of the dome and talus apron, which was calculated by Dvigalo et al., 2011 (Shevchenko and Svirid, 2014) to have a volume of 0.28 km<sup>3</sup>. The eruption generated an ash plume that deposited ash over 2000 km<sup>2</sup>, with a total eruptive mass of 7.8 million tons (Zharinov and Demyanchuk, 2013).

#### **A.8 26 JULY 2013**

Prior to the 26 July 2013 eruption, a lava flow was extruded on the northwestern to northern and northeastern flank of the dome. The activity leading to the 26 July eruption consisted of lava

extrusion, moderate to strong fumarolic activity, small avalanches, and explosive eruptions (KVERT reports). The 26 July eruption began at 2255 (local time) producing ash plumes up to 10 km that traveled 520 km to the southeast of Shiveluch, and a pyroclastic density current deposit. The deposit contained hot pumiceous andesite clasts in a fine matrix that remobilized when touched due to the high gas content (Gorbach et al., 2013). After the 26 July eruption, moderate ash eruptions continued until December, when a new dome began to grow on the northwestern side of the previous dome.

### **A.9 3 DECEMBER 2013**

Activity continued until December 2013 with viscous lava extrusion on the northwestern flank of the dome, ash explosions, fumarolic activity, and hot avalanches (December 2013 KVERT reports). A strong explosive event began at 1325 on 3 December. Ash plumes reached 8-9 km a.s.l. and extended 200 km north of Shiveluch, and large pyroclastic flows descended from the southwestern and northwestern flanks of the dome. This deposit was also investigated by Reath (2017).

## BIBLIOGRAPHY

- Andreastuti, S., Paripurno, E., Gunawan, H., Budianto, A., Syahbana, D., Pallister, J., 2017. Character of community response to volcanic crises at Sinabung and Kelud volcanoes. *Journal of Volcanology and Geothermal Research*, In Press.
- Banks, N.G., Hoblitt, R.P., 1981. Summary of temperature studies of 1980 deposits. In Lipman, P.W., Mullineaux, D.R., [Eds.]. *The 1980 eruptions of Mount St. Helens, Washington*. U.S. Geological Survey Professional Paper 1250, pp. 489-512.
- Bardintzeff, J.M., 1948. Merapi volcano (Java, Indonesia) and Merapi-Type Nuèe Ardente. *Bulletin of Volcanology*, 47(3): 433-446.
- Belousov, A.B., 1995. The Shiveluch volcanic eruption of 12 November 1964 - explosive eruption provoked by failure of the edifice. *Journal of Volcanology and Geothermal Research*, 66: 357-365.
- Belousov, A., Belousova, M., Voight, B., 1999. Multiple edifice failures, debris avalanches and associated eruptions in the Holocene history of Shiveluch volcano, Kamchatka, Russia. *Bulletin of Volcanology*, 61: 324-342.
- Belousov, A., Voight, B., Belousova, M., 2007. Directed blasts and blast generated pyroclastic density currents: a comparison of the Bezymianny 1956, Mount St Helens 1980, and Soufrière Hills, Montserrat 1997 eruptions and deposits. *Bulletin of Volcanology*, 69: 701-740.
- Bernstein, M., Pavez, A., Varley, N., Whelley, P., Calder, E.S., 2013. Rhyolite lava dome growth styles at Chaitén volcano, Chile (2008-2009): interpretation of thermal imagery. *Andean Geology*, 40(2): 295-309.
- Bindeman, I.N., Ponomareva, V.V., Bailey, J.C., Valley, J.W., 2004. Volcanic arc of Kamchatka: a province with high-delta O-18 magma sources and large-scale O-18/O-16 depletion of the upper crust. *Geochimica et Cosmochimica Acta* 68(4), 841–865.
- Bourdier, J.-L., Adburachman, E.K., 2001. Decoupling of small-volume pyroclastic flows and related hazards at Merapi volcano, Indonesia. *Bulletin of Volcanology*, 63:309-325.
- Brand, B.D., Mackaman-Lofland, C., Pollock, N.M., Bendaña, S., Dawson, B. and Wichgers, P., 2014. Dynamics of pyroclastic density currents: conditions that promote substrate erosion and self-channelization—Mount St Helens, Washington (USA). *Journal of Volcanology and Geothermal Research*, 276, pp.189-214.
- Branney, M.J., Kokelaar, P., 2002. Pyroclastic Density Currents and the Sedimentation of Ignimbrites. *Geological Society of London Memoirs*, 27.

- Brantley, S.R., Waitt, R.B., 1988. Interrelations among pyroclastic surge, pyroclastic flow, and lahars in Smith Creek valley during the first minutes of 18 May, 1980 eruption of Mount St. Helens, USA. *Bulletin of Volcanology*, 50: 304-326.
- Burgisser, A. and Bergantz, G.W., 2002. Reconciling pyroclastic flow and surge: the multiphase physics of pyroclastic density currents. *Earth and Planetary Science Letters*, 202(2), pp.405-418.
- Bursik, M., Patra, A., Pitman, E.B., Nichita, C., Macias, J.L., Saucedo, R. and Girina, O., 2005. Advances in studies of dense volcanic granular flows. *Reports on Progress in Physics*, 68: 271-301.
- Calder, E.S., Luckett, R., Sparks, R.S.J., Voight, B., 2002. Mechanisms of lava dome instability and generation of rockfalls and pyroclastic flows at Soufrière Hills Volcano, Montserrat. *Geological Society, London, Memoirs* 2002; v. 21; p. 173-190. doi:10.1144/GSL.MEM.2002.021.01.08
- Calder, E.S., Lavalée, Y., Kendrick, J.E., Bernstein, M., 2015. Lava dome eruptions. In: Sigurdsson, H., Houghton, B., McNutt, S, (Eds.), *The Encyclopedia of Volcanoes* (2). Saint Louis, US: Academic Press, 2015.
- Carn, S.A., Watts, R.B., Thompson, G., Norton, G.E., 2004. Anatomy of a lava dome collapse: the 20 March 2000 event at Soufriere Hills Volcano, Montserrat. *Journal of Volcanology and Geothermal Research*, 131: 241-264.
- Carter, A.J., Ramsey, M.S., Belousov, A.B., 2007. Detection of a new summit crater on Bezymianny Volcano lava dome: satellite and field-based thermal data. *Bulletin of Volcanology*, 69(7): 811-815.
- Cas, R.A., Wright, H.M., Folkes, C.B., Lesti, C., Porreca, M., Giordano, G. and Viramonte, J.G., 2011. The flow dynamics of an extremely large volume pyroclastic flow, the 2.08-Ma Cerro Galán Ignimbrite, NW Argentina, and comparison with other flow types. *Bulletin of Volcanology*, 73(10), pp.1583-1609.
- Charbonnier, S.J., Gertisser, R., 2009. Numerical simulations of block-and-ash flows using the Titan2D flow model: examples from the 2006 eruption of Merapi Volcano, Java, Indonesia. *Bulletin of Volcanology*, 71:953-959.
- Charbonnier, S.J., Gertisser, R., 2013a. Evaluation of geophysical mass flow models using the 2006 block-and-ash flows of Merapi Volcano, Java, Indonesia: Towards a short-term hazard assessment tool. *Journal of Volcanology and Geothermal Research*, 231-232: 87-108.
- Charbonnier, S.J., Germa, A., Connor, C.B., Gertisser, R., Preece, K., Komorowski, J.C., Lavigne, F., Dixon, T., Connor, L., 2013b. Evaluation of the impact of the 2010 pyroclastic density currents at Merapi volcano from high-resolution satellite imagery, field investigations and numerical simulations. *Journal of Volcanology and Geothermal Research*, 261: 295-315.

- Criswell, C.W., 1987. Chronology and pyroclastic stratigraphy of the 18 May, 1980, eruption of Mount St. Helens, Washington. *Journal of Geophysical Research*, 92(B10): 10,237-10,266.
- Christiansen, R.L., and Peterson, D.W., 1981. Chronology of the 1980 eruptive activity. In Lipman, P.W., Mullineaux, D.R., [Eds.]. *The 1980 eruptions of Mount St. Helens, Washington*. U.S. Geological Survey Professional Paper 1250, pp. 489-512.
- Cole, P.D., Calder, E.S., Druitt, T.H., Hoblitt, R., Robertson, R., Sparks, R.J.S., Young, S.R., 1998. Pyroclastic flows generated by gravitational instability of the 1996-97 lava dome of Soufriere Hills Volcano, Montserrat. *Geophysical Research Letters*, 25(18): 3425-3428.
- Cole, P.D., Calder, E.S., Sparks, R.S.J., Clarke, A.B., Druitt, T.H., Young, S.R., Herd, R.A., Haford, C.L., Norton, G.E., 2002. Deposits from dome-collapse and fountain-collapse pyroclastic flows at Soufrière Hills Volcano, Montserrat. *The Geological Society of London, Memoirs*, 21: 231-262.
- Cronin, S.J., Lube, G., Dayudi, D.S., Sumarti, S., Subrandiyo, S., Surono, 2013. Insights into the October–November 2010 Gunung Merapi eruption (Central Java, Indonesia) from the stratigraphy, volume and characteristics of its pyroclastic deposits. *Journal of Volcanology and Geothermal Research*, 261: 244-259.
- Dellino, P., La Volpe, L., 1995. Fragmentation versus transportation mechanisms in the pyroclastic sequence of Monte Pilato-Rocche Rosse (Lipari, Italy). *Journal of Volcanology and Geothermal Research*, 64: 211:231.
- Dennen, R.L., Bursik, M.I., Roche, O., 2014. Dome collapse mechanisms and block-and-ash flow emplacement dynamics inferred from deposit and impact mark analysis, Mono Craters, CA. *Journal of Volcanology and Geothermal Research*, 276: 1-9.
- Dirksen, O., Humphreys, M.C.S., Pletchov, P., Melnik, O., Demyanchuk, Y., Sparks, R.S.J., Mahony, S., 2006. The 2001-2004 dome-forming eruption of Shiveluch volcano, Kamchatka: Observation, petrological investigation and numerical modelling. *Journal of Volcanology and Geothermal Research*, 155: 201-266.
- Dufrense, A. and Davies, T.R., 2009. Longitudinal ridges in mass movement deposits. *Geomorphology*, 105: 171-181.
- Dvigalo, V.N., Svirid, I.Yu., Shevchenko, A.V., Sokorenko, A.V., Demyanchuk, Yu.V., 2011. Active volcanoes of northern Kamchatka as seen from aerophotogrammetric data in 2010. Proceedings of regional conference “Volcanism and associated processes”. Institute of Volcanology and Seismology FEB RAS, Petropavlovsk-Kamchatsky, pp. 26–36 (in Russian).
- Fedotov, S.A., Dvigalo, V.N., Zharinov, N. A., Ivanov, V. V., Seliverstov, N. I., Khubunaya, S. A., Demyanchuk, Yu. V., Markov I. A., Osipenko, L. G., Smelov, N. P., 2001. Eruption of Shiveluch volcano in May-July 2001. *Journal of Volcanology and Seismology*, 6:3-15. (In Russian).

- Fedotov, S.A., Zharinov, N.A., Dvigalo, V.N., Seliverstov, N.I. and Khubunaya, S.A., 2004. The 2001–2004 eruptive cycle of Shiveluch Volcano. *Journal of Volcanology and Seismology*, 6: 3-14.
- Fisher, R.V., Heiken, G., 1982. Mt. Pelée, Martinique: May 8 and 20, 1902, pyroclastic flows and surges. *Journal of Volcanology and Geothermal Research*, 13(3-4): 339-371.
- Gillespie, A.R., Rokugawa, S., Matsunaga, T., Cothern, J.S., Hook, S., Kahle, A.B., 1998. A Temperature and Emissivity Separation Algorithm for Advanced Spaceborne Thermal Emission and Reflection Radiometer (ASTER) images. *IEEE Transactions on Geoscience and Remote Sensing*, 36(4):1113-1126.
- Girina, O.A., Senyukov, S.L., Demyunchuk, Y.V., Khubunaya, S.A., Ushakov, S.V., 2004. The eruption of Sheveluch volcano, Kamchatka, on May 10, 2004. IV International Biennial Workshop on Subduction Processes emphasizing the Japan-Kurile-Kamchatka-Aleutian Arcs, Petropavlovsk- Kamchatsky.
- Girina, O.A., Manevich, A.G., Malik, N.A., Mel'nikov, D.V., Ushakov, S.V., Demyanchuk, Y.U. and Kotenko, V., 2007. Active volcanoes of Kamchatka and northern Kurils in 2005. *Journal of Volcanology and Seismology*, 1(4): 237-347.
- Glicken, H. 1996. Rockslide-debris Avalanche of May 18, 1980, Mount St. Helens Volcano, Washington: U.S. Geological Survey Open-File Report 96-677, 90 p., 5 plates, <https://pubs.usgs.gov/of/1996/0677/>.
- Gorelchik, V.I., Shirokov, V.A., Firstov, P.P., Chubarova, O.S., 1996. Shiveluch volcano: seismicity, deep structure and forecasting eruptions (Kamchatka). *Journal of Volcanology and Geothermal Research*, 78: 121-132.
- Gorbach, N.V., 2006. Extrusive dome formation at Shiveluch Volcano and its lava composition in 2004–2005. Proceedings of international symposium “Problems of explosive volcanism”. Institute of Volcanology and Seismology FEB RAS, Petropavlovsk- Kamchatsky, pp. 112–119 (in Russian).
- Gorbach, N.V., Portnyagin, M.V., 2011. Geology and Petrology of the Lava Complex of Young Shiveluch Volcano, Kamchatka. *Petrology*, 19(2):134-166.
- Gorbach, N.V., Plechova, A.A., Ponomareva, V.V., Tembrel, I.I., 2013. The explosive Shiveluch eruption of July 26, 2013. *Bulletin of Kamchatka Association “Educational-Scientific Center”* 2: 15–19.
- Gorbach, N.V., Portnyagin, M.V., Filosofova, T.M., 2016. Dynamics of Extrusive Dome Growth and Variations in Chemical and Mineralogical Composition of Young Shiveluch Andesites in 2001–2013. *Journal of Volcanology and Seismology*, 10(6):37-61.
- Gunawan, H., Budianto, A., Kartadinata, N., Prambada, O., Pallister, J., McCausland, W., 2017. Overview of the Volcanic History and Eruption Chronology of Sinabung 2010-2014. *Journal of Volcanology and Geothermal Research* (in press).



- Hanenkamp, E., 2011. Decoupling processes in block-and-ash flows: field evidence and analogue modelling. PhD Thesis University of Canterbury (254 pp).
- Harnett, C.E., Murphy, W., Thomas, M., Neuberg, J., 2017. Global Archive of Dome Instabilities (GLADIS). <https://vhub.org/resources/4149>.
- Hayashi, J.N., Self, S., 1992. A comparison of pyroclastic flow and debris avalanche mobility. *Journal of Geophysical Research*, 97:9063-9071.
- Herd, R.A., Edmonds, M., Bass, V.A., 2005. Catastrophic lava dome failure at Soufrière Hills Volcano, Montserrat, 12-13 July 2003. *Journal of Volcanology and Geothermal Research*, 148:234-252.
- Hoblitt, 1986. Observations of eruptions, 22 July and August 7, 1980, Mount St. Helens, Washington. U.S. Geological Survey Professional Paper 1335.
- Hochstaedter, A.G., Kepezhinskas, P., Defant, M., Drummond, M., Koloskov, A., 1996. Insights into the volcanic arc mantle wedge from magnesian lavas from the Kamchatka arc. *Journal of Geophysical Research-Solid Earth* 101 (B1), 697–712.
- Iverson, R., 1997. The physics of debris flows. *Reviews of Geophysics*, 35(3): 245-296.
- Iverson RM, Schilling SP, Vallance JW (1998) Objective delineation of lahar-inundation hazard zones. *Geological Society of America Bulletin*, 110:972–984
- Jessop, D.E., Kelfoun, K., Labazuy, P., Mangeney, A., Roche, O., Tillier, J.-L., Trouillet, M., Thibault, G., 2012. LiDAR derived morphology of the 1993 Lascar pyroclastic flow deposits, and implication for flow dynamics and rheology. *Journal of Volcanology and Geothermal Research*, 245-246:81-97.
- Johnson, C.G., Kokelaar, B.P., Iverson, R.M., Logan, M., LaHusen, R.G., Gray, J.M.N.T., 2012. Grain-size segregation and levee formation in geophysical mass flows. *Journal of Geophysical Research*, 117. doi:10.1029/2011JF002185.
- Kepezhinskas, P., McDermott, F., Defant, M.J., Hochstaedter, A., Drummond, M.S., Hawkesworth, C.J., Koloskov, A., Maury, R.C., Bellon, H., 1997. Trace element and Sr–Nd–Pb isotopic constraints on a three-component model of Kamchatka arc petrogenesis. *Geochimica et Cosmochimica Acta* 61 (3), 577–600.
- Komorowski, J. C.-., Jenkins, S., Baxter, P.J., Picquout, A., Lavingne, F., Charbonnier, S., Gertisser, R., Preece, K., Cholik, N., Budi-Santoso, A., Surono, 2013. Paroxysmal dome explosion during the Merapi 2010 eruption: Processes and facies relationships of associated high-energy pyroclastic density currents. *Journal of Volcanology and Geothermal Research*, 261: 260-294.
- Kuntz, M.A., Rowley, P.D., MacLeod, N.S., Reynolds, R.L., McBroome, L.A., Kaplan, A.M., Lidke, D.J., 1981. Petrography and particle-size distribution of pyroclastic-flow, ash-cloud, and surge deposits, in Lipman, P.W., Mullineaux, D.R., [Eds.]. *The 1980 eruptions of*

- Mount St. Helens, Washington. U.S. Geological Survey Professional Paper 1250, pp. 489-512.
- Lipman, P.W., Mullineaux, D.R., 1981 [Eds.] The 1980 eruptions of Mount St. Helens, Washington. U.S. Geological Survey Professional Paper 1250, pp. 513-524.
- Loughlin, S.C., Calder, E.S., Clarke, A., Cole, P.D., Luckett, R., Mangan, M.T., Pyle, D.M., Sparks, R.S.J., Voight, B., Watts, R.B., 2002. Pyroclastic flows and surges generated by the 25 June 1997 dome collapse, Soufriere Hills Volcano, Montserrat. In Druitt, T. H. & Kokelaar, B. P. (eds) 2002. The Eruption of Soufriere Hills Volcano, Montserrat, from 1995 to 1999. Geological Society, London, Memoirs, 21, 191-209. 0435-4052/02/\$15
- Lube, G., Cronin, S.J., Platz, T., Freundt, A., Proctor, J.N., Henderson, C., Sheridan, M.F., 2007. Flow and deposition of pyroclastic granular flows: A type example from the 1975 Ngauruhoe eruption, New Zealand. *Journal of Volcanology and Geothermal Research*, 161: 165-186.
- Mackaman-Lofland, C., Brand, B.D., Taddeucci, J., Wohletz, K., 2014. Sequential fragmentation/transport theory, pyroclast size-density relationships, and the emplacement dynamics of pyroclastic density currents – A case study on the Mt. St. Helens (USA) 1980 eruption. *Journal of Volcanology and Geothermal Research*, 275: 1-13.
- Major, J.M., 1997. Depositional Processes in Large-Scale Debris-Flow Experiments. *Depositional Processes in Large-Scale Debris-Flow Experiments*.
- Major, J.M., Pierson, T.C., Hoblitt, R.P., Moreno, H., 2013. Pyroclastic density currents associated with the 2008-2009 eruption of Chaitén Volcano (Chile): Forest disturbances, deposits, and dynamics. *Andean Geology*, 40(2): 324-358.
- Miyabuchi, Y., 1999. Deposits associated with the 1990–1995 eruption of Unzen volcano, Japan. *Journal of Volcanology and Geothermal Research*, 89: 139-158.
- Mosbrucker, A.R., 2014, High-resolution digital elevation model of Mount St. Helens crater and upper North Fork Toutle River basin, Washington, based on an airborne lidar survey of September 2009: U.S. Geological Survey Data Series 904, <https://dx.doi.org/10.3133/ds904>.
- Neri, A., Esposti Ongaro, T., Menconi, G., De'Michieli Vitturi, M., Cavazzoni, C., Erbacci, G. and Baxter, P.J., 2007. 4D simulation of explosive eruption dynamics at Vesuvius. *Geophysical research letters*, 34(4).
- Nairn, I.A., Self, S., Cole, J.W., Leonard, G.S., Scutter, C., 2001. Distribution, stratigraphy, and history of proximal deposits from the c. AD 1305 Kaharoa eruptive episode at Tarawera Volcano, New Zealand. *New Zealand Journal of Geology and Geophysics*, 44(3): 467-484.
- NASA LP DAAC., 2001. ASTER Level 2 Surface Radiance Product (TIR). NASA LP DAAC. [http://doi.org/10.5067/ASTER/AST\\_09T.003](http://doi.org/10.5067/ASTER/AST_09T.003).

- Ogburn, S.E., 2012. FlowDat: Mass flow database v2.2. On Vhub at <https://vhub.org/groups/massflowdatabase>.
- Ogburn, S.E., Loughlin, S.C. and Calder, E.S., 2015. The association of lava dome growth with major explosive activity (VEI [greater-than or equal to] 4): DomeHaz, a global dataset. *Bulletin of Volcanology*, 77(5), p.1.
- Ovsyannikov, A., Manevich, A., 2010, Eruption Shiveluch in October 2010, *Bulletin of Kamchatka Regional Association (Educational-Scientific Center); Earth Sciences (in Russian)*, IV&S FEB RAS, Petropavlovsk-Kamchatsky, 2010, vol. 2, no. 16, ISSN 1816-5532.
- Pallister, J.S., Clynne, M.A., Wright, H.M., Van Eaton, A.R., Vallance, J.W., Sherrod, D.R., Kokelaar, B.P., In Prep. IAVCEI Field Trip Guide to Mount St. Helens - An overview of the eruptive history and petrology, tephra deposits, 1980 pyroclastic deposits and the crater.
- Pallister, J., Wessels, R., Griswold, J., Kartadinata, N., Gunawan, H., Budianto, A., Primulyana, S. 2017. Remote sensing of the Sinabung eruption: Use of Optical, IR and Satellite Radar Imagery to monitor activity, estimate effusion rates, forecast collapse events and map the distribution of pyroclastic deposits. *Journal of Volcanology and Geothermal Research* (in press).
- Pineau, F., Semet, M.P., Grassineau, N., Okrugin, V.M., Javoy, M., 1999. The genesis of the stable isotope (O, H) record in arc magmas: the Kamchatka's case. *Chemical Geology* 153 (1–4), 93–124.
- Ponomareva, V., Kyle, P., Pevzner, M., Sulerzhitsky, L., Hartman, M., 2007. Holocene Eruptive History of Shiveluch Volcano, Kamchatka Peninsula, Russia. *Volcanism and Subduction: The Kamchatka Region Geophysical Monograph Series* 172.
- Realmutto, V.J., 1990. Separating the effects of temperature and emissivity: emissivity spectrum normalization. *Proceedings of the 2nd TIMS Workshop*, 2, pp. 31–35.
- Ramsey, M.S., Dehn, J., 2004. Spaceborne observations of the 2000 Bezymianny, Kamchatka eruption: the integration of high-resolution ASTER data into near real-time monitoring using AVHRR. *Journal of Volcanology and Geothermal Research*, 135: 127-146.
- Ramsey, M.S., Wessels, R.L., Anderson, S.W., 2012. Surface textures and dynamics of the 2005 lava dome at Shiveluch volcano, Kamchatka. *GSA Bulletin*; May/June 2012; v. 124; no. 5/6; p. 678–689.
- Reath, K.A., 2017. Thermal infrared analysis of volcanic processes. (Unpublished Doctoral dissertation). University of Pittsburgh, Pittsburgh.
- Rodriguez-Elizarrards, S., Siebe, C., Komorowski, J.-C., Espindola, J.M., Saucedo, R., 1991. Field observations of pristine block- and ash-flow deposits emplaced April 16-17, 1991 at Volcan de Colima, Mexico. *Journal of Volcanology and Geothermal Research*, 48: 399-412.

- Rowley, P.D., Kuntz, M.A., MacLeod, 1981. Pyroclastic-flow deposits, in Lipman, P.W., Mullineaux, D.R., [Eds.]. The 1980 eruptions of Mount St. Helens, Washington. US Geological Survey Professional Paper 1250, pp. 489-512.
- Rowley, P.D., MacLeod, N.S., Kuntz, M.A., Kaplan, 1985. Proximal bedded deposits related to pyroclastic flows of 18 May, 1980, Mount St. Helens, Washington. Geological Society of America Bulletin, 86: 1373-1383.
- Saucedo, R., Macias, J.L., Sheridan, M.F., Bursik, M.I., Komorowski, J.-C., 2005. Modeling of pyroclastic flows of Colima Volcano, Mexico: implications for hazard assessment. Journal of Volcanology and Geothermal Research, 139:103-115
- Schilling SP (1998) LAHARZ: GIS programs for automated mapping of lahar-inundation zones. US Geol. Survey, Open-file Report 98-638
- Schneider, D.J., Vallance, J.W., Wessels, R.L., Logan, M., Ramsey, M.S., 2008. Use of thermal infrared imaging for monitoring renewed dome growth at Mount St. Helens, 2004, In: Sherrod, D.R., Scott, W.E. and Stauffer, P.H., (Eds.), A volcano rekindled: The renewed eruption of Mount St. Helens, 2004-2006. U.S. Geological Survey Professional Paper 1750, 347-360.
- Shevchenko, A.V., Dvigalo, V.N., Svirid, I.Y., 2015. Airborne photogrammetry and geomorphological analysis of the 2001–2012 exogenous dome growth at Molodoy Shiveluch Volcano, Kamchatka. Journal of Volcanology and Geothermal Research, 304: 94-107.
- Shevchenko, A.V., Svirid, I. Yu, 2014. Collapsing processes of the current lava dome at Molodoy Shiveluch Volcano. Proceedings of the XIII regional youth conference “The natural environment of Kamchatka”. Institute of Volcanology and Seismology FEB RAS, Petropavlovsk-Kamchatsky, pp. 129–142 (in Russian).
- Schwarzkopf, L.M., Schmincke, H.-U., Cronin, S.J., 2005. A conceptual model for block-and-ash flow basal avalanche transport and deposition, based on deposit architecture of 1998 and 1994 Merapi flows. Journal of Volcanology and Geothermal Research, 139: 117.
- Schwarzkopf, L.M., Schmincke, H.-U., Troll, V.R., 2001. Pseudotachylite on impact marks of block surfaces in block-and-ash flows at Merapi volcano, Central Java, Indonesia. International Journal of Earth Sciences, 90(4): 769-775.
- Solikhin, A., Pinel, V., Vandemeulebrouck, J., Thouret, J.-C., Hendrasto, M., 2015. Mapping the 2010 Merapi pyroclastic deposits using dual-polarization Synthetic Aperture Radar (SAR) data. Remote Sensing of Environment, 158: 180-192.
- Solomina, O., 2010. Unknown eruption of Shiveluch volcano (Kamchatka, Russia) around AD1756 is identified by dendrochronology. In: Tree-Ring Reconstructions in Natural Hazards Research. Series: Advances in Global Change Research (AGLO) Eds. M. Stoffel, M. Bollschweiler, D. R. Butler, B. H.Luckman. DOI 10.1007/978-90-481-8736-2. p.483-484. p. 443-452.

- Sparks, R.S.J., Barclay, J., Calder, E.S., Herd, R.A., Komorowski, J.-C., Lockett, R., Norton, G.E., Ritchie, L.J., Voight, B., Woods, A.W., 2002. Generation of a debris avalanche and violent pyroclastic density current on 26 December (Boxing Day) 1997 at Soufrière Hills Volcano, Montserrat. In: T. H. Druitt and R. Kokelaar (Eds.), *The Eruption of Soufrière Hills Volcano, Montserrat from 1995 to 1999*, Geological Society Memoirs, 21, 409–434.
- Surono, Jousset, P., Pallister, J., Boichu, M., Fabrizia Buongiorno, M., Budisantoso, A., Costa, F., Andreastuti, S., Prata, F., Schneider, D., Clarisse, L., Humaida, H., Sumarti, S., Bignami, C., Griswold, J., Carn, S., Oppenheimer, C., Lavigne, F., 2012. The 2010 explosive eruption of Java's Merapi volcano—A '100-year' event. *Journal of Volcanology and Geothermal Research*, 241-242: 121-135.
- Tadahide, U., Matsuwo, N., Sumita, M., Fujinawa, A., 1999. Generation of block and ash flows during the 1990–1995 eruption of Unzen Volcano, Japan. *Journal of Volcanology and Geothermal Research*, 89: 123-137.
- Thouret, J.-C., Gupta, A., Lube, G., Liew, S.C., Cronin, S.J., Surono, 2010. The 2006 pyroclastic deposits of Merapi Volcano, Java, Indonesia: High-spatial resolution IKONOS images and complementary ground based observations. *Remote Sensing of Environment*, 144(9): 1949-1967.
- Thouret, J.-C., Kassouk, Z., Gupta, A., Liew, S.C., Solikhin, A., 2015. Tracing the evolution of 2010 Merapi volcanic deposits (Indonesia) based on object-oriented classification and analysis of multi-temporal, very high resolution images. *Remote Sensing of Environment*, 170: 350-371.
- Tolstykh, M.L., Naumov, V.B., Babanskii, A.D., Khubunaya, S.A., Kononkova, N.N., 2000. Chemical composition, trace elements, and volatile components of melt inclusions in minerals from andesites of the Shiveluch volcano, Kamchatka. *Geochemistry International* 38, 123–132.
- Torres, R.C., Self, S., Martinez, M.M.L., 1996. Secondary pyroclastic flows from the June 15, 1991, ignimbrite of Mount Pinatubo. In Newhall, C.G., and Punongbayan (eds.) *Fire and Mud: Eruption and Lahars of Mount Pinatubo, Philippines*. Quezon City, Philippines, Philippine Institute of Volcanology and Seismology, pp. 665-678.
- Urai, M., Fukui, K., Yamaguchi, Y., Pieri, D.C., 1999. Volcano observation potential and global volcano monitoring plan with ASTER. *Volcano Society of Japan*, 11(16): 131-141.
- Vaughan, R.G., Hook, S.J., Ramsey, M.S., Realmuto, V.J., Schneider, D.J., 2005. Monitoring eruptive activity at Mount St. Helens with TIR image data. *Geophysical Research Letters*, 32: doi:10.1029/2005GL024112.
- Vallance J. W., Bull K. F., Coombs M. L., Power J. A., Coombs M. L., Freymueller J. T., 2010. Pyroclastic flows, lahars, and mixed avalanches generated during the 2006 eruption of Augustine Volcano, The 2006 eruption of Augustine Volcano, Alaska. *US Geological Survey, Professional Papers*, 2010, vol. 1769 (pg. 219-268)

- VONA/KVERT Weekly Release. KVERT, Institute of Volcanology and Seismology FEB RAS.  
URL: <http://www.kscnet.ru/ivs/kvert/van/index.php?type=3>.
- Wadge, G., Voight, B., Sparks, R.S.J., Cole, P.D., Loughlin, S.C., Robertson, R.E.A., 2014. An overview of the eruption of Soufrière Hills Volcano, Montserrat from 2000 to 2010. In Wadge, G., Robertson, R. E. A. & Voight, B. (eds) 2014. *The Eruption of Soufriere Hills Volcano, Montserrat from 2000 to 2010*. Geological Society, London, *Memoirs*, 39, 1–39. <http://dx.doi.org/10.1144/M39.1>
- Widiwijayanti, C., Voight, B., Hidayat, D., Schilling, S.P., 2009. Objective rapid delineation of areas at risk from block-and-ash pyroclastic flows and surges. *Bulletin of Volcanology*, 71:687-703
- Wilson, L., Head, J.W., 1981. Morphology and Rheology of pyroclastic flows and their deposits, and guidelines for future observations, in Lipman, P.W., Mullineaux, D.R., [Eds.]. *The 1980 eruptions of Mount St. Helens, Washington*. U.S. Geological Survey Professional Paper 1250, pp. 489-512.
- Wright, H., Pallister, J., McCausland, W., Griswold, J., Andreastuti, S., Budianto, A., Primulyana, S., Gunawan, H., VDAP team, and CVGHM team, 2017. Construction of probabilistic event trees for eruption forecasting at Sinabung volcano, Indonesia 2013-14, *Journal of Volcanology and Geothermal Research* (in review).
- Yulianto, F., Suwarsono, Sofan, P., 2016. The Utilization of Remotely Sensed Data to Analyze the Estimated Volume of Pyroclastic Deposits and Morphological Changes Caused by the 2010–2015 Eruption of Sinabung Volcano, North Sumatra, Indonesia. *Pure Applied Geophysics*, 173:2711-2725.
- Zharinov, N.A., Demyanchuk, Y.V., 2008. The growth of an extrusive dome on Shiveluch Volcano, Kamchatka in 1980–2007: Geodetic observations and video surveys. *Journal of Volcanology and Seismology*, 2(4): 217-227.
- Zharinov, N.A., Demyanchuk, Y.V., 2013. Large Explosive Eruptions of Shiveluch Volcano, Kamchatka Resulting in Partial Destruction of the Extrusive Dome (February 28, 2005 and October 27, 2010).